博士論文

Ultrasound waveform tomography with the ring transducer for the breast imaging
（乳房イメージングのためのリングトランスデューサーによる超音波波形トモグラフィー）

林　宏翔

DOCTORAL THESIS

Ultrasound waveform tomography with the ring transducer for the breast imaging

Author: Hongxiang Lin

Fluids Engineering Laboratory
Department of Mechanical Engineering
THE UNIVERSITY OF TOKYO

Supervisor: Shu Takagi, Professor

June 1, 2017

Contents

Chapter 1

Introduction

1.1 Overview of breast cancer

Cancer is a collection of diseases that are caused by the uncontrollable division and spread of abnormal cells in the body. In all types of cancers, breast cancer becomes a great risk that endangers female's lives. Referred to the database in National Cancer Center Japan, breast ranks the first of the incident rate of the female's organs that suffers from cancer (**NCC_incident_ranking**). In Unit States, breast cancer takes the second place of age-adjust cancer death rate since 1990 (**AmericanCancerSociety2017**). Typically, forty-year-old postmenopausal women with high breast tissue density and high levels of endogenous hormones are vulnerable to develop breast cancer in general. Additionally, the modern lifestyle significantly increases the possibility of breast cancer risk factors. A report statistically points out that women who have experience on postmenopausal hormone use, obesity caused by the junk food and lack of physical exercise, unhealthy diet, drinking, smoking, and oral contraceptive use may take a higher risk of breast cancer than those having no experience, although there is no direct evidence on the relation of the unhealthy lifestyle and breast cancer.

Historically, the ancients originated "cancer" from the illustration of the limbs of a crab and believed that crab or crawfish has the therapeutic utility for cancer, which was an embryonic form of the conservative treatment. In the period of Alexandria, Leonides developed a test of operating the surgery for breast cancer (**DeMouLin1989**). And in the twenty-first century, breast cancer surgery, such as breast-conserving surgery or mastectomy, is now a regular way for treatment. Breast cancer with early stage is possible to conduct breast-conserving surgery to remove the tumors plus the surrounding tissue. Otherwise, there is no choice but to do the mastectomy or even radiation, chemo, and hormone therapy for the advanced case where invasive cancers occur. Anyway, the patients who receive the surgery will eventually suffer from the severe pain. Instead of the conventional surgery, a next generation medical solution using the high intensity focused ultrasound (HIFU) for soft-tissue tumors aims at developing a new noninvasive[1] treatment radiated from the outer human body (**Huber2001**).

For the sake of alleviating the painful burden during cancer treatment, tumor cells at the early stage are able to be removed with a small cut. Pathologically, breast cancer ranking from Stage 0 to Stage IV are mainly determined by the size of tumors. Stages I, and II, which is known as the early stage, namely, classify by means of the tumor size of less than 20 mm and 50 mm, respectively. Moreover, some noninvasive breast cancer occurring in the fibroglandular parenchymal tissue are called Stage 0 or furthermore Stage tissue (Tis). It is also known as ductal carcinoma in situ (DCIS) recognized at the fibrous connective tissue like ducts or lobular carcinoma in situ (LCIS) at the glandular tissue like lobules. And the statistic data from National Cancer Center Hospital indicates the survival rate in Stages Tis, I, and II of breast cancer is 94.72%, 89.10%, and 78.60%, respectively citenational...!!!!!!!! . With the development of Japan's health care policies for the year 2035, the noninvasive diagnostic system for the early stage breast cancer will become one of the potential addressed issues on the consideration of efficiency as well as precision of diagnosis, treatment, and nursing (**mhlw_health_care_2035**).

1.2 Breast imaging modalities

The transition from "cure" to "care" in the global revolution of the future health care motivates us to reconsider assessing whether the classical breast imaging modalities meet the needs of public health care promotion. Medical images obtained from the breast cancer scanning systems, such as mammography, magnetic resonance imaging (MRI), and sonography, are able to provide the prescribed resolution and contrast for the soft tissue. Using the medical images enables doctors to have a objective standard for judging the stage of the breast cancer and target the location of tumors prior to surgery. Only clinical breast examination can provide the service of the breast cancer scanning and doing examination usually requires the patient's self-awareness. Fortunately in most cases, breast cancer symptoms allow women to aware

---

[1] "Noninvasive" here indicates that the ablation targets at the tumors and causes little destruction on the normal tissues.

abnormalties happening in her bodies. However, the future health care requires earlier clinical diagnosis when the tumors are still as small as approximate 1-2 millimeter. Besides, in order to make the breast cancer screening as a program of the regular physical examination accepted annually, the ideal scanning system at least possesses the following criterion: non-destruction and irradiation, low expanse, short scanning time, and reliable examination result. At the same time a small-scale scanning systems may help save the room and extend the application in other scenarios, such as the examination in ambulance or spaceship.

1.2.1 Mammography

1.2.2 Magnetic resonance imaging

1.2.3 Sonography

1.2.4 Photoacoustic tomography

1.3 Ultrasound waveform tomography

The restricted concept of ultrasound waveform tomography is mathematically an inverse problem of the wave propagation equation which reconstructs the anatomic medical image of breast indicating the category and structure for each kind of tissue inside, given the received ultrasound signals only measured at the transducer. But in this study, it is regarded as developing the complete breast imaging system including the ultrasound scanning device, the waveform simulation for the ultrasound propagating in the breast tissue, and the clinical application more than the mathematical consideration of image reconstruction. In other works, the complete breast imaging system is also named ultrasound computed tomography (USCT).

Ultrasound Computed Tomography (USCT) is a novel modality of medical imaging technology for breast cancer detection. The scanning system of USCT is conducted on a two-dimensional ring-array transducer; see Figure 1.1. By vertically moving the transducer, it is able to scan the breast slice by slice and acquire the three-dimensional ultrasound measurements. The measurements record the acoustic properties, i.e. transmission, reflection, refraction, diffraction, etc, inside the transducer in all directions. USCT allows us to detect the 2-mm scale tumor from the reconstructed image. Nowadays, USCT has a wide prospect for the future research and application of health care because of its absence of the radiation dose compared with X-ray CT and mammography, costing extremely lower expenses with an equal-level reconstructed image of MRI, and acting as a nondestructive imaging test compared with PET/SPECT.

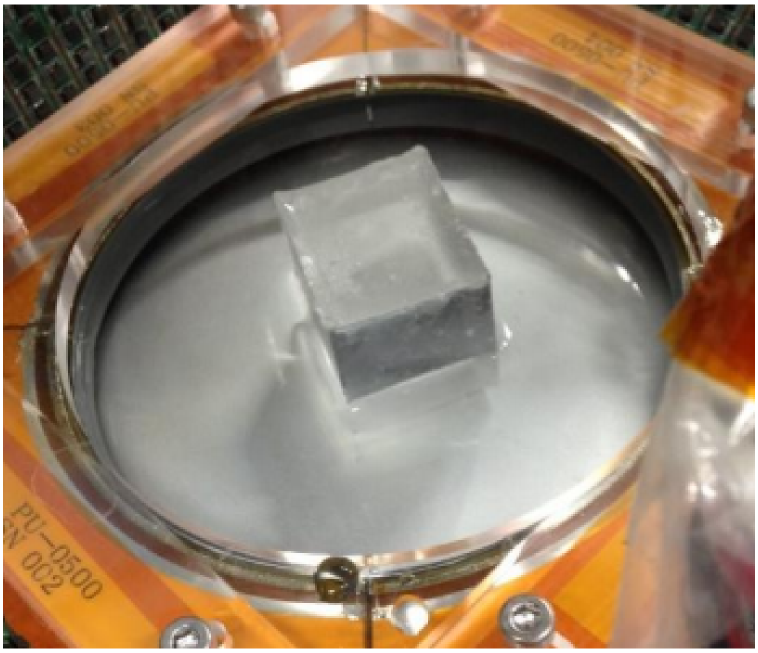

FIGURE 1.1: Ring-array Transducers (**Nakamura2014**)

Previously, USCT was difficult to advance the progress of physical applications because of its dramatic computation cost and its low resolution. However, a novel USCT device studied in our lab, based on ring-array transducers and Verasonics for data acquisition, sheds new light on the early detection of the small-scaled tumor by a high-resolution breast image; see Figure 1.1. With it, USCT reconstructs sound speed and attenuation images in the domain of ring-array transducers instead of acoustical impedance image from the popular echo imaging in the domain of linear-array transducers, as we utilize the full waveform model well discussed before from other research fields (seismic imaging, inverse scattering, etc.). And compared with the limit modes of the linear-array transducers, like the transmission or reflection mode, the ring-array ones are designed to study the full waveform mode, which is a more accurate model than others, with arbitrary emitted and received directions, resulting in an acceptable resolution of image. Additionally, some recent works accelerates USCT algorithms by applying GPU (Graphic Processing Unit) computing, expected to save the computing time for one USCT job; see [Roy2010].

We present a classical literature review of models and algorithms related to USCT below. Previously, with the limitation of computing performance, the full waveform USCT was approximated by: diffraction tomography with Born or Rytov approximation [Devaney1982, 1986], the Eikonal Equation with straight-line approximation [Greenleaf1983], seismic methods in the Fourier domain [Brukhout et al.1982], initial value inverse scattering transformed from boundary value one [Natterer, Wubbeling1995], etc; Afterwards, as the development of the high performance hardware, the researchers began to return to original full waveform model, such as the ultrasound tomography by exploiting seismic wave propagation [Natterer2008b], inverse acoustic mammography in the time domain [Natterer 2008a], reflection mode of inverse acoustic scattering by CARI and analytical continuation [Natter 2011a, 2011b]. In terms of the classical USCT algorithms, we refer to a propagation-backpropagation method in 2D and 3D, see [Natterer and Wubbeling1995] and [Natterer1997] which is well-known as Landweber-Kaczmarz's method [Kaltenbacher, Neubauer, Scherzer2008], contrast source inversion and its extensions, see [van den Berg and Kleinman1997], [van den Berg, van Broekhoven and Abubakar1999], [Abubakar et al.2008] and the recent work [van Dongen et al.2013], the 3D inverse medium scattering solver [Hohage2001], marching schemes for USCT [Natterer and Wubbeling2005], etc.

The recent USCT prototype "SoftVue", built by Delphinus Medical Technologies, is of ability to simultaneously reconstruct the parametric cross-sectional images, such as the distribution of speed of sound, attenuation, and acoustical impedance (or the echo image); found in the homepage of Delphinus Medical Technologies. The related searches they published hold on the following topics: practical computation of experimental data, the comparison between the numerical full waveform algorithm, and the previous ray-tracing methods, and its GPU implementation; see [Duric et al. 2013, 2014], [Roy, et al. 2013], [Sak, et al. 2014], [Sandhu, et al. 2014], etc. However, different with their research direction, the work focuses on the fast and robust improvement for the current algorithms suitable to GPU computing and our own USCT device. Our team get started with the robustness consideration on the bent-tracing reconstruction of USCT [Qu2015].

1.4 Introduction to inverse problems theory

1.5 Outline of the dissertation

Chapter 2

Forward problem of wave propagation

The forward problem of wave propagation is developed to numerically computing the ultrasound wavefield in the imaging domain as well as on the ring transducer, given the acoustic coefficients and the source term. In this study, speed of sound and attenuation in a viscous fluid are considered in terms of the acoustic property, leading to the derivation of the attenuated wave equation. The forward problem is regarded as a computer simulator performing the wave phenomena that occur in the ring transducer, i.e. transmission, reflection, refraction, diffraction, and scattering. More significantly, ultrasound waveform inversion allows us to reconstruction the acoustic coefficients by means of iteratively computing the solver of the forward problem. It requires the numerical solver possessing an efficient way to better match the key features, says amplitude and phase, of the measured data on the ring transducer. In this chapter, the numerical solvers built in the frequency domain intends to generate the simulated data at principal frequencies if the relatively narrow bandwidth of the measured data is acquired from the pulse excitation. One anticipates that the frequency-domain solver with the use of the partial frequency components of the measured data enables us to reconstruct the breast image, provided a sufficient accuracy.

The study of the forward problem of wave propagation is organized as follows: In Section 2.1, the attenuated wave equation is derived with the knowledge of the fluid mechanics. The forward problem is developed and discussed in Section 2.2 by extending the attenuated wave equation into the frequency-domain formula – Helmholtz equation and its integral equation – the Lippmann-Schwinger equation. Section 2.3 introduces two numerical solvers built with ulitizing the Cartesian and trigonometric bases. The complexity and computational burden for the two solvers are discussed. In

Section 2.3, the verification study of accuracy is conducted on the numerical solvers when the configuration is similar to that in the real experiments. Finally, the discussion and conclusion are included in Section 2.5.

2.1 Derivation of the attenuated wave equation

In this section, the derivation of the attenuated wave equation is reviewed by a way of starting with the view of viscous fluid mechanics. First the spatial coordinate of the variables, vector-valued functions, and tensors are set in the N-dimensional Cartesian system, especially with $N = 1, 2, 3$ for the nature of physics. Particularly, the spatial coordinate with a capital letter denotes the position of the particle with the reference time while that with a small letter denotes ordinary position in a space. In the following, the Euler's equation of motion is introduced by means of expressing the velocity as the function of the reference time in the Lagrangian description. In this case, the laws of conservation is constructed through tracking the motion at an fixed individual particle. The particle is deformed from the initial position $\mathbf{X}$ to the point $\mathbf{x}(\mathbf{X}, t)$ at the present time t. Additionally, the constitutive relation between stress and strain is considered in the fluid. The Eulerian description is used to observe the motion of the particle at a fixed spatial position $\mathbf{x}$ for period of time.

The propagation of the acoustic wave arising from the small oscillatory of the fluid particle results in the attenuated wave equation, performing the behaviors of vibration (compression/rarefaction) as well as dissipation. A general fluid motion is addressed by the governing law of the momentum diffusion. Then the motion is restricted to the acoustic wave with the situation of the adiabatic compression. Several assumptions and approximations are considered as prerequisites in the place prior to the specific theories being presented.

2.1.1 The Euler's equation of motion

Consider that with the Lagrangian description, the displacement $\mathbf{u}(\mathbf{X}, t)$, the velocity $\mathbf{v}(\mathbf{X}, t)$, and the density field $\rho(\mathbf{X}, t)$ are defined on the infinitesimal volume V of the fluid particle which satisfies

$$\mathbf{u}(\mathbf{X}, t) = \mathbf{x}(\mathbf{X}, t) - X, \qquad \mathbf{v}(\mathbf{X}, t) = \frac{\mathrm{D}\mathbf{u}}{\mathrm{D}t}(\mathbf{X}, t). \tag{2.1.1}$$

The derivative in the Lagrangian description or the material derivative $\mathrm{D}/\mathrm{D}t$ is given as

$$\frac{\mathrm{D}}{\mathrm{D}t} = \frac{\partial}{\partial t} + \mathbf{v}\cdot\nabla_{\mathbf{X}}, \tag{2.1.2}$$

where the dot $\cdot$ denotes the inner product and ∇ the gradient with respect to $\mathbf{X}$. Then the Reynolds' transport theorem follows with the definition of the material derivative for an arbitrary differentiable function $A(\mathbf{X}, t)$:

$$\frac{\mathrm{D}}{\mathrm{D}t}\int_V A(\mathbf{X}, t)\mathrm{d}V = \int_V \left[\frac{\mathrm{D}A}{\mathrm{D}t} + A\nabla_{\mathbf{X}}\cdot\mathbf{v}\right]\mathrm{d}V. \tag{2.1.3}$$

We introduce the equation of continuity and motion for a fluid particle in the Lagrangian description. Applying the conservation of mass, Eq. (2.1.3), and selecting $A = \rho$ yields the continuity equation in the Lagrangian description:

$$\frac{\mathrm{D}}{\mathrm{D}t}\int_V \rho\mathrm{d}V = \int_V \frac{\mathrm{D}\rho}{\mathrm{D}t} + \rho\nabla_{\mathbf{X}}\cdot\mathbf{v} = 0, \tag{2.1.4}$$

Applying the conservation of momentum, Eq. (2.1.3), and $A = \rho\mathbf{v}$ the force acting on the volume is given by

$$\frac{\mathrm{D}}{\mathrm{D}t}\int_V \rho\mathbf{v}\mathrm{d}V = \int_V \left[\frac{\mathrm{D}(\rho\mathbf{v})}{\mathrm{D}t} + \rho\mathbf{v}\nabla_{\mathbf{X}}\cdot\mathbf{v}\right]\mathrm{d}V = \int_V \mathbf{f}\mathrm{d}V + \int_S \mathcal{T}\cdot\mathbf{n}_S\mathrm{d}S, \tag{2.1.5}$$

where $\mathbf{f}(\mathbf{X}, t)$ denotes the body force on V, the stress tensor $\mathcal{T}(\mathbf{X}, t)$ represents the surface force acting on the surface S of V, and the vector $\mathbf{n}_S$ is defined as the outer normal vector on S. Combining Eqs. (2.1.1, 2.1.4, 2.1.5) and applying the Gauss' divergence theorem yield the Euler's equation of motion

$$\rho\frac{\mathrm{D}\mathbf{v}}{\mathrm{D}t} = \nabla_{\mathbf{X}}\cdot\mathcal{T} + \mathbf{f}. \tag{2.1.6}$$

2.1.2 Constitutive relation in a viscous fluid

Naturally, particles in compressible viscous fluid are allowed to measure the stress force from the extent of distortion which is called strain rate. Commonly, we start with the differential of the velocity $\mathbf{v}(\mathbf{x}, t)$ in the Eulerian description given as the spatial distorted rate, i.e.

$$\mathrm{d}v_j = \frac{\partial v_j}{\partial x_k}\mathrm{d}x_k. \tag{2.1.7}$$

In this subsection, we claim that all indices, such as j, k etc., in this subsection satisfy Einstein summation. To further see the motion modes of the fluid particle, Eq. (2.1.7) can be decomposed into

$$\mathrm{d}v_j = \frac{1}{2}\left(\frac{\partial v_j}{\partial x_k} + \frac{\partial v_k}{\partial x_j}\right)\mathrm{d}x_k + \frac{1}{2}(\nabla_{\mathbf{x}} \times \mathbf{v} \times \mathbf{dx})_j, \tag{2.1.8}$$

where the rotation motion is obtained from the term $\left(\frac{\partial v_j}{\partial x_k} - \frac{\partial v_k}{\partial x_j}\right)\mathrm{d}x_k = (\nabla_{\mathbf{x}} \times \mathbf{v} \times \mathbf{dx})_j$ where $\times$ denotes the cross product with the property:

$$(\mathbf{a} \times \mathbf{b})_j = \varepsilon_{jkl} a_k b_l.$$

Since $\nabla \times \mathbf{u} \times \mathbf{dx} \cdot \mathbf{dx} = 0$, the rotation has no effect on the extention of the particle at the direction of dx. Thus, the strain rate e_{jk} is attributed to the remaining term of Eq. (2.1.8):

$$e_{jk} = \frac{1}{2}\left(\frac{\partial v_j}{\partial x_k} + \frac{\partial v_k}{\partial x_j}\right). \tag{2.1.9}$$

In this study, the constitutive relation of stress and strain is required to characterize the viscous effect of the medium. The fluid particle is said to be linear isotropic if stress is represented as a linear combination of the strain rate. In specific, it can be referred to **ben2012seismic**; **kundu20125th** that the constitutive relation is given by the Navier-Poisson law (or the linear isotropic relation) as follows:

$$\mathcal{T}_{jk} = -\mu\delta_{jk} + \left(\eta_{\text{bulk}} - \frac{2}{3}\eta_{\text{shear}}\right)\delta_{jk}e_{ll} + 2\eta_{\text{shear}}e_{jk}, \tag{2.1.10}$$

where the coefficient $\mu(\mathbf{x}, t)$, $\eta_{\text{bulk}}(\mathbf{x})$, and $\eta_{\text{shear}}(\mathbf{x})$ denotes the magnitude of the normal stress, the bulk viscosity and the shear viscosity.

Note that μ is identical with the hydrostatic pressure satisfying the fact that it is proportional to the displacement gradient for a given mass of the particle. In specific, there is an assumption that the compression in the fluid is adiabatic when the entropy S is kept as a constant. Following the state equation $\mu = \mu(\rho, S)$ and the continuity equation (2.1.4), the hydrostatic pressure satisfies the relation

$$\frac{\mathrm{D}\mu}{\mathrm{D}t} = \left(\frac{\partial \mu}{\partial \rho}\right)_S \frac{\mathrm{D}\rho}{\mathrm{D}t} = -\kappa_S \nabla \cdot \mathbf{v}, \tag{2.1.11}$$

where the adiabatic bulk modulus κ_S is defined as a measure of resistance to compressibility of a fluid which has the expression

$$\kappa_S = \rho \frac{\partial \mu}{\partial \rho}. \tag{2.1.12}$$

The bulk viscosity is also called as the second viscosity (**LANDAU1987**). It describes the energy loss produced by the hydrodynamic compression and rarefaction. The shear viscosity is related to the resistance of the shear stress in the fluid.

2.1.3 Acoustic wave

Next, in terms of the consideration of the attenuated wave equation for acoustic wave, the additional approximations are required to simplify the aforementioned equations. One adds the several assumptions for the acoustic wave propagation in the viscous fluid as follows:

1. With the low-velocity approximation, the particle is oscillated around the same position for any time. In this situation, there is no difference between the Eulerian and Lagrangian descriptions and the derivatives have the relation
$$\frac{\mathrm{D}}{\mathrm{D}t} = \frac{\partial}{\partial t}, \quad \nabla = \nabla_{\mathrm{x}} = \nabla_{\mathbf{X}}; \tag{2.1.13}$$
2. Sound wave propagating in the linear isotropic viscous fluid satisfies the constitutive equation (2.1.10);
3. The density ρ is independent of the time and space;
4. There is no shear stress acting on the particle, i.e. $\eta_{\text{shear}} = 0$.
5. The displacement and velocity of particle are assumed to be irrotational and the body force is conservative such that

$$\mathbf{v} = \nabla P, \qquad \frac{\partial \mathbf{f}}{\partial t} = -\rho \nabla Q. \tag{2.1.14}$$

With the point 1, Eq. (2.1.11) again yields the relation of μ and $\mathbf{v}$

$$\frac{\partial \mu}{\partial t} + \kappa_S \nabla \cdot \mathbf{v} = 0. \tag{2.1.15}$$

Combining Eq. (2.1.9) and the points 1,2, and 4, the momentum equation (2.1.6) reduces to

$$\rho\frac{\partial \mathbf{v}}{\partial t} = -\nabla\mu + \nabla\left(\eta_{\text{bulk}}\nabla\cdot\mathbf{v}\right) + \mathbf{f}. \tag{2.1.16}$$

Incorporated with Eq. (2.1.15) and the point 5, we have

$$\begin{aligned}\rho\frac{\partial}{\partial t}\nabla P &= \nabla\left(\kappa_S\nabla\cdot\mathbf{v}\right) + \nabla\left(\eta_{\text{bulk}}\nabla\cdot\frac{\partial \mathbf{v}}{\partial t}\right) + \frac{\partial \mathbf{f}}{\partial t}\\ &= \nabla\left(\kappa_S\nabla\cdot\nabla P\right) + \nabla\left(\eta_{\text{bulk}}\nabla\cdot\frac{\partial}{\partial t}\nabla P\right) - \rho\nabla Q.\end{aligned} \tag{2.1.17}$$

Thus, with the use of the point 3, Eq. (2.1.16) finally yields the attenuated wave equation

$$-\frac{\partial^2 P(\mathbf{x},t)}{\partial t^2} + c^2(\mathbf{x})\nabla^2 P(\mathbf{x},t) + \frac{\eta_{\text{bulk}}(\mathbf{x})}{\rho}\nabla^2\frac{\partial P(\mathbf{x},t)}{\partial t} = Q(\mathbf{x},t). \tag{2.1.18}$$

Here, $c(\mathbf{x})$ denotes speed of sound with the definition

$$c = \sqrt{\frac{\kappa_S}{\rho}}.$$

There is a remark that the wave equation (2.1.18) free of attenuation can be also derived from the fluid mechanics theory in inviscid flow; see **kundu20125th**; **ben2012seismic**; **colton2013inverse** and the references therein. In that case, for the consideration of the physical meaning, it has the same equation as Eq.(2.1.18) and in this situation P represents acoustic pressure.

2.2 Helmholtz equation and the integral form

2.2.1 Helmholtz equation

Similar to the seismic application in **fokkema2013seismic**, the study of the wave equation (2.1.18) is conducted in the temporal frequency domain. The Fourier transform denoted by $\wedge$ for the displacement potential $P(\mathbf{x},t)$ is defined as

$$p(\mathbf{x},\omega) := \widehat{P(\mathbf{x},t)} = \int_{-\infty}^{+\infty} P(\mathbf{x},t)e^{i\omega t}\mathrm{d}t, \tag{2.2.1}$$

so is the volume force potential $Q(\mathbf{x},t)$. Here ω denotes the angular frequency. The capital-letter symbol denotes the Fourier-transformed function of the small-letter one. Substituting Eq. (2.2.1) into Eq. (2.1.18) yields the

Helmholtz equations in the region of heterogeneity immersed in the homogeneous medium with the speed of sound of c_0

$$\nabla^2 p(\mathbf{x},\omega) + K^2(\mathbf{x},\omega)p(\mathbf{x},\omega) = q_0(\mathbf{x},\omega), \tag{2.2.2}$$

in which the complex-valued (attenuated) wavenumber is denoted by $K(\mathbf{x},\omega)$ satisfying

$$K^2(\mathbf{x},\omega) = \frac{\omega^2}{c^2(\mathbf{x}) + i\omega\eta_{\text{bulk}}(\mathbf{x})/\rho}, \tag{2.2.3}$$

where the source term located in the reference homogeneous medium is given by $q_0(\mathbf{x},\omega) = q(\mathbf{x},\omega)/c_0^2$ in which q is transformed from Q via the Fourier transform.

To study the mathematical properties of the Helmholtz equation, the scattering theory is introduced to explain the scattered wavefield induced by the excitation from the scatterers or the so-called contrast source, by means of the linearization in the homogeneous medium. The scatterers are produced by the acoustic deviation between the homogeneous and heterogeneous medium with the use of the identical incident wavefield. In specific, the total wavefield propagating in the heterogeneous medium is composed by the incident wavefield denoted by $p^{\text{inc}}(\mathbf{x},\omega)$ in the homogeneous medium and the scattered wavefield $p^{\text{sct}}(\mathbf{x},\omega)$, i.e.

$$p = p^{\text{inc}} + p^{\text{sct}} \tag{2.2.4}$$

The incident wavefield satisfies the Helmholtz equation (2.2.2) with speed of sound being the constant c_0

$$\nabla^2 p^{\text{inc}}(\mathbf{x},\omega) + \frac{\omega^2}{c_0^2} p^{\text{inc}}(\mathbf{x},\omega) = q_0(\mathbf{x},\omega), \tag{2.2.5}$$

or

$$\nabla^2 p^{\text{inc}}(\mathbf{x},\omega) + K_0^2(\omega)p^{\text{inc}}(\mathbf{x},\omega) = q_0(\mathbf{x},\omega), \tag{2.2.6}$$

where $K_0(\omega) = \omega/c_0$ denotes the wavenumber in the homoegeneous medium. The choose of the point source term $q_0(\mathbf{x},\omega) = -\delta(\mathbf{x}-\mathbf{s})$ formulates the Green's function $G(\mathbf{x},\mathbf{s},\omega)$ of Eq. (2.2.5):

$$\nabla^2 G(\mathbf{x},\mathbf{s},\omega) + K_0^2(\omega)G(\mathbf{x},\mathbf{s},\omega) = -\delta(\mathbf{x}-\mathbf{s}). \tag{2.2.7}$$

To uniquely determine the solution of Eq. (2.2.7), the Sommerfeld radiation condition

$$\lim_{|\mathbf{x}|\to\infty} |\mathbf{x}|^{\frac{n-1}{2}} \left(\frac{\partial G(\mathbf{x},\mathbf{s},\omega)}{\partial \nu_{\mathbf{x}}} - iK_0(\omega)G(\mathbf{x},\mathbf{s},\omega) \right) = 0 \tag{2.2.8}$$

where $\nu_{\mathbf{x}}$ is the unit normal vector of $\mathbf{x}$, stipulates completion with an out-going spherically symmetric solution. This is called the free-space Green's function, which typically can be written in the dimensions $n = 1, 2, 3$:

$$G_{1D}(\mathbf{x},\mathbf{s},\omega) = \frac{i}{2K_0(\omega)} e^{iK_0(\omega)|\mathbf{x}-\mathbf{s}|}, \tag{2.2.9}$$

$$G_{2D}(\mathbf{x},\mathbf{s},\omega) = \frac{i}{4} H_0^{(1)}(K_0(\omega)|\mathbf{x}-\mathbf{s}|), \tag{2.2.10}$$

$$G_{3D}(\mathbf{x},\mathbf{s},\omega) = \frac{1}{4\pi|\mathbf{x}-\mathbf{s}|} e^{iK_0(\omega)|\mathbf{x}-\mathbf{s}|}. \tag{2.2.11}$$

Indeed, the term "out-going" is associated with the time-domain expression (2.2.1). Combining the phase factor $e^{iK_0(\omega)|\mathbf{x}-\mathbf{s}|}$ identically in Eqs. (2.2.9-2.2.11) with that of $e^{-i\omega t}$ in the integrand of Eq. (2.2.1) yields the out-going wave with the phase factor $e^{i(K_0(\omega)|\mathbf{x}-\mathbf{s}|-\omega t)}$ when the time t and distance $|\mathbf{x}|$ increases.

Particular solutions

Consider the particular solution of Eq. (2.2.6). The "out-going" of the wavefield is assumed as above. With the vanishing of the source term, i.e. $q_0 = 0$, the plain wave propagating in the direction of the unit vector $\mathbf{r}$ is given by

$$p^{\text{inc, plain}}(\mathbf{x};\omega,\mathbf{r}) = e^{iK_0(\omega)\mathbf{r}\cdot\mathbf{x}}. \tag{2.2.12}$$

On the other hand, the spherical wave is a wave which is emanated from a point source and propagates along omni-directions. Note that in this situation, the expressions of the sperical wave are identical to those of the Green's functions, i.e. Eqs. (2.2.9-2.2.11), with choosing $q_0(\mathbf{x},\omega) = -\delta(\mathbf{x}-\mathbf{s})$ where the point source is located at s.

Now consider the solution of the Helmholtz equation for the homogeneous medium in a finite domain. The use of the Green's representation theorem provides an integral expression in an open bounded domain Σ. Supposing that the domain Σ and the source term $q_0(\mathbf{x},\omega)$ have sufficient regularity, we have the Green's representation theorem for Eq. (2.2.6), referred to theorem 2.1 in **colton2013inverse**:

$$p^{\text{inc}}(\mathbf{x},\omega) = \int_{\partial\Sigma} \left\{ \frac{\partial p^{\text{inc}}(\mathbf{y},\omega)}{\partial \nu_{\mathbf{y}}} G(\mathbf{x},\mathbf{y},\omega) - \frac{\partial G(\mathbf{x},\mathbf{y},\omega)}{\partial \nu_{\mathbf{y}}} p^{\text{inc}}(\mathbf{y},\omega) \right\} \mathrm{d}\sigma(\mathbf{y}) - \int_{\Sigma} G(\mathbf{x},\mathbf{y},\omega) q_0(\mathbf{y},\omega) \mathrm{d}\mathbf{y}, \tag{2.2.13}$$

where $\mathbf{x} \in \Sigma$, $\partial\Sigma$ denotes the boundary of Σ, and $\nu_{\mathbf{y}}$ denotes the unit normal vector starting on $\mathbf{y} \in \partial\Sigma$ directed into the exterior of Σ.

Attenuation coefficient

According to the derivation of the attenuated wave equation (2.1.18), the bulk viscosity principally determines the attenuation effect and is included in the imaginary part of the complex-valued wavenumber K of Eq. (2.2.3). With keeping the branch point of the square root of K^2 which makes the imaginary part of K positive, one can explicitly write the expression of K:

$$K := \Re K + i\Im K = \frac{\omega}{(c^4 + \omega^2\eta^2/\rho^2)^{1/4}} e^{\frac{i}{2}\arctan\left(\frac{\omega\eta}{\rho c^2}\right)}. \tag{2.2.14}$$

Then similar to Eq. (2.2.12) for the plain wave in the homogeneous medium, one can have the ansatz[1] for the expression of the plain wave with the complex-valued wavenumber K in the direction of the unit vector $\mathbf{r}$:

$$P^{plain}(\mathbf{x},t) = e^{i(K\mathbf{x}\cdot\mathbf{r} - \omega t)}. \tag{2.2.15}$$

The intensity I is defined as $I = |P^{plain}|^2$. Attenuation can be measured by the intensity decay in a wavelength λ. Since the ratio of the intensity decay can be calculated from

$$\frac{I(\mathbf{x},t)}{I(\mathbf{x}+\lambda\mathbf{r},t)} = e^{2K_{\text{imag}}\lambda} \simeq e^{4\pi\Im K/\Re K} = e^{\frac{4\pi\omega\eta}{\rho c^2}},$$

---

[1] An ansatz is an assumed form for a mathematical establishment that is not based on any underlying physics theory or principle.–Wolfram MathWorld

with the assumption that $|\Re K| \gg |\Im K|$, the attenuation coefficient $\alpha(\mathbf{x})$ can be written as

$$\begin{aligned}\alpha(\mathbf{x})\ [\mathrm{dB}/(\mathrm{cm}\cdot\mathrm{MHz})] &= \frac{10\log(I(\mathbf{x},t)/I(\mathbf{x}+\lambda\mathbf{r},t))\ [\mathrm{dB}]}{\lambda[\mathrm{cm}]f[\mathrm{MHz}]}\\ &= \frac{40\pi\Im K/\Re K\ [\mathrm{dB}]}{\lambda[\mathrm{cm}]f[\mathrm{MHz}]}\\ &= \frac{40\pi\omega\eta_{\mathrm{bulk}}/(\rho c^2)\ [\mathrm{dB}]}{\lambda[\mathrm{cm}]f[\mathrm{MHz}]}. \end{aligned} \tag{2.2.16}$$

The analogue derivation refers to **Dukhin2009**.

2.2.2 Lippmann-Schwinger equation

We first define the geometrical configuration suited to breast ultrasound tomography. An imaging domain D set in the n-dimensional real space is surrounded by the transducer array S; see Figure 2.1. The transducer array in our study is assumed to be full transparent, that is to say, the wave continues propagating on its path without the loss of energy. The contrast function denoted by $\chi(\mathbf{x})$ is defined as a function of speed of sound having a compact support in D:

$$\chi(\mathbf{x},\omega) = \begin{cases} \frac{K^2(\mathbf{x},\omega)}{K_0^2(\omega)} - 1, & \mathbf{x}\in D,\\ 0, & \mathbf{x}\in\mathbb{R}^n\backslash D. \end{cases}$$

Combined with Eq. (2.2.14), the speed of sound and the bulk viscosity are given by

$$c = c_0\sqrt{\frac{1+\Re\chi}{(1+\Re\chi)^2+(\Im\chi)^2}}, \tag{2.2.17}$$

$$\eta_{\mathrm{bulk}} = -\frac{\rho c_0^2}{\omega}\frac{\Im\chi}{(1+\Re\chi)^2+(\Im\chi)^2}. \tag{2.2.18}$$

Subtracting Eq. (2.2.6) from Eq. (2.2.2) yields

$$\nabla^2 p^{\mathrm{sct}}(\mathbf{x},\omega) + K_0^2(\omega)p^{\mathrm{sct}}(\mathbf{x},\omega) = -K_0^2(\omega)\chi(\mathbf{x})p(\mathbf{x},\omega). \tag{2.2.19}$$

Note that the scattered wave can be considered as the wavefield emanating from the tissue with the cancellation of the external source term. Moveover, the intensity of the scattered wave is related to the value of the contrast function.

Now we start to formulate the so-called Lippmann-Schwinger equation.

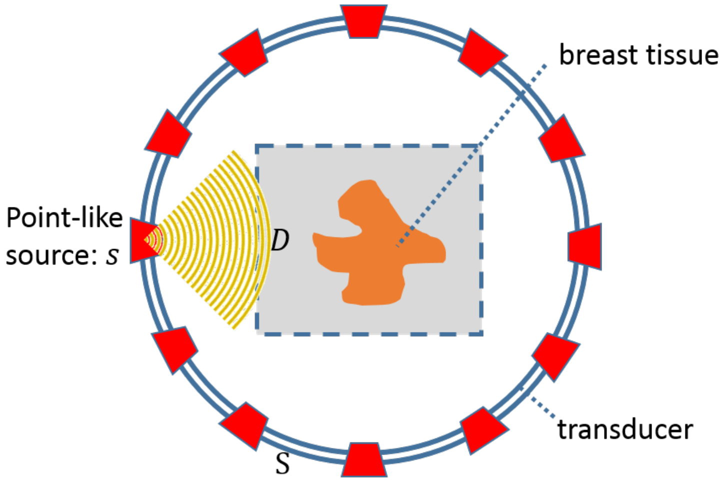

FIGURE 2.1: Schematic diagram of wave propagating in the ring-transducer.

In scattering theory, the Green's representation theorem plays a role in deriving the integral-form expression of the scattered wave $p^{\text{sct}}(\mathbf{x},\omega)$, which can be given as

$$\begin{aligned} p^{\text{sct}}(\mathbf{x},\omega) = & \int_{\partial\Sigma} G(\mathbf{x},\mathbf{y},\omega)\left\{\frac{\partial p^{\text{sct}}(\mathbf{y},\omega)}{\partial\nu_{\mathbf{y}}} - i\kappa p^{\text{sct}}(\mathbf{y},\omega)\right\}\mathrm{d}\sigma(\mathbf{y}) \\ & - \int_{\partial\Sigma} p^{\text{sct}}(\mathbf{y},\omega)\left\{\frac{\partial G(\mathbf{x},\mathbf{y},\omega)}{\partial\nu_{\mathbf{y}}} - i\kappa G(\mathbf{x},\mathbf{y},\omega)\right\}\mathrm{d}\sigma(\mathbf{y}) \\ & + K_0^2(\omega)\int_{\Sigma} G(\mathbf{x},\mathbf{y},\omega)\chi(\mathbf{y})p(\mathbf{y},\omega)\mathrm{d}\mathbf{y}, \end{aligned} \tag{2.2.20}$$

In order to simplify Eq. (2.2.21), we assume that the transducer array is deployed in the far-field and the scattered wave $p^{\text{sct}}(\mathbf{x},\omega)$ also satisfies the Sommerfeld radiation condition (2.2.8). With the assumption, we note that the first and second surface integral terms converge to zero by the Cauchy-Schwartz inequality. The consideration is similar to the proof of Theorem 2.5 in **colton2013inverse**. And incorporated with the compact support in the domain D, finally we conclude our key formula–the Lippmann-Schwinger equation

$$p(\mathbf{x},\omega) = p^{\text{inc}}(\mathbf{x},\omega) + K_0^2(\omega)\int_D G(\mathbf{x},\mathbf{y},\omega)\chi(\mathbf{y})p(\mathbf{y},\omega)\mathrm{d}\mathbf{y}. \tag{2.2.21}$$

2.3 Numerical scheme

Without loss of generality, we fix $\kappa = 1$ and then omit the notation ω in the equation. Indeed, it is done by scaling the spatial variable $\mathbf{x}$, i.e.

$$\tilde{\mathbf{x}} = \kappa \mathbf{x},\ \tilde{p}(\tilde{\mathbf{x}}) = p(\mathbf{x}),\ \tilde{\chi}(\tilde{\mathbf{x}}) = \chi(\mathbf{x}).$$

So for simplicity of notations, we omit the 'tilde' symbol henceforth. The imaging domain D is specified as a square centered at the origin in the heterogeneous medium. And we denote by $\mathbb{J}_N = \{\mathbf{j} = (j_1, j_2) \in \mathbb{Z}^2 \mid -\frac{N}{2} < j_1, j_2 \leq \frac{N}{2}\}$ the index set of grid points $\mathbf{x}_\mathbf{j} = h\mathbf{j}$ in D with the grid size h and the number of points of N in each dimension.

2.3.1 Quadrature method

In the appendix of **ito2013two**, they present a discretised method for Eq. (2.2.21) in the Cartesian coordinate. Multipling χ on both sides of Eq. (2.2.21) and defining $v = \chi p$ yields

$$v(\mathbf{x}) = \chi(\mathbf{x}) p^{\text{inc}}(\mathbf{x}) + \chi(\mathbf{x}) \int_D G(\mathbf{x}, \mathbf{y}) v(\mathbf{y}) \mathrm{d}\mathbf{y} \tag{2.3.1}$$

Then we use the mid-point quadrature rule (the Nystrom methods) that

$$v_\mathbf{k} = \chi_\mathbf{k} p^{\text{inc}}_\mathbf{k} + \chi_\mathbf{k} \sum_{\mathbf{j} \in \mathbb{J}_N} G_{\mathbf{kj}} v_\mathbf{j} h^2 \tag{2.3.2}$$

where $v_\mathbf{k} = v(\mathbf{x_k})$ and $\chi_\mathbf{k} = \chi(\mathbf{x_k})$, and $G_\mathbf{kj}$ is given by

$$G_\mathbf{kj} = \begin{cases} G(\mathbf{x_k}, \mathbf{x_j}) & \mathbf{k} \neq \mathbf{j} \\ \frac{1}{h^2} \int_{(-h/2, h/2)^2} G(\mathbf{x}, \mathbf{0}) \mathrm{d}\mathbf{x} & \mathbf{k} = \mathbf{j} \end{cases} \tag{2.3.3}$$

The discrete spatial convolution can be alleviated with the help of the Fourier transform. Followed with the form of the continuous Fourier transform similar to Eq. (2.3.11), the discrete Fourier transform and inverse discrete Fourier transform denoted by $\mathcal{F}_N$ and $\mathcal{F}_N^{-1}$ having expressions

$$\mathcal{F}_N := \left(\exp(-\frac{2\pi i}{N} \mathbf{k} \cdot \mathbf{j}) \right)_{\mathbf{j}, \mathbf{k} \in \mathbb{J}_N}, \tag{2.3.4}$$

$$\mathcal{F}_N^{-1} := \left(\exp(\frac{2\pi i}{N} \mathbf{k} \cdot \mathbf{j}) \right)_{\mathbf{j}, \mathbf{k} \in \mathbb{J}_N}. \tag{2.3.5}$$

With them, we have the convolution operation for Eq. (2.3.2)

$$v_{\mathbf{k}} = \chi_{\mathbf{k}} p_{\mathbf{k}}^{\text{inc}} + h^2 \chi_{\mathbf{k}} \mathcal{F}_{2N-1}^{-1}\{\mathcal{F}_{2N-1}(G_{\mathbf{k0}})\mathcal{F}_{2N-1}(v_{\mathbf{k}})\}. \tag{2.3.6}$$

First, note that the computational domain is extended to one corresponding to the index set $\mathbb{J}_{2N-1}$ since the Fourier transform of the Green's function $G_{\mathbf{kj}}$. Then $v_{\mathbf{k}}$ should be zero-padding (**press1982numerical**). In this sense, the arithmetic operations and storage of the Fourier transform are the required to be approximate 4 times of that with $\mathbb{J}_N$. Second, the mismatch between the original computational domain and the extended one after doing the inverse Fourier transform $\mathcal{F}_{2N-1}^{-1}$. The index set is required to return to $\mathbb{J}_N$ by restricting the extended domain to D_R.

The linear system (2.3.2) can be solved by any standard numerical solver like GMRES **saad2003iterative**.

2.3.2 Vainikko's solver

In **vainikko2000fast**, Vainikko proposes a numerical solver for solving the Lippmann-Schwinger equation using the collocation method with the trigonometric basis in a periodic spatial domain. It is demonstrated that the Vainikko's solver improves the numerical computing on the accuracy of its optimal convergence order as well as less load of the memory. In terms of complexity, the Vainikko's solver costs $O(MN^2 \log N)$ arithmetical operations through the consideration of explicitly computing the **eigenvalues** of the integral operator in (2.3.1) using fast Fourier transform of the complexity $O(N^2 \log N)$ and additionally conducting the iteration method with approximate M steps.

In this section, I go on using the notation in Section 2.3. The aim is to review the entail details of numerical scheme of the Vainikko's solver. First, the periodization form is given for Eq. (2.3.1). Define $D_R = \{\mathbf{x} = (x_1, x_2) \in \mathbb{R}^2 \mid |x_k| \le R, k = 1, 2\}$ where $R = Nh/2$. We denote by $K(\mathbf{x})$ a new kernel for the integral operator in (2.3.1) which cuts off the Green function $G(\mathbf{x}, \mathbf{y}) := G(|\mathbf{x} - \mathbf{y}|)$

$$K(\mathbf{x}) = \begin{cases} G(|\mathbf{x}|) & |\mathbf{x}| \le R, \\ 0 & |\mathbf{x}| > R \text{ and } \mathbf{x} \in D_R \end{cases} \tag{2.3.7}$$

Then we can extend functions $f(\mathbf{x})$, $K(\mathbf{x})$, $v(\mathbf{x})$ and $u(\mathbf{x})$ from D_R to $\mathbb{R}^2$ as $2R$-periodic functions in each dimensions. Therefore Eq. (2.3.1) is rewritten as

$$v(\mathbf{x}) = v^{\text{inc}}(\mathbf{x}) + \chi(\mathbf{x}) \int_{D_R} K(\mathbf{x} - \mathbf{y}) v(\mathbf{y}) d\mathbf{y}, \mathbf{x} \in D_R \tag{2.3.8}$$

where $v^{\mathrm{inc}}(\mathbf{x}) = \chi(\mathbf{x})p^{\mathrm{inc}}(\mathbf{x})$.

Next we intend to discretize the solution $v(\mathbf{x})$ in the periodic space $L^2(D)$. The trigonometric orthonormal basis of $L^2(D)$ is shown as follows

$$\varphi_{\mathbf{j}}(\mathbf{x}) = (2R)^{-1}e^{i\pi\mathbf{j}\cdot\frac{\mathbf{x}}{R}} \tag{2.3.9}$$

where $\mathbf{j} = (j_1, j_2) \in \mathbb{Z}^2$. Then we project $v(\mathbf{x})$ onto the finite space $\tau_N = \mathrm{span}\{\varphi_{\mathbf{j}} \in L^2(D) \mid \mathbf{j} \in \mathbb{J}_N\}$ by the orthogonal projection P_N

$$v_N := P_N v = \sum_{\mathbf{j}\in\mathbb{J}_N} \hat{v}(\mathbf{j})\varphi_{\mathbf{j}}. \tag{2.3.10}$$

Here the Fourier coefficients of v are given by

$$\hat{v}(\mathbf{j}) = \int_D v(\mathbf{x})\overline{\varphi_{\mathbf{j}}(\mathbf{x})}d\mathbf{x}. \tag{2.3.11}$$

We also define an interpolation operator $Q_N : L^2(D) \to \tau_N$ which satisfies

$$(Q_N v)(h\mathbf{j}) = v(h\mathbf{j}).$$

With the collocation method, Eq. (2.3.8) discretized by

$$P_N Q_N v = P_N Q_N v^{\mathrm{inc}} + P_N Q_N(\chi K v) \tag{2.3.12}$$

or briefly

$$\underline{v}_N = \underline{v^{\mathrm{inc}}}_N + \underline{\chi}_N\, \underline{Kv}_N \tag{2.3.13}$$

where the underline of symbol represents the nodal values on $\mathbb{J}_N$.

From the Fourier transforms in Eq. (2.3.4) and (2.3.5), we have $\underline{\hat{v}}_N = \frac{2R}{N^2}\mathcal{F}_N\underline{v}_N$ and $\underline{v}_N = \frac{1}{2R}\mathcal{F}_N^{-1}\underline{\hat{v}}_N$. By using the above two formulas and the convolution theorem of Fourier transform, we finally obtain the computing linear systems

$$\underline{v}_N = \underline{v^{\mathrm{inc}}}_N + \underline{\chi}_N\mathcal{F}_N^{-1}\underline{\hat{K}}_N\mathcal{F}_N\underline{v}_N. \tag{2.3.14}$$

The diagonal matrix $\underline{\hat{K}}_N$ can be explicitly computed by

$$\begin{aligned} \underline{\hat{K}}_N(\mathbf{j}) &= \frac{R\left(1 + \frac{i\pi}{2}\left(\pi|\mathbf{j}|J_1(\pi|\mathbf{j}|)H_0^{(1)}(R) - RJ_0(\pi|\mathbf{j}|)H_1^{(1)}(R)\right)\right)}{2(\pi^2|\mathbf{j}|^2 - R^2)} && (2.3.15)\\ &\quad \text{when } \mathbf{j} \neq \mathbf{0}, \\ \underline{\hat{K}}_N(\mathbf{0}) &= -(2R)^{-1} + \frac{\pi i}{4}H_1^{(1)}(R) && (2.3.16) \end{aligned}$$

for $\pi|\mathbf{j}| \neq R$ and

$$\underline{\hat{K}}_N(\mathbf{j}) = \frac{\pi R i}{8}\left(J_0(R)H_0^{(1)}(R) + J_1(R)H_1^{(1)}(R)\right) \tag{2.3.17}$$

for $\pi|\mathbf{j}| = R$.

2.4 Verification of the numerical schemes

In terms of the application of the Lippmann-Schwinger equation in USCT, its solver should have common characteristics of rapidness as well as accuracy since the inverse problem of USCT is usually solved by means of recurrently calculating the numerical forward problem. However, it is hard to achieve in the case of large wavenumbers (or a high frequency). First, in ultrasound breast imaging, the computational cost is burdensome for the requirement of much more number of grid points due to the fact that the imaging domain contains the order of 100 wavelength in each dimension. Besides, in the literature (**Chen2013**) , the Helmholtz equation or the Lippmann-Schwinger equation suffers from the severe oscillation for large wavenumbers. And consequently the so-called "pollution effect" occurs, i.e. the accuracy of the numerical solution deteriorates rapidly as the wavenumber increases. Unfortunately, ref (p e) indicate that in two dimensions, the pollution effect happening in the Helmholtz solver can be minimized but not eliminated. Therefore, a compromise is made to find an acceptable solver for the scenario of USCT for breast imaging instead of developing an optimal one.

The post section shows that one can benefit from the easy implementation of the quadrature method while the Vainikko's solver have merits of less number of grid points as well as the optimal convergence rate. But in this section, a verification test are conducted to display the behaviors of the quadrature method and the Vainikko's solver with different choices of the number of grid points and the wavenumbers. In addition, the wave field traversing in a breast phantom is simulated with both of the solvers in large wavenumbers. The selection of the numerical forward solver of the Lippmann-Schwinger equation is based on the performed numerical results.

2.4.1 Configuration

Two numerical tests are shown to display the behavior of the quadrature method and the Vainikko's solver. In the first example, the wave propagates through the circular scatterer B and the measurements of the scattered wave are only recorded on a ring transducer S surrounding B. One can set that B is homogeneous with the speed of sound of 1470 m/s and the radius of 0.01 m. The ring has a radius of 0.05 m and consists of 256 equi-spaced sensor elements. The background speed of sound is 1540 m/s. The imaging domain D is a square region centered at the origin with an area of 0.06×0.06 m^2. In Appendix A, one has shown that the wavefield of the circular scatterer has an exact solution for Eq. (2.2.21). Hence, one can assess the accuracy of the aforementioned numerical methods through the comparison with the exact wavefield.

2.4.2 Example one: a circular scatterer

In this section, three groups of the numerical tests are shown to display the accuracy of the quadrature method and the Vainikko's solver. In Table 2.1, the first test shows the relationship between the relative error and the frequency. Tables 2.4, 2.5 show the total and scattered wavefield with respect to distinct frequencies. It indicates the result that the increasing of the frequency amplifies the relative error in spite of a fixed point per wavelength (PPW) of 20. Moreover, the growth of the relative error for the Vainikko's solver is much faster than that for the quadrature method. The second test is carried out on varying PPW with two frequencies, one is 0.04 MHz and the other is 0.64 MHz in Tables 2.2, 2.3, 2.6, 2.7, 2.8, 2.9. Especially in the case of the frequency of 0.64 MHz, the increasing of PPW by applying the quadrature method can enhance the accuracy of the numerical solution whilst that by applying the Vainikko's solver doesn't have significant effect.

TABLE 2.1: Relative error of the numerical solution applying the quadrature and Vainikko's solver for the circular scatterer with varying frequencies and a fixed 20 PPW.

Frequency (MHz)	grid numbers	p in D		p^{sct} on S	
		Quadrature	Vainikko	Quadrature	Vainikko
0.01	8×8	0.0159	0.1534	0.2757	0.0883
0.02	16×16	0.0096	0.1532	0.0568	0.0646
0.04	31×31	0.0136	0.0122	0.0440	0.1141
0.08	62×62	0.0132	0.1603	0.0368	0.1593
0.16	125×125	0.0227	0.0567	0.0461	0.2946
0.32	249×249	0.0437	0.2108	0.0784	0.5802
0.64	499×499	0.0913	0.7461	0.1513	1.2060
1.28	997×997	0.1837	1.9467	0.3507	3.1341

TABLE 2.2: Relative error of the numerical solution applying the quadrature and Vainikko's solver for the circular scatterer with varying PPW and a fixed frequency of 0.04 MHz.

PPW	grid numbers	p in D		p^{sct} on S	
		Quadrature	Vainikko	Quadrature	Vainikko
2	3×3	0.6041	0.5781	1.5536	1.3891
5	8×8	0.0743	0.6071	0.2672	0.1388
10	16×16	0.0224	0.3079	0.0653	0.1141
20	31×31	0.0132	0.0118	0.0443	0.1138
40	62×62	0.0040	0.0808	0.0141	0.0981
80	125×125	0.0020	0.0053	0.0043	0.0983
160	249×249	0.0009	0.0054	0.0011	0.1009

TABLE 2.3: Relative error of the numerical solution applying the quadrature and Vainikko's solver for the circular scatterer with varying PPW and a fixed frequency of 0.64 MHz.

PPW	grid numbers	p in D		p^{sct} on S	
		Quadrature	Vainikko	Quadrature	Vainikko
2	50×50	0.4962	1.7404	0.9619	1.5666
5	125×125	0.2288	0.7329	0.4173	1.2069
10	249×249	0.1477	0.7351	0.2610	1.2070
20	499×499	0.0898	0.7345	0.1513	1.2051
40	997×997	0.0501	0.7346	0.0813	1.2052
80	1995×1995	0.0265	0.7346	0.0420	1.2052

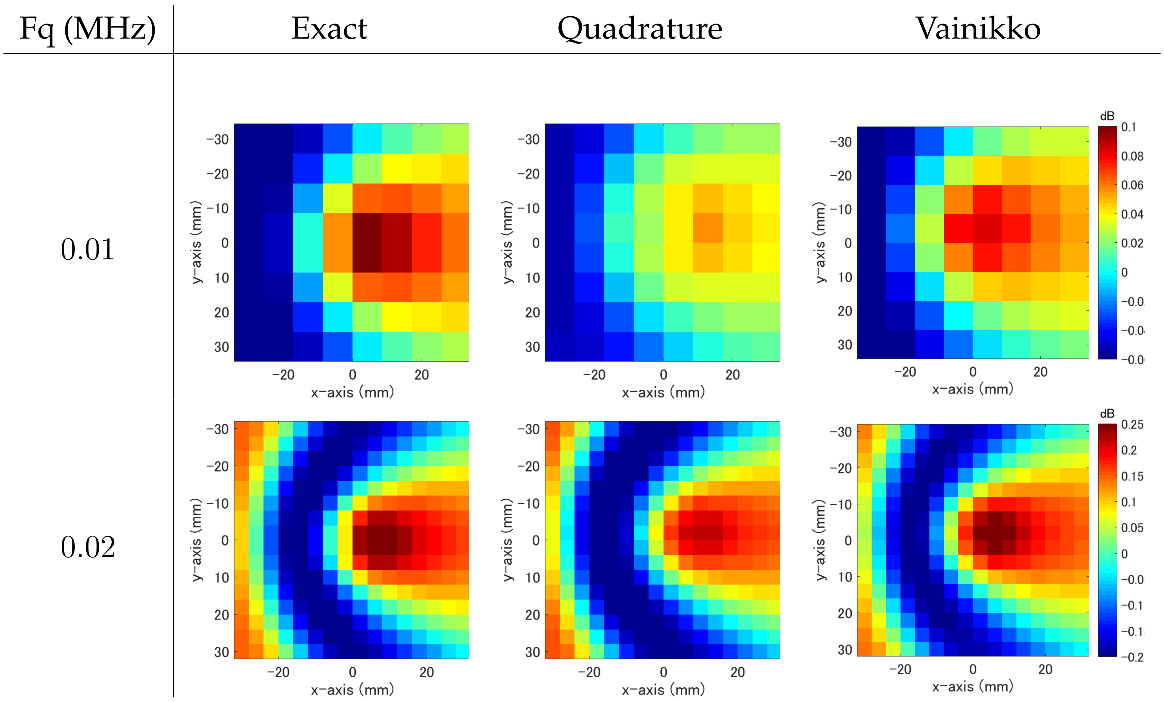

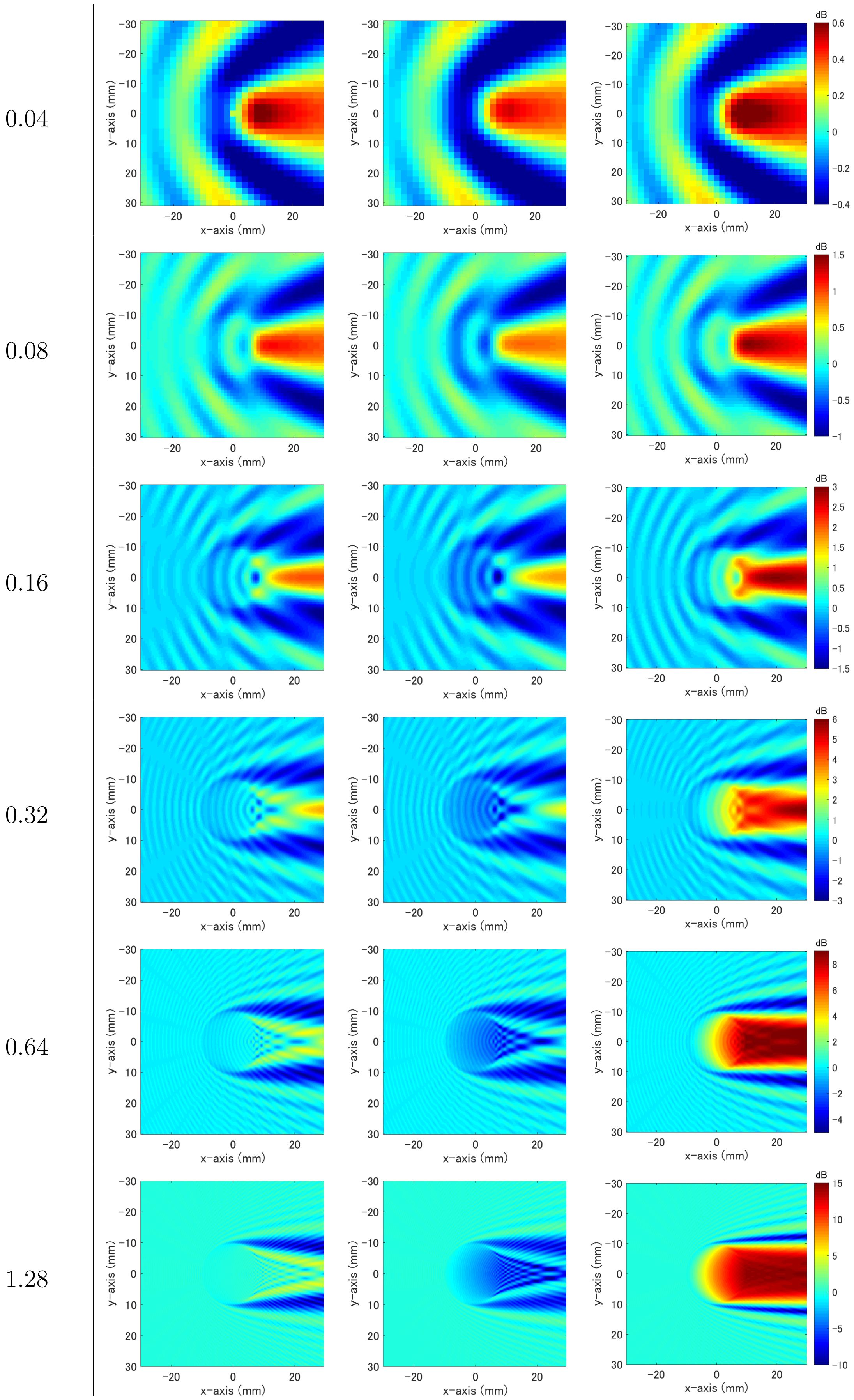
0.04
0.08
0.16
0.32
0.64
1.28
y−axis (mm)
x−axis (mm)
−30
−20
−10
0
10
20
30
−20
0
20
dB
0.6
0.4
0.2
0
−0.2
−0.4
1.5
1
0.5
0
−0.5
−1
3
2.5
2
1.5
1
0.5
0
−0.5
−1
−1.5
6
5
4
3
2
1
0
−1
−2
−3
8
6
4
2
0
−2
−4
15
10
5
0
−5
−10

TABLE 2.4: Numerical solution of the total wavefield applying the exact solution, the quadrature method, and the Vainikko's solver for the circular scatterer with varying frequencies and a fixed 20 PPW.

Fq (MHz)	Exact	Quadrature	Vainikko
0.01	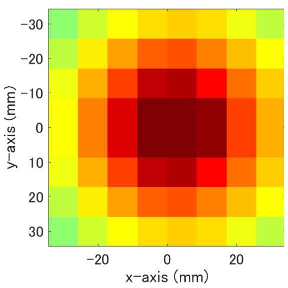	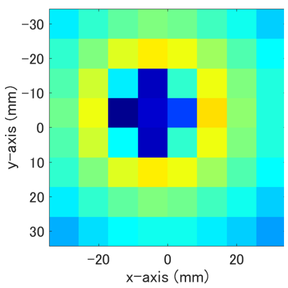	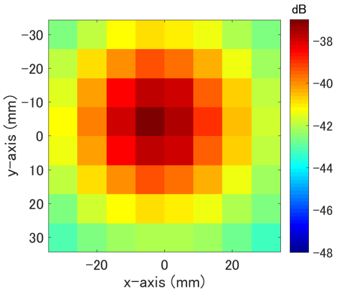
0.02	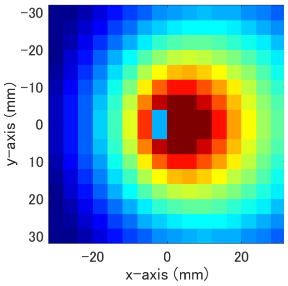	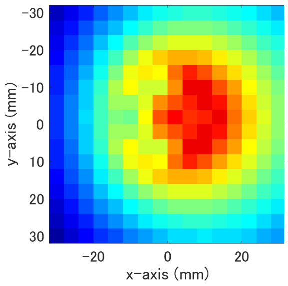	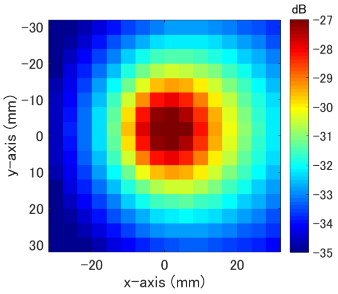
0.04	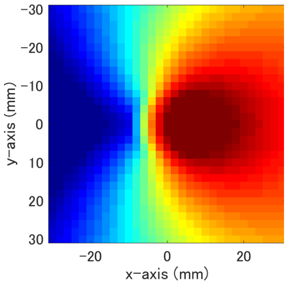	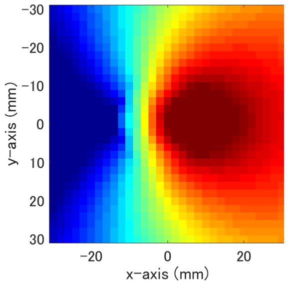	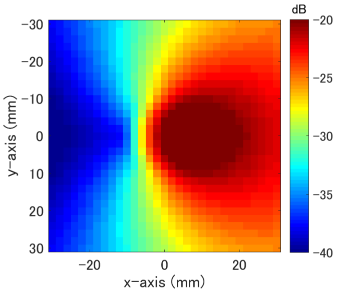
0.08	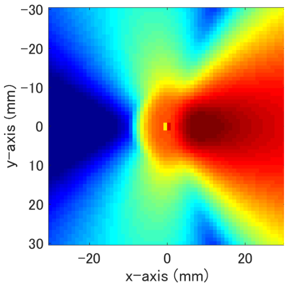	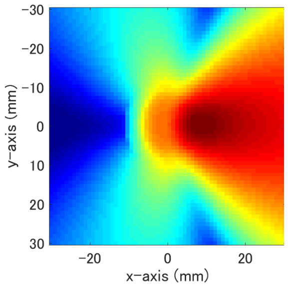	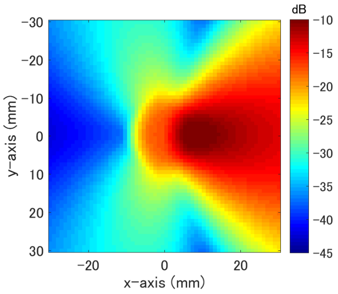
0.16	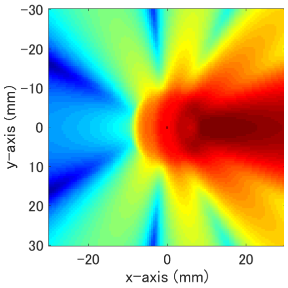	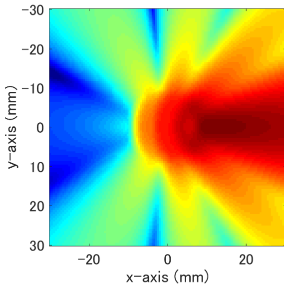	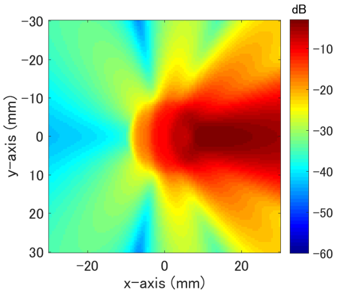

0.32	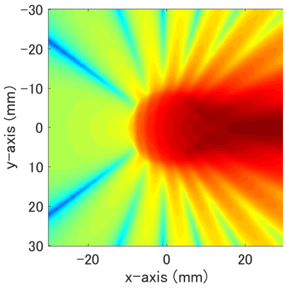	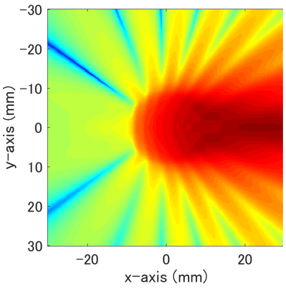	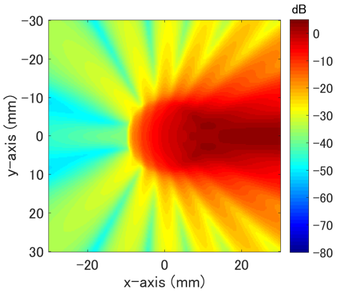
0.64	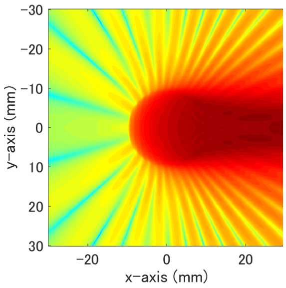	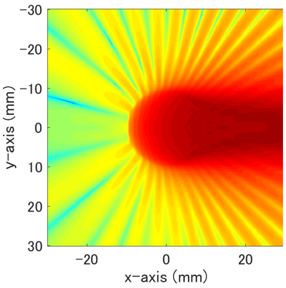	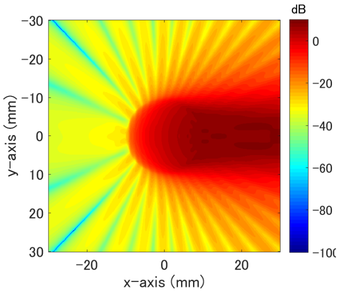
1.28	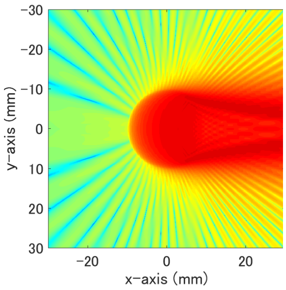	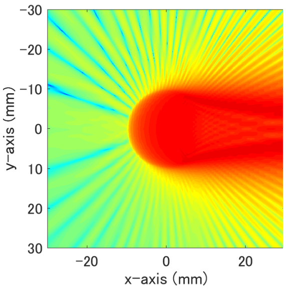	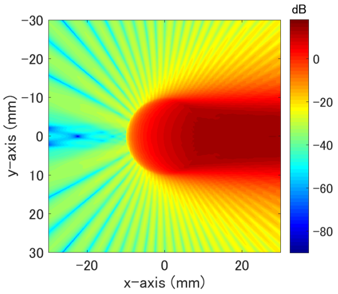

TABLE 2.5: Numerical solution of the scattered wavefield applying the exact solution, the quadrature method, and the Vainikko's solver for the circular scatterer with varying frequencies and a fixed 20 PPW.

PPW	Exact	Quadrature	Vainikko
5	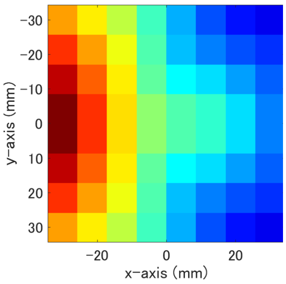	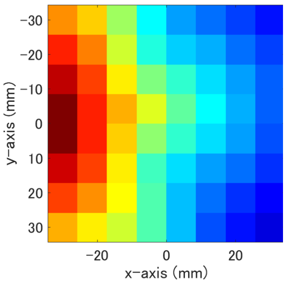	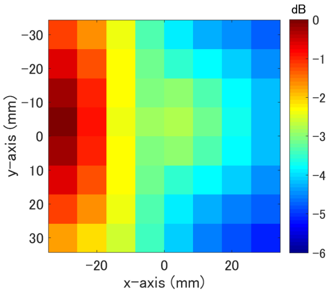
10	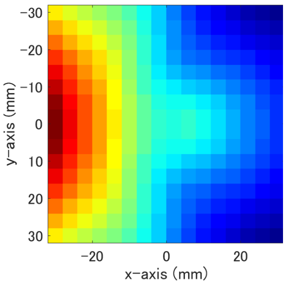	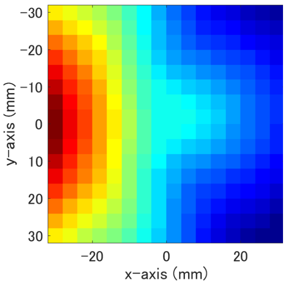	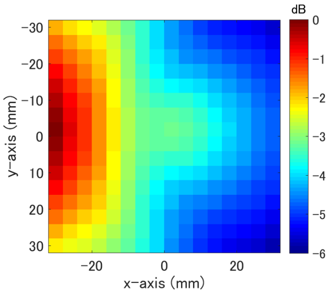

20	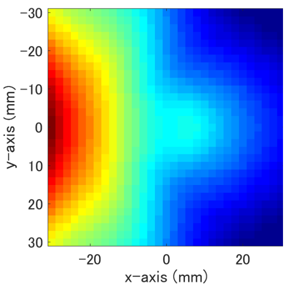	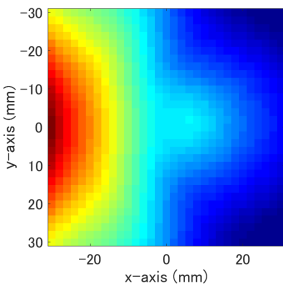	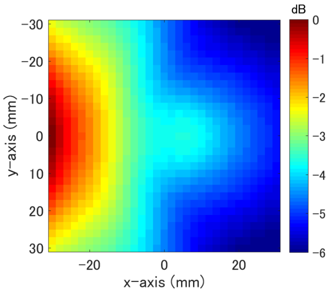
40	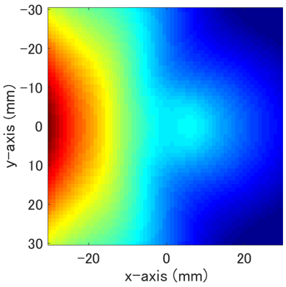	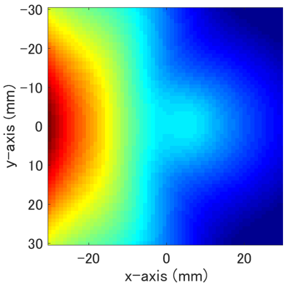	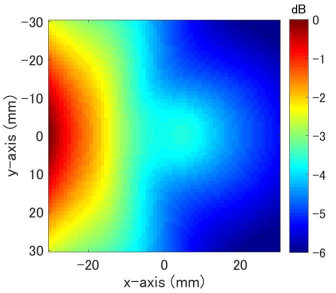
80	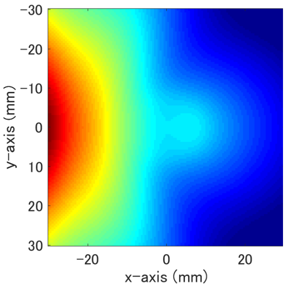	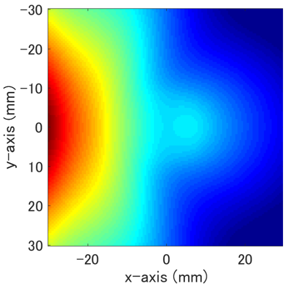	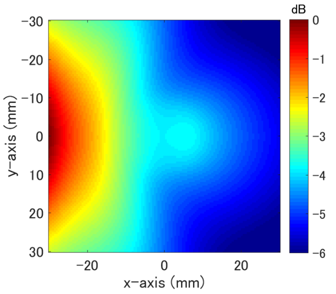
160	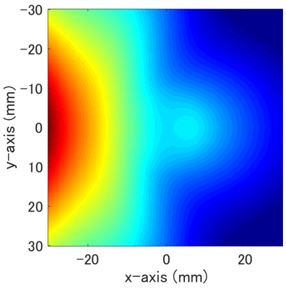	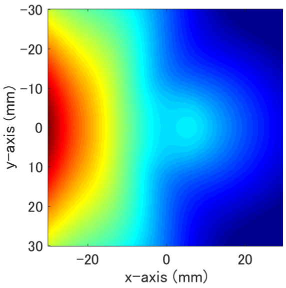	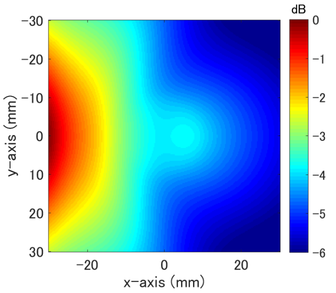

TABLE 2.6: Numerical solution of the total wavefield applying the exact solution, the quadrature method, and the Vainikko's solver for the circular scatterer with varying PPW and a fixed frequency of 0.04 MHz.

PPW	Exact	Quadrature	Vainikko
5	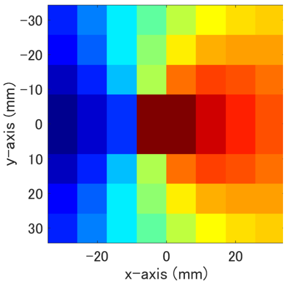	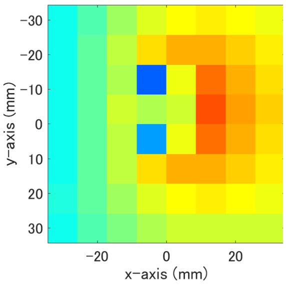	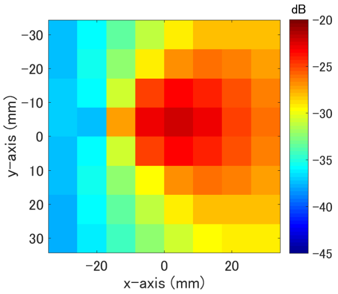

10	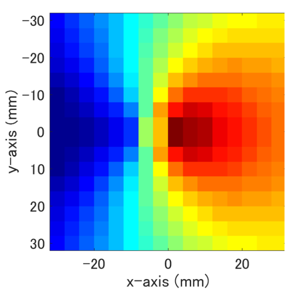	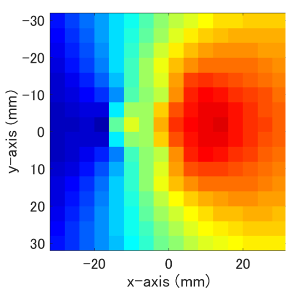	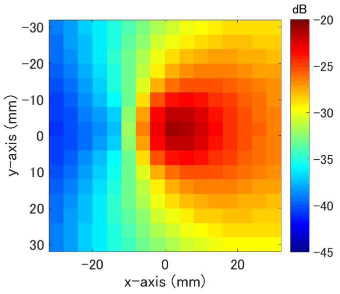
20	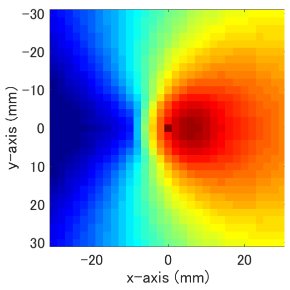	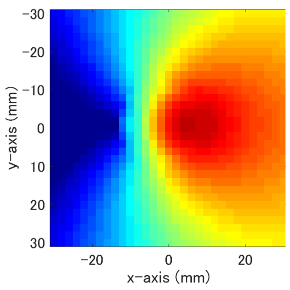	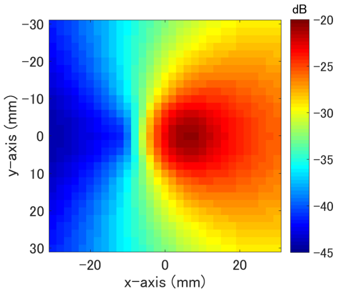
40	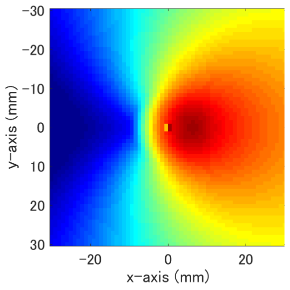	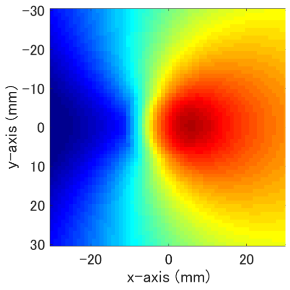	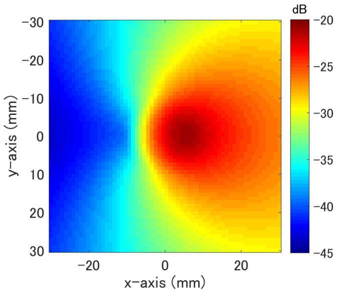
80	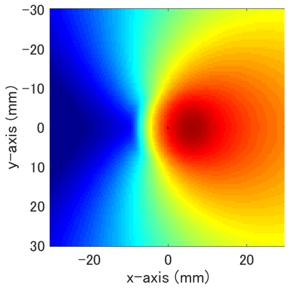	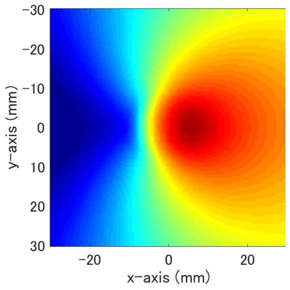	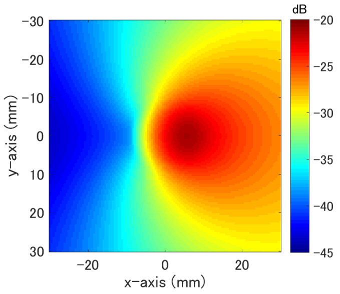
160	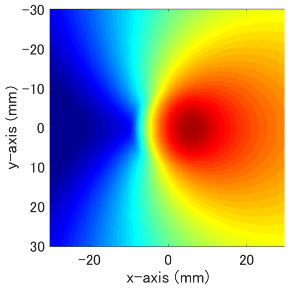	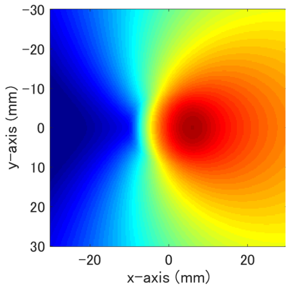	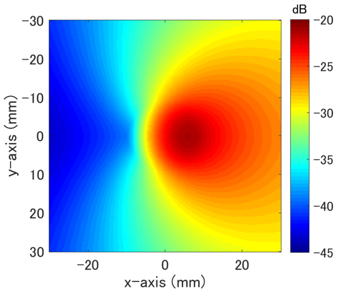

TABLE 2.7: Numerical solution of the scattered wavefield applying the exact solution, the quadrature method, and the Vainikko's solver for the circular scatterer with varying PPW and a fixed frequency of 0.04 MHz.

PPW	Exact	Quadrature	Vainikko

PPW	Exact	Quadrature	Vainikko
5	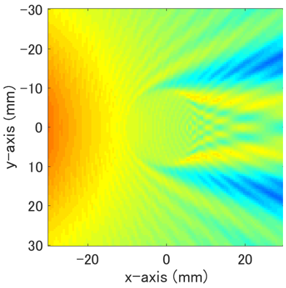	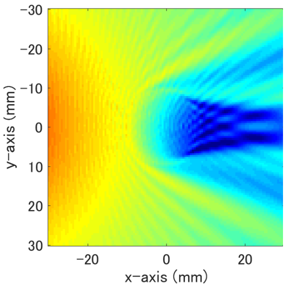	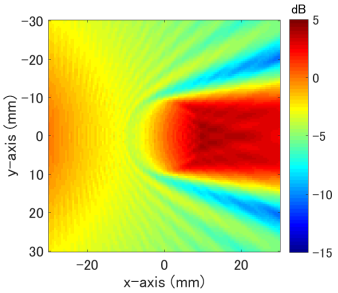
10	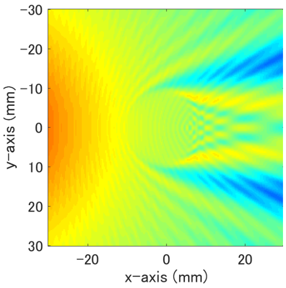	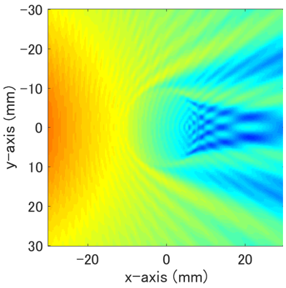	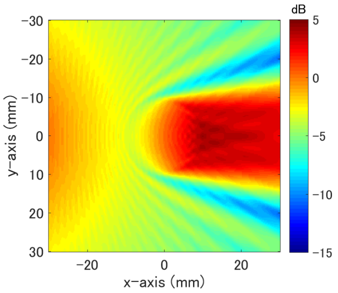
20	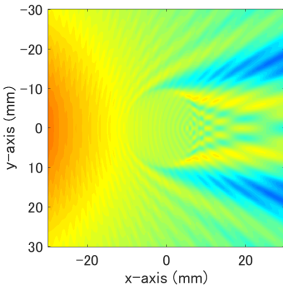	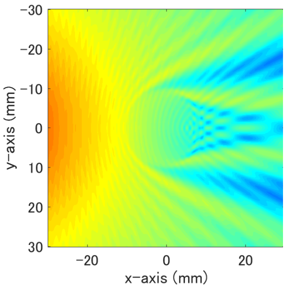	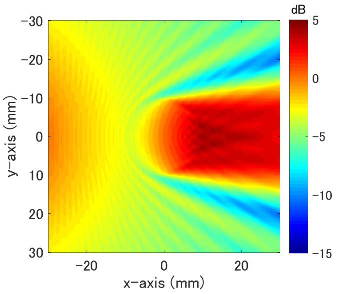
40	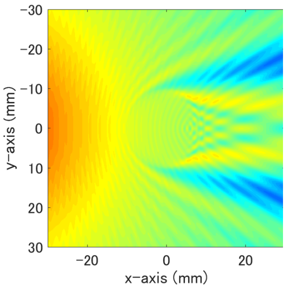	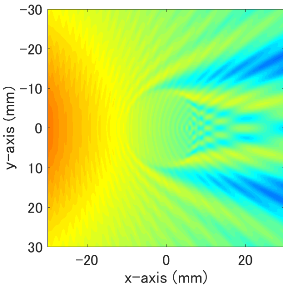	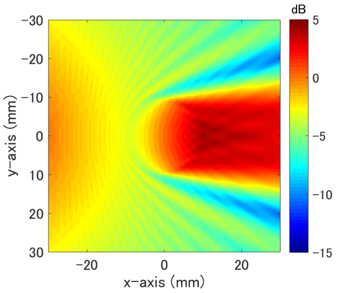
80	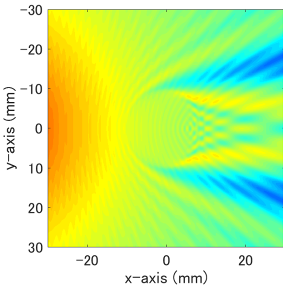	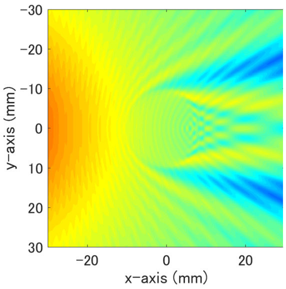	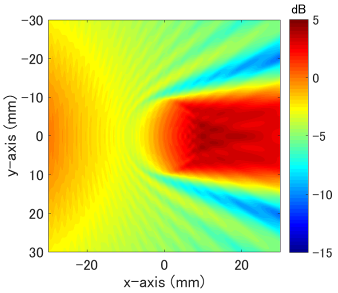

TABLE 2.8: Numerical solution of the total wavefield applying the exact solution, the quadrature method, and the Vainikko's solver for the circular scatterer with varying PPW and a fixed frequency of 0.64 MHz.

5	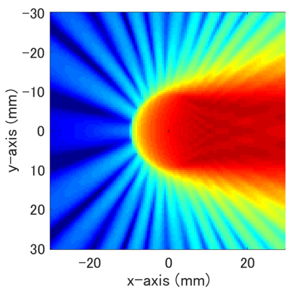	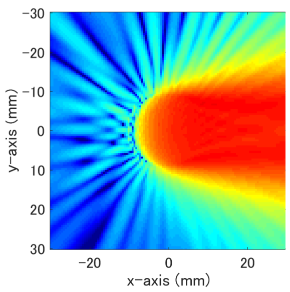	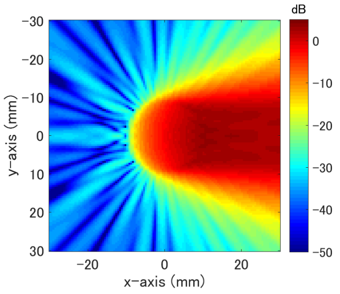
10	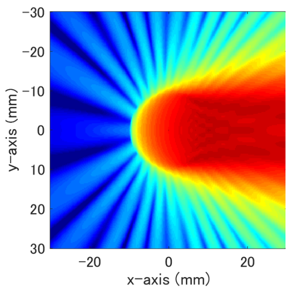	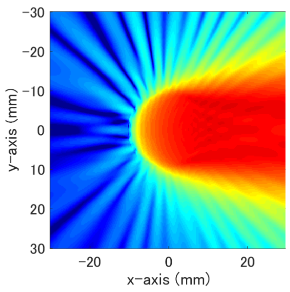	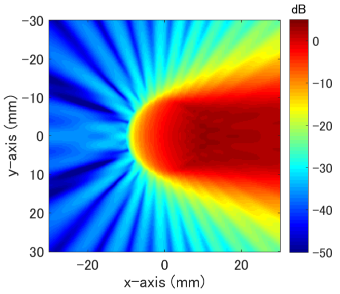
20	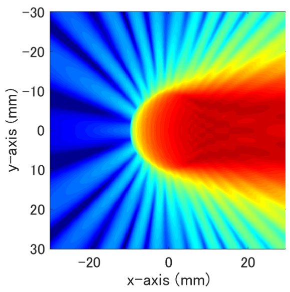	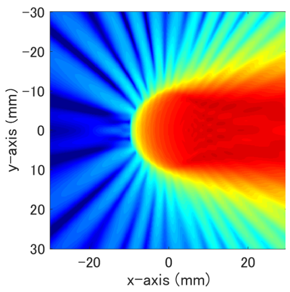	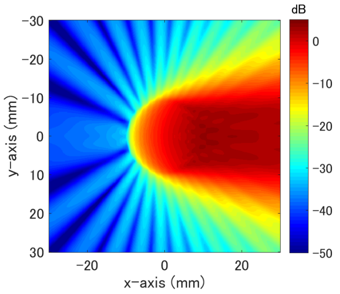
40	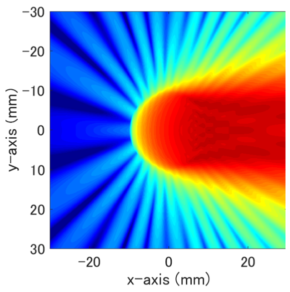	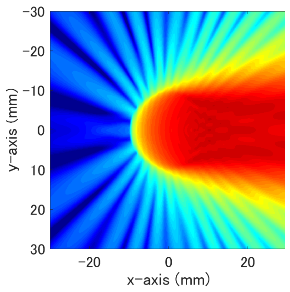	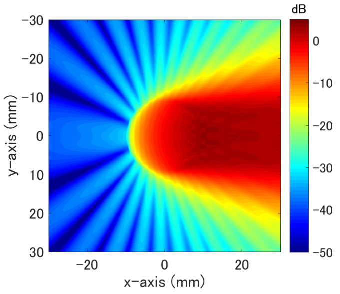
80	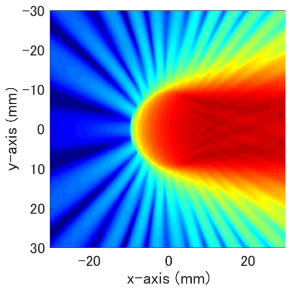	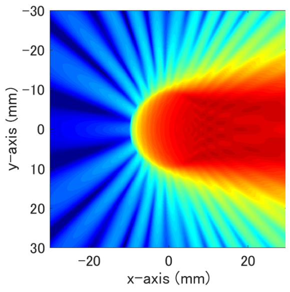	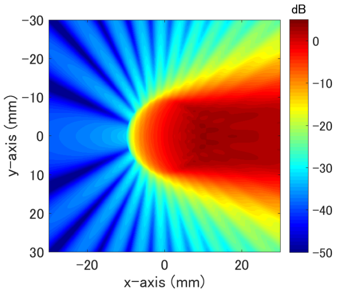

TABLE 2.9: Numerical solution of the scattered wavefield applying the exact solution, the quadrature method, and the Vainikko's solver for the circular scatterer with varying PPW and a fixed frequency of 0.64 MHz.

2.5 Discussion and conclusion

According to the theoretical and numerical study, the better choice of the numerical method for solving the attenuated wave equation is the quadrature method. Despite the need of four times of the grid points for the quadrature method than that for the Vainikko's solver, the acceptable accuracy of the numerical solution is attained with the scenario of the similar frequency with respect to the ultrasound device.

From Section 2.5, the previous numerical solvers will be invalid when given a higher value of the wave number, which is the larger number of wavelength in our physical domain. This can be base on the theory in **Babuska1997** that shows the two-dimensional Helmholtz equation will encounter with a so-called pollution effect and can reduce it but not avoid it. Pollution effect indicates the numerical solver of the two-dimensional Helmholtz equation is invalid when k^2h is not small enough, where k is the wave number and h the grid size. Actually, kh represents points per wavelength and some references recommend kh be $10 - 60$; see **babuska2000pollution**; **alles2011perfectly**. For higher-order numerical scheme , see **aguilar2004high**; **aguilar2002high**; **kapur1997high**.

Chapter 3

Inverse problems: contrast source inversion

3.1 Introduction

Ultrasound computed tomography (USCT) for breast cancer diagnosis has recently become popular because of the development of a diagnostic prototype equipped with ring-array transducers (**Qu2015a**; **Qu2015b**; **qu2016phase**; **tamano2015compensation**) and the rapid improvement of computing hardware. In terms of USCT imaging methods, several works (**greenleaf1983computerized**; **avinash2001principles**; **natterer1986themathematics**; **li2009improved**; **Qu2015a**; **Qu2015b**) have focused on the ray-based reconstruction of sound-speed images of the breast tissue, yielding a low-resolution blurring result owing to the diffraction effects being ignored. On the other hand, waveform inversion, which is based on the wave equation retaining the integrated feature of ultrasound, generates higher-resolution images, but is very time-consuming because of a large number of iterations and a markedly high computing cost at each iteration (**roy2010sound**; **li2014toward**; **wang2015waveform**; **sandhu2015frequency**). To enhance the performance of USCT, frequency-domain full waveform inversion, or the inverse medium problem (**colton2013inverse**), is introduced to overcome these difficulties by exploiting the wave theory in the frequency domain. It produces high-accuracy images of the breast tissue compared with ray-based reconstruction and has a relatively low computing cost compared with the waveform inversion in the time domain (**alles2011perfectly**). Hence, using frequency-domain full waveform inversion will greatly help the diagnosis of breast cancer at an early stage.

The contrast source inversion (CSI) method, first proposed in **van1997contrast**, is used to linearize the original nonlinear full waveform inversion model by adding a new variable, namely, a contrast source. The merit of the CSI method lies in the direct solution of a two-objective optimization problem for sound speed without utilizing the forward solver of the wave equation. Afterwards, several robust CSI methods were developed in order to diminish the error of data fidelity terms caused by noise data. The total-variation (TV) CSI method together with additive and multiplicative TV penalty terms is considered (**van1999extended**). Moreover, for application in breast cancer diagnosis, the TV penalty term with an L^1 norm is preferred because it preserves more edge information in reconstructed images (**rudin1992nonlinear**; **li2009breast**; **li2009vivo**). The CSI method with a finite-difference approach (**abubakar2008finite**) is introduced to solve the iteration scheme of the CSI method using the finite-difference solver instead of an integral operator. Recently, **ozmen2014ultrasound**; **ozmen2015comparing** have compared the currently popular breast imaging algorithms and concluded that the CSI method yields the highest-resolution medical images for the sound-speed reconstruction of the breast tissue.

As a reference of the modality of the robust CSI methods, one can refer to general studies on inverse problems and regularization methods in **engl1996regularization** and **kaltenbacher2008iterative**. Fundamentally, the regularization methods have the following three aspects: the data fidelity term derived from the original model, the penalty term depending on which property you expect the solution to be endowed with, and the choice rule of regularization parameters. We may face several difficulties while utilizing the regularization methods from the conventional points: (1) determination of the unknown noise level in practice; (2) determination of the regularization parameter prior to the execution of the algorithm. Some papers propose that regularization parameters can be chosen automatically with a known noise level (**ito1992choice**; **kunisch1998iterative**; **xie2002improved**; **lu2010model**), whereas the automatic choice rule can be developed when there is a lack of information on the noise level (**hansen1992analysis**; **hansen1993use**; **clason2010duality**; **clason2010semismooth**; **Heng2010model**).

In this work, we mainly study an integrated approach by which an automatic choice rule of regularization parameters is merged with the robust CSI method together with an L^1 TV-regularization term. The use of the automatic choice rule of regularization parameters is a heuristic way to (1) reconstruct high-resolution medical images and (2) enhance the robustness of the CSI method without *a priori* information on the noise level. Additionally, we observe that this integrated method provides an $O(1/k)$ sublinear rate of convergence. In prior research, **van2001contrast** showed that the numerical solutions solved by the CSI method and its extensions probably converge to a global minimum with a large total number of sources. We replace the outer iteration of the robust CSI method with the alternating minimization algorithm, so that we can estimate the convergence rate by the convergence analysis described in **beck2013ontheconvergence** and **beck2015convergence**.

This paper is organized as follows. In Sect. 2, we start with a mathematical formulation of the USCT problem and the robust CSI method. In Sect. 3, we study the alternating minimization algorithms together with the automatic choice rule of regularization parameters in detail. In Sect. 4, we show a numerical result of reconstructing a real medical phantom by the above methodology. The conclusions and future work are given in Sect. 5.

3.2 Notation and mathematical formulation

We list the notations to be used as follows. The square-bracket function represents a functional while the round-bracket function is normally a function. The semicolon inside a "function" separates the variables into the unknowns in the front and the knowns in the back. The bar over a variable represents a complex conjugate and the asterisk with an operator denotes its adjoint operator.

To formulate the USCT problem for the ring-array transducers (**tamano2015compensation**) shown in Fig. 3.1, we consider a case in which a breast tissue placed in a rectangular domain $D \subset \mathbb{R}^2$ is immersed in a homogeneous background medium filling the entire two-dimensional space. The domain D is surrounded by the ring-array transducers with the function of sources and receivers on the curve $S \subset \mathbb{R}^2$. The Lippmann-Schwinger equation (**colton2013inverse**) governing the acoustic-wave propagation of the USCT problem gives the scattered field of a pressure wave through the integral equation with the spatial variable $\xi \in \mathbb{R}^2$:

$$p_m(\xi) - p_m^{\mathrm{inc}}(\xi) = \kappa^2 \int_{\mathbb{R}^2} G(\xi, \mathbf{y})\chi(\mathbf{y})p_m(\mathbf{y})\mathrm{d}\mathbf{y}, \tag{3.2.1}$$

where $m = 1, 2, \cdots, N$ represents the source number, N the number of sources, and $p_m(\xi)$ the total wave field of the mth source. The function $\Phi(\xi, \mathbf{y})$ is the free-space Green's function of the homogeneous Helmholtz equation of the wavenumber k, which is given by a zero-order Hankel function of the 1st kind:

$$G(\xi, y) = \frac{i}{4} H_0^{(1)}(\kappa|\xi - \mathbf{y}|).$$

The spherical incident wave field is denoted by $p_m^{\text{inc}}(\xi) = \Phi(\xi, \mathbf{s_m})$, where $\mathbf{s_m} \in S$ is the location of the source for $m = 1, 2, \cdots, N$. The contrast $f(\xi)$ has a compact support in D expressed as

$$\chi(\xi) = \begin{cases} \frac{c_0^2}{c^2(\xi)} - 1, & \xi \in D, \\ 0, & \xi \in \mathbb{R}^2 \backslash D, \end{cases}$$

where $c(\xi)$ and c_0 are the sound speed in the breast tissue and the homogeneous background, respectively. Hence, the USCT problem is to recover $\chi(\xi)$ in D from the Lippmann-Schwinger equation (3.2.1) given the data $p_m(\mathbf{s})$ on the boundary $\mathbf{s} \in S$, in which all sources and receivers are located, corresponding to the incident wave field $p_m^{\text{inc}}(\xi)$ in $\mathbb{R}^2$.

To solve this nonlinear inverse problem, one can linearize it with the substitution of an auxiliary function – contrast source $v_m(\xi) := p_m(\xi)\chi(\xi)$ in Eq. (3.2.1) and restrict ξ in S denoted by s, which yields the data equation of the linear form with respect to the contrast source $v_m(\mathbf{s})$ on S and scattered-field boundary data $g_m(\mathbf{s})$:

$$\begin{aligned} g_m(\mathbf{s}) = p_m(\mathbf{s}) - p_m^{\text{inc}}(\mathbf{s}) = \chi^2 \int_D G(\mathbf{s}, \mathbf{y}) v_m(\mathbf{y}) d\mathbf{y} \\ := G^S v_m(\mathbf{s}), \mathbf{s} \in S, \end{aligned} \tag{3.2.2}$$

where $m = 1, 2, \cdots, N$. On the other hand, the state equation is obtained by multiplying both sides of Eq. (3.2.1) by $\chi(\mathbf{x})$ and restricting the spatial variable ξ in D denoted by $\mathbf{x}$, which yields

$$\begin{aligned} v_m(\mathbf{x}) - \chi(\mathbf{x}) p_m^{\text{inc}}(\mathbf{x}) = \kappa^2 \chi(\mathbf{x}) \int_D G(\mathbf{x}, \mathbf{y}) v_m(\mathbf{y}) d\mathbf{y} \\ := \chi(\mathbf{x}) G^D v_m(\mathbf{x}), \mathbf{x} \in D, \end{aligned} \tag{3.2.3}$$

where $m = 1, 2, \cdots, N$.

The robust CSI method here is introduced to solve Eqs. (3.2.2) and (3.2.3) together for the unknown contrast $\chi(\mathbf{x})$ and the contrast sources $\{v_m(\mathbf{x})\}_{m=1}^N$ in D by minimizing the following cost functional:

$$\begin{aligned} J[\chi, v_1, \cdots, v_N, \gamma] = \sum_{m=1}^{N} \|\chi G^D v_m - v_m + \chi p_m^{\text{inc}}\|_{L^2(D)}^2 \\ + \frac{\mu_D[\chi]}{\mu_S} \sum_{m=1}^{N} \|G^S v_m - g_m\|_{L^2(S)}^2 + \gamma \|\nabla \chi\|_{L^1(D)}, \end{aligned} \tag{3.2.4}$$

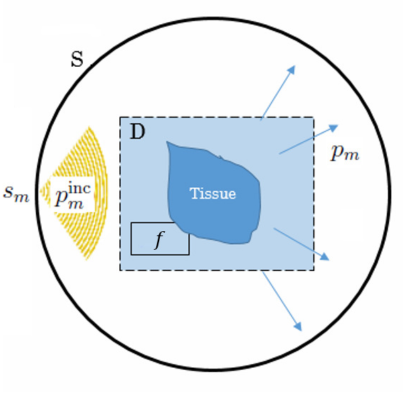

FIGURE 3.1: (Color online) USCT problem with the ring-array transducers.

with the coefficients

$$\mu_S = \sum_{m=1}^{N} \|g_m\|_{L^2(S)}^2, \ \mu_D[\chi] = \sum_{m=1}^{N} \|\chi p_m^{\text{inc}}\|_{L^2(D)}^2, \tag{3.2.5}$$

and the regularization parameter γ. In this paper, we assume that the measured data $\{g_m\}_{m=1}^N$ are noisy without any information on the noise level, considering medical applications. Hereinafter, the spatial variable for each function will be omitted if their definition domains are clear.

Note that we need several assumptions to ensure that the robust CSI method is soluble. We assume that the number of sources N is large such that $\sum_{m=1}^N \|p_m\|_{L^2(D)}^2 \gg \|f\|_{L^2(D)}^2$. Under this assumption, we then conclude that the contrast sources $\{v_m\}_{m=1}^N$ and the measured data $\{g_m\}_{m=1}^N$ have large values in the L^2 sense from their definitions and Eq. (3.2.2).

3.3 Algorithm

We will study the alternating minimization algorithms as the outer iteration for solving the robust CSI method in Sect. 3.3.1. In Sect. 3.3.2, we show the numerical implementation of the inner iteration in the alternating minimization algorithms. In Sect. 3.3.3, we introduce the numerical scheme for the automatic choice rule and discuss its convergence. In Sect. 3.3.4, we present the compound convergence theorem for the alternating minimization algorithms with the automatic choice rule.

3.3.1 Outer iteration

In this section, we construct a concrete algorithm for the robust CSI method described by Eq. (3.2.4). For the outer iteration, an alternative way of switching the iteration directions between f and $\{v_m\}_{m=1}^N$ is the well-known alternating minimization method (**beck2015convergence**). Specifically, for a fixed f, minimizing Eq. (3.2.4) with v_m is identical to minimizing the following cost functional $V_m[v;\chi]$, which is part of the fidelity term in the functional $J[\chi, v_1, \cdots, v_N, \gamma]$:

$$
\begin{aligned}
V_m[v;\chi] := &\|\chi G^D v - v + \chi p_m^{\mathrm{inc}}\|_{L^2(D)}^2 \\
&+ \frac{\mu_D[\chi]}{\mu_S}\|G^S v - g_m\|_{L^2(S)}^2 .
\end{aligned} \tag{3.3.1}
$$

Then, after updating the regularization parameter γ by the method described in Sect. 3.3.3, for fixed $\{v_m\}_{m=1}^N$, we give the minimum χ by minimizing the following cost functional $F[\chi; v_1, \cdots, v_N, \gamma]$:

$$
F[\chi; v_1, \cdots, v_N, \gamma] := J[\chi, v_1, \cdots, v_N, \gamma]. \tag{3.3.2}
$$

We summarize the alternating minimization method for the robust CSI method (see algorithm 1). The numerical implementation of steps 2 and 4 are shown in Sect. 3.3.2. Later, we will discuss step 3 in detail in Sect. 3.3.3, with regard to the automatic choice rule of regularization parameters.

Algorithm 1: Alternating minimization method with automatic choice rule – outer iteration

```
  Input: $\chi^{(0)}$, $\{v_m^{(0)}\}_{m=1}^N$, and $\gamma^{(0)}$.
1 for $k = 0, 1, \cdots$ do
2     $v_m^{(k+1)} = \arg\min_v V_m[v;\chi^{(k)}]$ for $m = 1, \cdots, N$;
3     Update $\gamma^{(k+1)}$ automatically from $\gamma^{(k)}$ by using algorithm 4;
4     Compute
          $$\chi^{(k+1)} = \arg\min_{\chi} F[\chi; v_1^{(k+1)}, \cdots, v_N^{(k+1)}, \gamma^{(k+1)}].$$
5 end
```

Since the zero-valued initial guesses lead to the vanishing of the second term in Eq. (3.3.1) owing to zeroing $\mu_D[\chi]$ in Eq. (3.2.5), one should design the initial guesses of $\chi^{(0)}$ and $\{v_m^{(0)}\}_{m=1}^N$. On the basis of the idea presented in

van1997contrast, the available initial guess can be chosen as the backpropagation solution

$$v_m^{(0)} = \frac{\|G^{S*}g_m\|^2_{L^2(D)}}{\|G^S G^{S*}g_m\|^2_{L^2(D)}} G^{S*}g_m, \tag{3.3.3}$$

where $m = 1, 2, \cdots, N$. Then, substituting v_m with $v_m^{(0)}$ and minimizing the first term in Eq. (3.2.4) yields the expression of $\chi^{(0)}$:

$$\chi^{(0)} = \frac{\sum_{m=1}^N \overline{p_m^{(0)}} v_m^{(0)}}{\sum_{m=1}^N |p_m^{(0)}|^2}, \tag{3.3.4}$$

with $p_m^{(0)} = p_m^{\text{inc}} + G^D v_m^{(0)}$, for $m = 1, \cdots, N$.

3.3.2 Inner iteration

The inner iterations in algorithm 1, i.e., steps 2 and 4, are directly given by some general numerical methods. Specifically, $v_m^{(k+1)}$ can be updated by the conjugate gradient method (**saad2003iterative**) and $f^{(k+1)}$ by the lagged diffusivity method (**vogel1996iterative**) for TV regularization of image denoising (see algorithms 2 and 3 in Appendix**??**). We restrict the maximal step $j^{\max}$ for both algorithms considering the efficiency of all the algorithms instead of complete convergence. Actually, in the original CSI method, $j^{\max}$ is recommended to be chosen as 1 (**van1997contrast**).

In this appendix, we give the concrete forms of the conjugate gradient method in algorithm 2 and the lagged diffusivity method in algorithm 3. Note that for algorithm 2, the step size $\beta_m^{(k,j+1)}$ of the conjugate vectors can be calculated by either the Fletcher-Reeves formula or the Polak-Ribiere formula. Choosing the appropriate formula will speed up the inner iteration. For algorithm 3, first and foremost, the second term of Eq. (3.2.4) will not be included in the iteration scheme, because the coefficient is sufficiently small to be neglected owing to the assumption in Sect. 2. Second, the lagged diffusivity method also holds in the case of the diagonal operator.

3.3.3 Automatic choice rule of regularization parameters

In this section, we will review the automatic choice rule of regularization parameters, originally proposed in **clason2010semismooth**, for the alternating minimization method above. We first briefly describe a fixed point algorithm

Algorithm 2: Conjugate gradient method – $v_m^{(k+1)} = \arg\min_v V_m[v;\chi^{(k)}]$.

Input: $\chi^{(k)}$, $j^{\max}$, $v_m^{(k,0)} := v_m^{(k)}$, $w_m^{(k,1)} := w_m^{(k)}$, and $h_m^{(k,1)} := h_m^{(k)}$.
Output: $v_m^{(k+1)} := v_m^{(k,j^{\max})}$, $w_m^{(k+1)} := v_m^{(k,j^{\max}+1)}$, and $h_m^{(k+1)} := v_m^{(k,j^{\max}+1)}$.

```
for $j = 1, 2, \cdots, j^{\max}$ do
    $v_m^{(k,j)} := v_m^{(k,j-1)} + \alpha_m^{(k,j)} w_m^{(k,j)}$ where
      $\alpha_m^{(k,j)} = \arg\min_\alpha V_m[v_m^{(k,j-1)} + \alpha w_m^{(k,j)}; \chi^{(k)}]$;
    $p_m^{(k,j)} := p_m^{\mathrm{inc}} + G^D v_m^{(k,j)}$;
    Residual: $\rho_m^{(k,j)} = g_m - G^S v_m^{(k,j)}$, $r_m^{(k,j)} = \chi^{(k)} p_m^{(k,j)} - v_m^{(k,j)}$;
    Gradient: $h_m^{(k,j+1)} := -\frac{\mu_D[\chi^{(k)}]}{\mu_S} G^{S^*} \rho_m^{(k,j)} - (r_m^{(k,j)} - G^{D^*}(\overline{\chi^{(k)}} r_m^{(k,j)}))$
      where $\mu_S = \sum_{i=1}^N \|g_i\|_{L^2(S)}^2$,   $\mu_D[\chi^{(k)}] = \sum_{i=1}^N \|\chi^{(k)} p_i^{\mathrm{inc}}\|_{L^2(D)}^2$;
    $w_m^{(k,j+1)} := h_m^{(k,j+1)} + \beta_m^{(k,j+1)} w_m^{(k,j)}$ where $\beta_m^{(k,j+1)} =$
      $\begin{cases} \|h_m^{(k,j+1)}\|_{L^2(D)}^2 / \|h_m^{(k,j)}\|_{L^2(D)}^2 & \text{Fletcher-Reeves} \\ \langle h_m^{(k,j+1)}, h_m^{(k,j+1)} - h_m^{(k,j)} \rangle_{L^2(D)} / \|h_m^{(k,j)}\|_{L^2(D)}^2 & \text{Polak-Ribiere} \end{cases}$;
end
```

The initial values are $w_m^{(0)}$ and $h_m^{(0)}$. We choose $w_m^{(0)} = h_m^{(0)}$ first. Then $h_m^{(0)}$ is determined by the expression $h_m^{(0)} := -\frac{\mu_D[\chi^{(0)}]}{\mu_S} G^{S^*} \rho_m^{(0)} - (r_m^{(0)} - G^{D^*}(\overline{\chi^{(0)}} r_m^{(0)}))$ where $\rho_m^{(0)} = g_m - G^S v_m^{(0)}$ and $r_m^{(0)} = \chi^{(0)} p_m^{(0)} - v_m^{(0)}$ with the initial guesses of Eqs. (3.3.3) and (3.3.4).

for resolving regularization parameters. This algorithm is based on the balancing principle and the model function approach. Throughout this section, we only concentrate on the special case where $\{v_m\}_{m=1}^N$ is fixed.

Balancing principle and model function approach

The idea of the balancing principle is to balance the data fidelity term $\sum_{m=1}^N V_m[v_m, \chi]$ and the penalty term $\gamma \|\nabla\chi\|_{L^1(D)}$ of the cost functional denoted by $F(\gamma) := \min_\chi F[\chi; v_1, \cdots, v_N, \gamma]$. From Eq. (3.4.8) in Appendix3.4, we note that $F'(\gamma) = \|\nabla\chi\|_{L^1(D)}$, i.e., the penalty term. Hence, the optimal regularization parameter $\gamma^\dagger$ should satisfy

$$F(\gamma^\dagger) = \sigma(F(\gamma^\dagger) - \gamma^\dagger F'(\gamma^\dagger)), \tag{3.3.5}$$

where $\sigma > 1$ is a weight slightly larger than 1 for balancing the two sides of the equation. It follows from the idea of fixed point iteration that the regularization parameter $\gamma^{(k+1)}$ is updated by

$$F(\gamma^{(k+1)}) = \sigma(F(\gamma^{(k)}) - \gamma^{(k)} F'(\gamma^{(k)})). \tag{3.3.6}$$

```
Algorithm 3: Lagged diffusivity method
    $\chi^{(k+1)} = \arg\min_{\chi} F[\chi; v_1^{(k+1)}, \cdots, v_N^{(k+1)}, \gamma^{(k+1)}]$
Input: $\chi^{(k,0)} := \chi^{(k)}, \chi^{(k,-1)} := \chi^{(k-1)}$ ($\chi^{(0)}$ if $k = 0$), $\{v_m^{(k+1)}\}_{m=1}^{N}, \gamma^{(k+1)}$,
       and $j^{\max}$.
Output: $\chi^{(k+1)} := \chi^{(k,j^{\max})}$ and $\chi^{(k)} := \chi^{(k,j^{\max}-1)}$.
$p_m^{(k+1)} = G^D v_m^{(k+1)} + p_m^{\mathrm{inc}}$ for all $m = 1, \cdots, N$;
Shrinking coefficient $t = 1/\sum_{m=1}^{N} \|p_m^{(k+1)}\|_{L^\infty(D)}^2$;
for $j = 1, 2, \cdots, j^{\max}$ do
    The factor $\delta^{(k,j-1)} = \sum_{m=1}^{N} \|\chi^{(k,j-1)} p_m^{(k+1)} - v_m^{(k+1)}\|_{L^2(D)}^2$;
    $\chi^{(k,j+1)} = \chi^{(k,j)} - t\left(\sum_{m=1}^{N} \overline{p_m^{(k+1)}}(\chi^{(k,j)} p_m^{(k+1)} - v_m^{(k+1)}) - \gamma^{(k+1)} \nabla \cdot \frac{\nabla \chi^{(k,j)}}{\sqrt{|\nabla \chi^{(k,j-1)}|^2 + \delta^{(k,j-1)}}}\right)$.
end
```

To rapidly compute it, we use the model function approach proposed in **kunisch1998iterative** by approximating $F(\gamma)$ with the rational polynomials $m(\gamma)$, i.e.,

$$m(\gamma) = a + \frac{b}{c + \gamma}. \tag{3.3.7}$$

Noting $F(\gamma) \to \sum_{m=1}^{N} \|v_m\|_{L^2(D)}^2$ as $\gamma \to \infty$ [see Eq. (3.4.4) in the proof of Lemma3.4.1], we choose $a = \sigma \sum_{m=1}^{N} \|v_m\|_{L^2(D)}^2$ to ensure that $m(\gamma)$ mimics the asymptotic behavior of $F(\gamma)$. One can determine the coefficients b and c from the model functions $m(\gamma)$ and $m'(\gamma)$, i.e.,

$$a + \frac{b}{c + \gamma} = m(\gamma) \approx F(\gamma), \tag{3.3.8}$$

$$-\frac{b}{(c + \gamma)^2} = m'(\gamma) \approx F'(\gamma). \tag{3.3.9}$$

After obtaining all the coefficients in $m(\gamma)$, we write the expression of the new regularization parameter $\gamma^{(\mathrm{new})}$ updated from γ by combining the interpolation relation $F(\gamma^{(\mathrm{new})}) \approx m(\gamma^{(\mathrm{new})})$, and Eqs. (3.3.6) and (3.3.7):

$$\gamma^{(\mathrm{new})} = \frac{b}{\sigma(F(\gamma) - \gamma F'(\gamma)) - a} - c. \tag{3.3.10}$$

Finally, with the recursion scheme (3.3.10), we give the complete algorithm of the automatic choice rule of regularization parameters (see algorithm 4).

Algorithm 4: Automatic choice rule of regularization parameters

```
    Input: $\chi^{(k)}, \{v_m^{(k+1)}\}_{m=1}^N$, and $\gamma^{(k)}$.
    Output: $\gamma^{(k+1)}$.
Compute $F(\gamma^{(k)}) := F[\chi^{(k)}; v_1^{(k+1)}, \cdots, v_N^{(k+1)}, \gamma^{(k)}]$ and
  $F'(\gamma^{(k)}) := F'[\chi^{(k)}; v_1^{(k+1)}, \cdots, v_N^{(k+1)}, \gamma^{(k)}]$;
Compute the coefficients of the model function $m(\gamma)$ as follows
    $a^{(k)} = \sigma \sum_{m=1}^{N} \|v_m^{(k+1)}\|_{L^2(D)}^2;$
    $b^{(k)} = -\frac{(a^{(k)} - F(\gamma^{(k)}))^2}{F'(\gamma^{(k)})};$
    $c^{(k)} = \frac{a^{(k)} - F(\gamma^{(k)})}{F'(\gamma^{(k)})} - \gamma^{(k)}.$
Compute $\gamma^{(k+1)} = \frac{b^{(k)}}{\sigma(F(\gamma^{(k)}) - \gamma^{(k)} F'(\gamma^{(k)})) - a^{(k)}} - c^{(k)}$.
```

Selection of initial guess $\gamma^{(0)}$

Algorithm 4 provides a way to search for the optimal regularization parameter along the sequence $\{\gamma^{(k)}\}_{k\in\mathbb{N}}$ while iterating on the outer algorithm 1. In this section, we will show how the initial guess of the regularization parameter $\gamma^{(0)}$ significantly affects the convergence of algorithm 4. The succinct notation $R(\gamma) = (1-\sigma)F(\gamma) + \sigma\gamma F'(\gamma)$ denotes the residual of the balancing equation (3.3.5). Lemma3.4.4 in Appendix3.4 shows that this sequence $\{\gamma^{(k)}\}_{k\in\mathbb{N}}$ converges if we prudently select the initial guess $\gamma^{(0)}$ such that the residual of the balancing equation (3.3.5) satisfies $R(\gamma^{(0)}) > 0$.

We discuss the simplest case of the relationship between the regularization parameter γ and the residual $R(\gamma)$ of the balancing equation in Fig. 3.2. Assume the inequality (3.4.5) holds strictly, i.e., $\lim_{\gamma\to+\infty} R(\gamma) < 0$, and from Eqs. (3.4.6) and (3.4.7), the limit $R(0+)$ is negative and there exists $\gamma_0 \in (0, +\infty)$ such that $R(\gamma_0) > 0$. Then there must be two roots, $\gamma^{\dagger,1}$ and $\gamma^{\dagger,2}$, of the balancing equation $R(\gamma) = 0$ located at intervals $(0, \gamma_0)$ and $(\gamma_0, +\infty)$, respectively. From Lemma3.4.4, the sequence $\{\gamma^{(k)}\}_{k\in\mathbb{N}}$ recursively generated by algorithm 4 converges to the accumulation point $\gamma^{\dagger,1}$, with the initial guess $\gamma^{(0)}$ chosen at the interval $(0, \gamma^{\dagger,2})$; otherwise, the sequence $\{\gamma^{(k)}\}_{k\in\mathbb{N}}$ diverges to infinity. Moreover, it is better to select a larger $\gamma^{(0)}$, which lies in $(\gamma^{\dagger,1}, \gamma^{\dagger,2})$, in order to make the penalty term $\gamma\|\nabla\chi\|_{L^1(D)}$ in Eq. (3.2.4) effective.

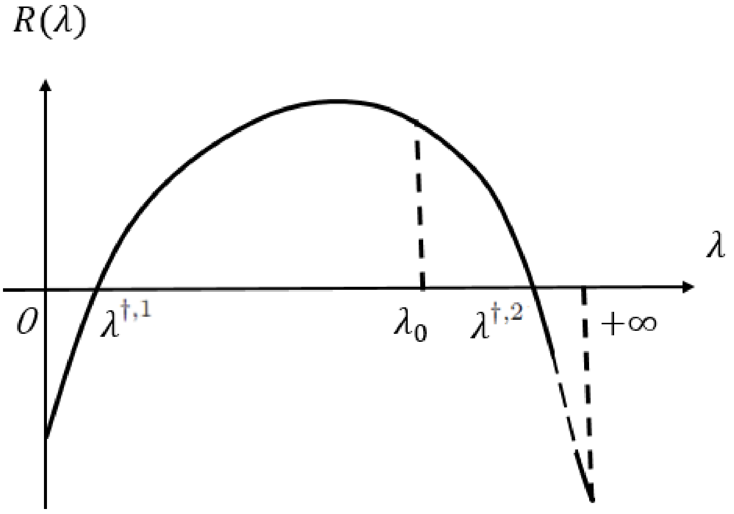

FIGURE 3.2: (Color online) Simplest case of the residual $R(\gamma)$ of the balancing equation.

3.3.4 Global convergence

We first discuss the convexity of the cost functional J in Eq. (3.2.4) in order to ensure the global convergence of algorithm 1. The cost functional J is a polynomial of degree 4 with respect to the unknowns, which indicates that there probably exists one or two local minima. **van2001contrast** and the references therein suggest that the large number of sources N may prevent algorithm 1 from being trapped in the false local minimum. It implies that the functional J is locally convex under a prescribed initialization.

As our main contribution, we write the compound convergence result of the alternating minimization method with the automatic choice rule, which has been studied in **clason2010semismooth** and **beck2015convergence**. For simplicity, we give a complete notation of the residual of the balancing equation $R[\gamma; z] = (1-\sigma)J[z, \gamma] - \sigma\gamma\|\nabla\chi\|_{L^1(D)}$ with $z = (\chi, v_1, \cdots, v_N)$. We denote by $z^{(k+1/2)} = (\chi^{(k)}, v_1^{(k+1)}, \cdots, v_N^{(k+1)})$ "a sequence in between" generated by step 2 in algorithm 1 after the kth iteration $z^{(k)} = (\chi^{(k)}, v_1^{(k)}, \cdots, v_N^{(k)})$ in step 4. To keep the consistency of the notation, $\gamma^{(k+1/2)}$ denotes the regularization parameter updated at step 3 of the kth iteration and transmits an identical value to $\gamma^{(k+1)}$ at step 4.

Theorem 3.3.1. *Assume the number of sources N is sufficiently large. Let $\{z^{(k/2)}\}_{k\in\mathbb{N}}$ be the function sequence and $\{\gamma^{(k/2)}\}_{k\in\mathbb{N}}$ the regularization-parameter sequence, both generated using algorithm 1 with an initial regularization parameter $\gamma^{(0)}$ satisfying $R[\gamma^{(0)}; z^{(0)}] > 0$. Then $\{z^{(k/2)}\}_{k\in\mathbb{N}}$ globally converges to the optimum $z^{\dagger}$ of* *the problem (3.2.4), and* $\{\gamma^{(k/2)}\}_{k\in\mathbb{N}}$ *converges to* $\gamma^\dagger$*, one of the roots of the balancing equation, which satisfies* $R(\gamma^\dagger; z^\dagger) = 0$*.*

The proof of Theorem 3.3.1 is shown in next section. With the help of the proximal-gradient theories, the sequence $\{J[z^{(k/2)}, \gamma^{(k/2)}]\}_{k\in\mathbb{N}}$ monotonically decreases and converges at a sublinear convergence rate $O(1/k)$ (**beck2015convergence**).

3.4 Proof of Theorem 3.3.1

Here, we list all the required results from which the convergence theorem of algorithm 1 are derived. First, we write some notations. Let $\chi(\gamma)$ denote the minimum of the functional $F[\chi; v_1, \cdots, v_N, \gamma]$ in Eq. (3.3.2) with respect to the positive constant γ. We assume $\{v_m\}_{m=1}^N$ is fixed in Lemma3.4.1-3.4.4.

The following lemma shows that the balancing equation is soluble with a fixed $\{v_m\}_{m=1}^N$.

Lemma 3.4.1 (Similar to Theorem 4.1 in **clason2010semismooth**)**.** *For* $\sigma > 1$ *sufficiently close to* 1 *and a large* $\sum_{m=1}^N \|v_m\|^2_{L^2(D)}$*, the balancing equation* $R(\gamma) = 0$ *has at least one positive solution.*

Proof. Firstly, from the definition of $f(\gamma)$, we have $F[\chi(\gamma); v_1, \cdots, v_N, \gamma] \leq F[\chi; v_1, \cdots, v_N, \gamma]$ for any $\chi \in L^2(D)$. Take $\chi = 0$ and then we have

$$\begin{aligned} &C\gamma\|\chi(\gamma)\|_{L^2(D)} \leq \gamma\|\nabla\chi(\gamma)\|_{L^1(D)} \\ \leq &F[\chi(\gamma); v_1, \cdots, v_N, \gamma] \leq \sum_{m=1}^N \|v_m\|^2_{L^2(D)}, \end{aligned} \tag{3.4.1}$$

where the Gagliardo-Nirenberg-Sobolev inequality (**adam2003sobolev**) is employed in the first inequality since χ has the compact support in D and C is a constant greater than zero. Dividing the inequalities (3.4.1) with γ on both sides and letting it go to infinity, we obtain

$$\lim_{\gamma\to\infty} \|\chi(\gamma)\|_{L^2(D)} = 0. \tag{3.4.2}$$

Moreover, following the same deduction of Lemma 4.2 in **clason2010semismooth**, it holds that

$$\lim_{\gamma\to 0^+} \gamma\|\nabla\chi(\gamma)\|_{L^1(D)} = \lim_{\gamma\to\infty} \gamma\|\nabla\chi(\gamma)\|_{L^1(D)} = 0. \tag{3.4.3}$$

With Eqs. (3.4.2) and (3.4.3) and the triangle inequality, we have

$$\lim_{\gamma\to\infty} F(\gamma) = \sum_{m=1}^{N} \|v_m\|_{L^2(D)}^2. \tag{3.4.4}$$

With Eqs. (3.4.3) and (3.4.4), the limits of the residual $R(\gamma)$ defined in Sect. 3.3.3 have the properties

$$\begin{aligned}\lim_{\gamma\to+\infty} R(\gamma) = (1-\sigma)\sum_{m=1}^{N} \lim_{\gamma\to+\infty} \|\chi(\gamma)G^D v_m \\ - v_m + \chi(\gamma)p_m^{\text{inc}}\|_{L^2(D)}^2 \le 0, \qquad (3.4.5)\\ \lim_{\gamma\to0^+} R(\gamma) = (1-\sigma)\sum_{m=1}^{N} \|v_m\|_{L^2(D)}^2 < 0. \qquad (3.4.6)\end{aligned}$$

Note that

$$\|\chi(\gamma)G^D v_m - v_m + \chi(\gamma)p_m^{\text{inc}}\|_{L^2(D)}^2 \le \|v_m\|_{L^2(D)}^2,$$

and $0 < \gamma_0 < +\infty$ such that $\gamma_0\|\nabla\chi(\gamma_0)\|_{L^1(D)} > 0$. Therefore, one can find a $\sigma_0 > 1$ such that for any $\sigma \in (1, \sigma_0)$,

$$R(\gamma_0) \ge \lim_{\gamma\to0^+} R(\gamma) + \gamma_0\|\nabla\chi(\gamma_0)\|_{L^1(D)} > 0. \tag{3.4.7}$$

With the continuity of $R(\gamma)$, this proves the lemma. □

Then we show the significant properties of the functional $F(\gamma)$ defined in Sect. 3.3.3.

Lemma 3.4.2. *The first-order derivative of $F(\gamma)$ on γ is of the form*

$$F'(\gamma) = \|\nabla\chi(\gamma)\|_{L^1(D)}. \tag{3.4.8}$$

Proof. With the chain rule, the derivative of $F(\gamma)$ is immediately given by

$$\begin{aligned}F'(\gamma) = \left.\frac{\partial F[\chi; v_1, \cdots, v_N, \gamma]}{\partial\chi}\right|_{\chi=\chi(\gamma)} f'(\gamma) \\ + \|\nabla\chi\gamma)\|_{L^1(D)}. \qquad (3.4.9)\end{aligned}$$

Note that $\frac{\partial F[f;v_1,\cdots,v_N,\gamma]}{\partial f}$ is the Frechet derivative of $F[f; v_1, \cdots, v_N, \gamma]$ vanishing on the optimal solution $f(\gamma)$. Then the remaining part of Eq. (3.4.9) gives Eq. (3.4.8). □

Lemma 3.4.3. *Let $0 < \alpha < \beta$. Then $F(\alpha) \le F(\beta)$ but $F'(\alpha) \ge F'(\beta)$.*

Proof. From the definitions of $\chi(\alpha)$ and $\chi(\beta)$, we have

$$\begin{aligned} F[\chi(\alpha); v_1, \cdots, v_N, \gamma] &\leq F[\chi(\beta); v_1, \cdots, v_N, \gamma], \\ F[\chi(\beta); v_1, \cdots, v_N, \beta] &\leq F[\chi(\gamma); v_1, \cdots, v_N, \beta]. \end{aligned}$$

Adding the two inequalities, rearranging the terms, and applying Lemma3.4.2, we obtain

$$(\alpha - \beta)(F'(\alpha) - F'(\beta)) \leq 0.$$

Moreover, since $F'(\alpha) \geq 0$ for any $\alpha > 0$, another inequality is attained by the monotonicity property, i.e., $F(\alpha) \leq F(\beta)$. ☐

So far it is enough to state that for any given χ, $\{v_m\}_{m=1}^N$, and an initial guess $\gamma^{(0)}$ satisfying $R(\gamma^{(0)}) > 0$, the regularization-parameter sequence $\{\gamma^{(k)}\}_{k\in\mathbb{N}}$ generated by algorithm 4 recursively is monotonically decreasing.

Lemma 3.4.4. *Let $\gamma^{(\mathrm{new})}$ updated by algorithm 4 [or Eq. (3.3.10)] be the next regularization parameter of the positive γ. Then, if γ satisfies $R(\gamma) > 0$, it holds that $0 < \gamma^{(\mathrm{new})} < \gamma$ and $R(\gamma^{(\mathrm{new})}) > 0$; in contrast, if $R(\gamma) < 0$, it holds that $\gamma^{(\mathrm{new})} > \gamma$.*

Proof. From Eqs. (3.3.8)-(3.3.10), we have

$$\begin{aligned} \gamma^{(\mathrm{new})} - \gamma &= -\frac{a - F(\gamma)}{a - \sigma(F(\gamma) - \gamma F'(\gamma))} \frac{R(\gamma)}{F'(\gamma)} \\ &:= \omega(\gamma) \frac{R(\gamma)}{F'(\gamma)}. \end{aligned} \tag{3.4.10}$$

Having deduced the inequality (3.4.1) in Lemma3.4.1, i.e.,

$$\begin{aligned} F(\gamma) &\leq \sum_{m=1}^{N} \|v_m\|^2_{L^2(D)}, \\ F(\gamma) - \gamma F'(\gamma) &\leq \sum_{m=1}^{N} \|v_m\|^2_{L^2(D)}, \end{aligned}$$

and with $a = \sigma \sum_{m=1}^N \|v_m\|^2_{L^2(D)}$, we have $\omega(\gamma) < 0$. Hence, $(\gamma^{(\mathrm{new})} - \gamma)$ has the opposite sign against $R(\gamma)$. Moreover, in the case of $R(\gamma) > 0$, we note that $-1 < \omega(\gamma) < 0$ directly from the definition in Eq. (3.4.10). It follows from

Lemma3.4.3, $\sigma > 1$, and Eq. (3.4.10) that

$$\begin{aligned}\frac{R(\gamma^{(\text{new})})}{F'(\gamma^{(\text{new})})} &= (1-\sigma)\frac{F(\gamma^{(\text{new})}) - \gamma^{(\text{new})}F'(\gamma^{(\text{new})})}{F'(\gamma^{(\text{new})})} + \gamma^{(\text{new})} \\ &\geq (1-\sigma)\frac{F(\gamma) - \gamma F'(\gamma)}{F'(\gamma)} + \gamma^{(\text{new})} \\ &= (1+\omega(\gamma))\frac{R(\gamma)}{F'(\gamma)},\end{aligned}$$

which proves $R(\gamma^{(\text{new})}) > 0$. Finally, note that from Eq. (3.4.10),

$$\gamma^{(\text{new})} = \omega(\gamma)(1-\sigma)\frac{F(\gamma) - \gamma F'(\gamma)}{F'(\gamma)} + (1+\omega(\gamma))\gamma.$$

This yields $\gamma^{(\text{new})} > 0$ since the data fidelity term $F(\gamma) - \gamma F'(\gamma)$ is always positive. ☐

Note that Lemma3.4.4 indicates

$$J[z^{(k+1/2)}, \gamma^{(k)}] \geq J[z^{(k+1/2)}, \gamma^{(k+1/2)}],$$

for $k = 0, 1, \cdots$ with an initial guess $\gamma^{(0)}$ satisfying $R[\gamma^{(0)}; z^{(1/2)}] > 0$. This implies the sequence $\{J[z^{(k/2)}, \gamma^{(k/2)}]\}_{k\in\mathbb{N}}$ is monotonically decreasing.

With the notations $R[\gamma; z]$ shown in Sect. 3.3.4, we quote the convergence of the regularization parameter from the recursive execution of the automatic choice rule as follows (**clason2010semismooth**).

Lemma 3.4.5. *Assume there exists $\gamma^{(0)} > 0$ such that $R[\gamma^{(0)}; z^{(0)}] > 0$. Then the regularization-parameter sequence $\{\gamma^{(k/2)}\}_{k\in\mathbb{N}}$ generated by algorithm 1 is monotonically decreasing and bounded below, i.e., converged.*

Proof. First, that the sequence $\{J[z^{(k/2)}, \gamma^{(k/2)}]\}_{k\in\mathbb{N}}$ is monotonically decreasing stipulates $R[\gamma^{(k)}; z^{(k+1/2)}]>0$ if $R[\gamma^{(k)}; z^{(k)}] > 0$. It follows from Lemma3.4.4 that $R[\gamma^{(k+1)}; z^{(k+1)}] > 0$ if $R[\gamma^{(k)}; z^{(k+1/2)}] > 0$. Therefore, with Lemma3.4.4, the decreasing property of the sequence $\{\gamma^{(k/2)}\}_{k\in\mathbb{N}}$ with the lower bound of 0 is immediately valid. ☐

Before the proof of Theorem 3.3.1, we first introduce the concept of partial gradient mapping $H_f[z;\gamma]$ and $H_{v_m}[z;\gamma]$ with respect to f and v_m, for $m = 1, \cdots, N$, respectively (see **beck2015convergence** and the references therein). Since the cost function (3.2.4) is locally convex, when the number of sources N is sufficiently large, $z^\dagger$ is an optimal solution of Eq. (3.2.4) if and only if it satisfies $H_f[z^\dagger;\gamma] = 0$ and $H_{v_m}[z^\dagger;\gamma] = 0$ for a given γ and

$m = 1, \cdots, N$. Hence, this will result in the following consequence of the convergence analysis.

Proof of Theorem 3.3.1. This proof is a combination of Lemma 3.3 in **beck2015convergence** and Theorem 4.9 in **clason2010semismooth**, and proceeds in the following three steps.

1. From Lemma3.4.5, the sequence $\{\gamma^{(k/2)}\}_{k\in\mathbb{N}}$ decreasingly converges to a point $\gamma^\dagger$.
2. Since the integer-index sequence $\{z^{(k)}\}_{k\in\mathbb{N}}$ is bounded, there exists a subsequence $\{z^{(k_l)}\}_{l\in\mathbb{N}}$ that converges to an accumulation point $z^\dagger$. The integer-index sequence implies the partial gradient mapping w.r.t. f satisfies $H_f[z^{(k_l)}; \gamma^{(k_l)}] = 0$, which yields $H_f[z^\dagger; \gamma^\dagger] = 0$. On the other hand, noting that

$$\begin{aligned} 0 &\leq J[z^{(k)}, \gamma^{(k)}] - J[z^{(k+1/2)}, \gamma^{(k)}] \\ &\leq J[z^{(k)}, \gamma^{(k)}] - J[z^{(k+1/2)}, \gamma^{(k+1/2)}], \end{aligned}$$

   and that $\{J[z^{(k/2)}, \gamma^{(k/2)}]\}_{k\in\mathbb{N}}$ is nonincreasing and bounded below, we have $J[z^{(k)}, \gamma^{(k)}] - J[z^{(k+1/2)}, \gamma^{(k)}]$ converging to 0 as $k \to \infty$. Then from Lemma 3.1 of **beck2015convergence**, it follows that $H_{v_m}[z^{(k)}; \gamma^{(k)}] \to 0$ as $k \to \infty$. Hence, $H_{v_m}[z^\dagger; \gamma^\dagger] = 0$ by the continuity of H_{v_m} for $m = 1, \cdots, N$. Finally, we conclude that $z^\dagger$ is the optimum of Eq. (3.2.4) because $H_f[z^\dagger; \gamma^\dagger] = 0$ and $H_{v_m}[z^\dagger; \gamma^\dagger] = 0$ for $m = 1, \cdots, N$.
3. Substituting $\gamma^{(k)}$ and $\gamma^{(k+1)}$ with γ and $\gamma^{(\text{new})}$ in Eq. (3.4.10), respectively, and taking the limits on both sides, we immediately have $R[\gamma^\dagger; z^\dagger] = 0$.

□

3.5 Numerical results and discussion

In this section, we will numerically investigate the sound-speed distribution in order to illustrate the convergence and the robustness of our proposed method. A real medical phantom is extracted from a breast magnetic resonance image, as shown in Fig. 3.3(a). This heterogeneous image is to be regarded as the exact sound-speed distribution for the numerical simulation of wave-field data. With it, we generate the synthetic scattered-field boundary data $\{g_m(s)\}$ by applying the forward solver of the Lippmann-Schwinger equation in **chen2002fast**, and then add the 5% standard Gaussian noise to them. Using noise data, we run the robust CSI method with a fixed regularization parameter (RCSI), and with the automatic choice rule of regularization parameters (RCSI-ACR), starting with the initial guess of the contrast seen in Fig. 3.3(b). For all numerical results, we set the wavenumber $k = 1.039 \times 10^3\ \mathrm{rad/m}$, the wavelength 6.16 mm, and the sound speed of the homogeneous background $c_0 = 1540\ \mathrm{m/s}$. The rectangular domain D on a 256×256 grid is of a $100 \times 100\ \mathrm{mm}^2$ area. The 256 receivers and 128 sources are uniformly placed on the circle S with a 200 mm radius.

We start with the first example with a fixed regularization parameter $\gamma = 10^{-4}$ for RCSI, and with the automatic choice rule starting at $\gamma^{(0)} = 10^{-4}$ and choosing $\sigma = 1.01$ for RCSI-ACR. For both these methods, we choose one-maximal-step inner iteration. Table 3.1 shows that RCSI-ACR always has a smaller $L^2(D)$ relative error than RCSI at each outer iteration. Figures 3.3(a)-3.3(e) show the imaging quality under different methods when they terminates at sufficiently large outer iterates. Figures 3.3(c) and 3.3(d) indicate that RCSI-ACR reconstructs a sharper image than RCSI. This can also be seen in the horizontal cross sections of the position at -0.025 m shown in Figs. 3.4(a)-3.4(d) with different iterates. Moreover, the artifact, which is attributed to the noisy boundary data we generated in the synthetic wavefield data, degraded the image reconstructed by RCSI-ACR in Fig. 3.3(d), in comparison with the exact one in Fig. 3.3(a).

Currently, the numerical algorithm is implemented on a single core of the Intel Core i7-4790 central processing unit (CPU) of 3.60 GHz and 8 gigabytes memory using Matlab. Under this configuration, RCSI-ACR takes approximately $0.327 - 0.350$ h per outer iteration whereas RCSI takes approximately $0.307 - 0.338$ h per outer iteration (see Table 3.1). The additional computational cost of RCSI-ACR is caused by the automatic choice rule while iterating. However in fact, RCSI-ACR has been designed for parallel computing. We note that each source index m can be synchronously run in algorithm 2. Moreover, the computation of the operators G^S and G^D can be accelerated by the standard libraries of Parallel FFTW (fastest Fourier transform in the west (**fftw**)). As a result, the computational time will markedly decrease by at least a factor of 128 for our numerical example when the algorithm is run on a graphics processing unit (GPU).

In spite of the rather long wavelength of 6.16 mm we utilize, RCSI-ACR still produces a relatively high-resolution image compared with the ray-based reconstruction (**qu2015novel**) at a wavelength of 0.96 mm shown in Fig. 3.3(e). This is because the ray-based image is reconstructed from the first-arrival

TABLE 3.1: $L^2(D)$ relative error of the numerical solutions of the robust CSI methods with/without the automatic choice rule for some outer iterates, calculated using the synthetic data of 5% noise. RCSI: the robust CSI method with a fixed regularization parameter $\gamma = 10^{-4}$. RCSI-ACR: the robust CSI method with the automatic choice rule starting at $\gamma^{(0)} = 10^{-4}$.

	$L^2(D)$ relative error		Calculation time (h)	
Outer iterate	RCSI	RCSI-ACR	RCSI	RCSI-ACR
50	0.0152	0.0149	15.35	16.36
100	0.0137	0.0127	30.71	33.68
200	0.0128	0.0104	65.32	70.06
400	0.0125	0.0085	135.02	140.71

picking arising from the partial waveform data, whereas RCSI-ACR employs all single-frequency waveform data. Theoretically, the spatial resolution of the ray-based reconstruction related to the size of the Fresnel zone is rather lower than that of RCSI-ACR, one of the waveform inversion methods with "half-wavelength resolution"(**chen1997inverse**; **pratt2007soundspeed**). Numerically, the spatial resolution will be obtained from the signal-to-noise ratio (SNR) of the relative spectrum between the exact contrast $\chi^\dagger$ and the numerical one $\chi^{(k)}$, according to the expression

$$\mathrm{SNR} = 20\log_{10}\left|\frac{\widehat{\chi^{(k)}}}{\widehat{\chi^\dagger} - \widehat{\chi^{(k)}}}\right|,$$

for each spatial frequency at the kth outer iteration, where the hat symbol represents the discrete Fourier transform. In some sense, the CSI methods work as a spatially low-pass filter for the exact image. In Fig. 3.5, the brightest disk of the radius $340.3\ \mathrm{m}^{-1}$ is equivalent to approximately 48% of the wavelength of 6.16 mm. This indicates that the spatial resolution obtained by the robust CSI method is approximately half the wavelength in Figs. 3.5(a) and 3.5(b). Furthermore, with the automatic choice rule, the high-resolution noise is nearly eliminated since the spectrum far away from the original is almost dark [see Fig. 3.5(b)]. In terms of the diagnosis of breast cancer in practice, instead of the ray-based reconstruction, the RCSI-ACR method may be meaningful for detecting a Stage-I breast tumor with a size under 20 mm (**ajcc2002cancer**), because it yields a sound-speed image with a resolution of approximately 3 mm. The statistical data from National Cancer Center Hospital show that the ability to diagnose breast cancer at Stage I will significantly increase the survival rate to 98% in the long term(**nationalStatistic**).

Here, we note that, concerning a wavelength much shorter than 6.16 mm, our algorithm may significantly show a slow convergence. We claim that when one uses RCSI-ACR, there is a tradeoff between the computational cost per iteration and the terminal step. Consequently, the numerical solution of RCSI-ACR may be inaccurate as a result of the insufficient choice of point per wavelength (ppw) for the grids and the terminal step. In practice, we may also potentially face the situation where the experimental waveform data are largely attenuated after passing through the tissue, and correspondingly, a large error emerges for each iteration step. Therefore, for a shorter-wavelength case, the ray-based reconstruction may have the advantage of rapid convergence over the RCSI-ACR method. Nevertheless, the selection of such a long wavelength of 6.16 mm in our numerical computation is currently sufficient for validating the proposed RCSI-ACR algorithm. To ensure the accuracy firstly in our numerical example, we must deploy at least 16 ppw for the computational grids, with reference to the configuration in **ozmen2014ultrasound**.

The next example numerically shows the effect of the $j^{\max}$-maximal-step inner iteration for algorithms 2 and 3. Figure 3.6 shows how the L^2 relative measure of the error and the cost functional J in Eq. (3.2.4) vary as total number of inner iterates, which is equal to (outer iterates-1) $\times j^{\max}+$ current inner iterates, increases within different maximal steps $j^{\max}$. We see that the one-step inner iteration clearly has better performance in terms of convergence, as is recommended in **van1997contrast** and **van1999extended**. In fact, in terms of inner iteration, theoretically, the residual of the conjugate gradient method (algorithm 2) converges with finite steps, and that of the lagged diffusivity method (algorithm 3) converges with a linear rate. This causes the bottleneck of the whole computing cost to be attributable to the outer iteration with the sublinear rate of convergence. Hence, within a limited computing time, it is better to perform more outer iteration.

Note that the one-step inner iteration or the gradient-based iteration converges to a global minimizer in our example, even though the convergence at each step in algorithm 1 is not satisfied. According to the analysis of the gradient-based iteration in **van2001contrast**, this is because, in this example, we are fortunate enough to select the appropriate initial guess of the contrast source, which guarantees the local convexity of the cost functional J by taking the number of sources $N = 128$. Generally, more maximal inner iterates $j^{\max}$ are required to ensure that the global minimizer is successfully computed, which is in contrast to the above conclusion that the inner iteration needs to be reduced.

It is a surprise that the more inner iterates one executes, the slower the convergence becomes. This is because the $O(1/k)$ sublinear rate of convergence of outer iteration dominates the total convergence rate of algorithm 1. In future work, any numerical method that can speed up the outer iteration will be considered. In the near future, we will implement our algorithm on a GPU to show its good performance in parallel computing.

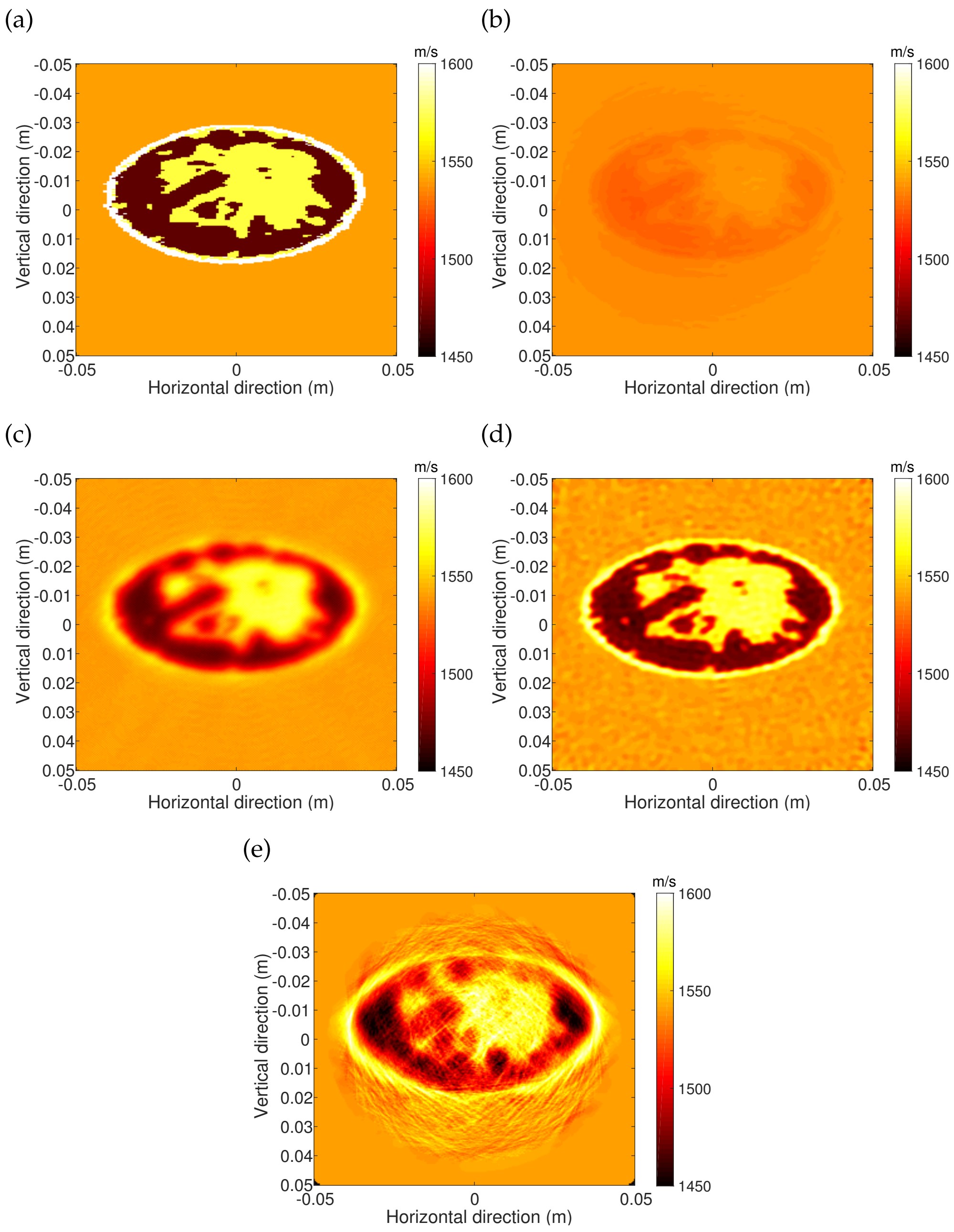

FIGURE 3.3: (Color online) Sound-speed distribution of the medical phantom using (a) exact phantom, (b) initial guess, (c) RCSI with 400 outer iterates, (d) RCSI-ACR with 400 outer iterates, and (e) ray-based reconstruction. The wavelength is 6.16 mm for (a)-(d) and 0.96 mm for (e).

(a)

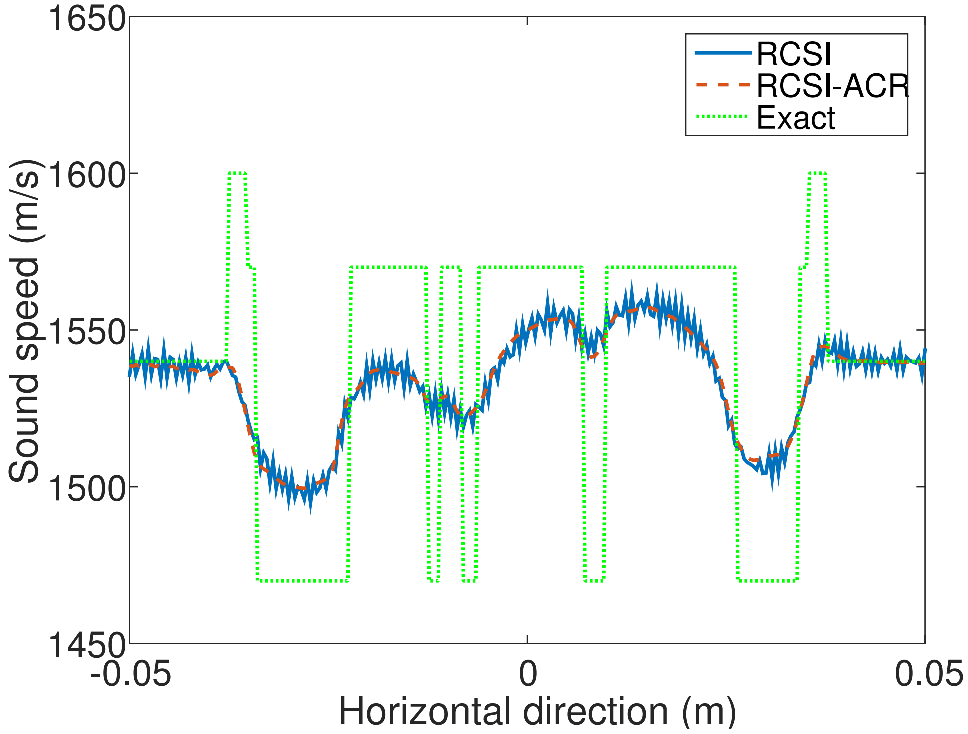

(b)

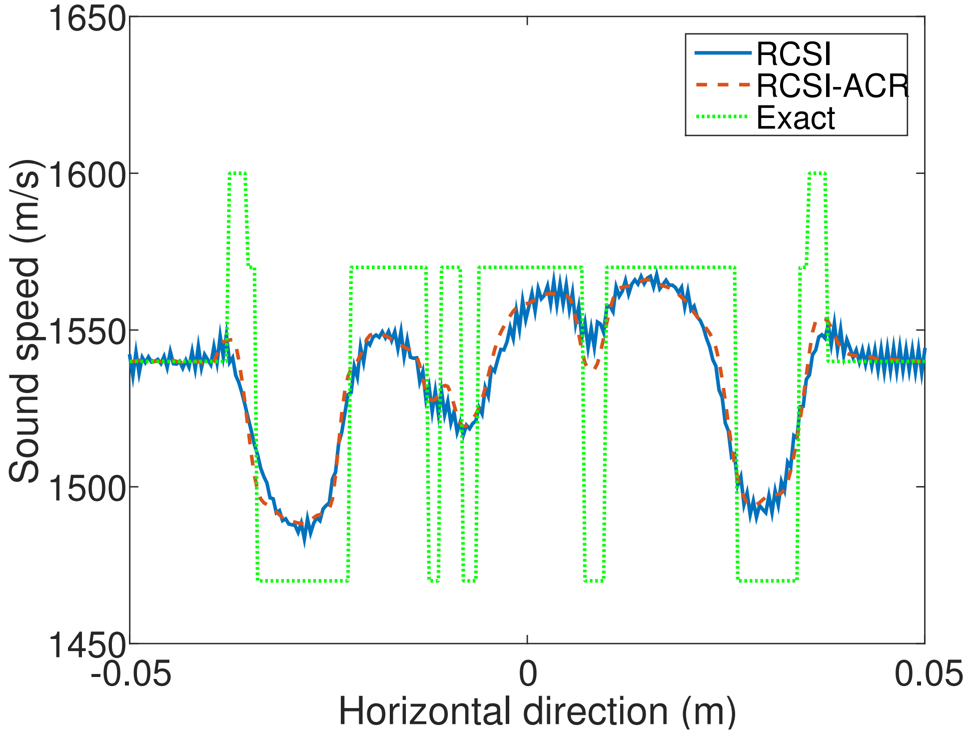

FIGURE 3.4: (Color online) Horizontal cross sections of the position at -0.025 m using the exact phantom, the RCSI, and RCSI-ACR with the different iterates: (a) 50 outer iterates, (b) 100 outer iterates, (c) 200 outer iterates, and (d) 400 outer iterates. The wavenumber is $k = 1.039 \times 10^3$ rad$/m$.

(c)

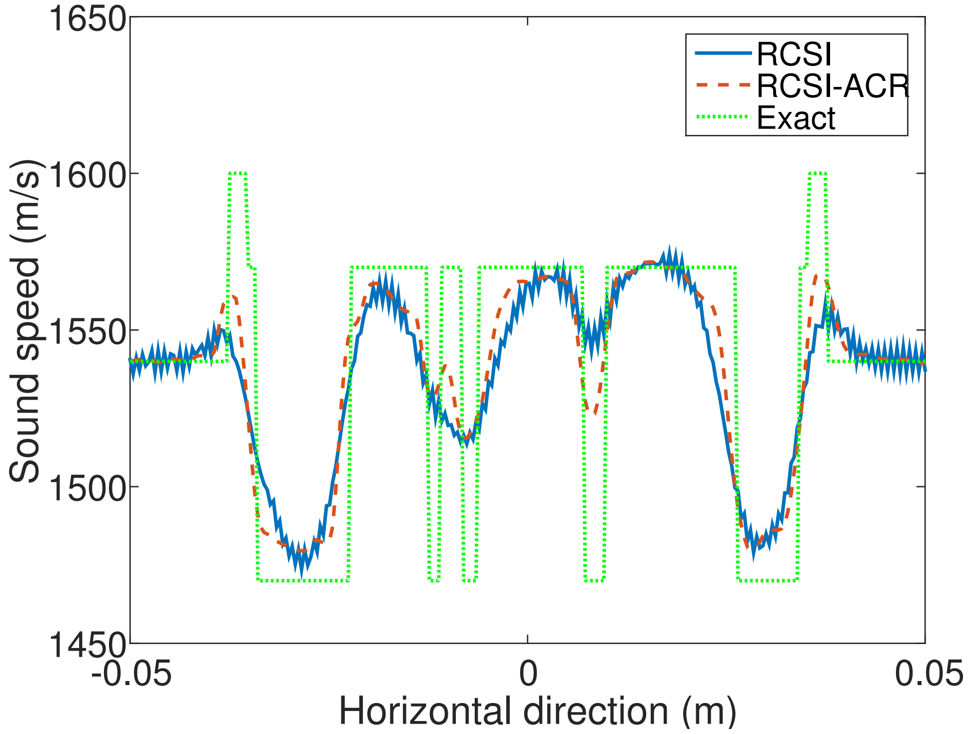

(d)

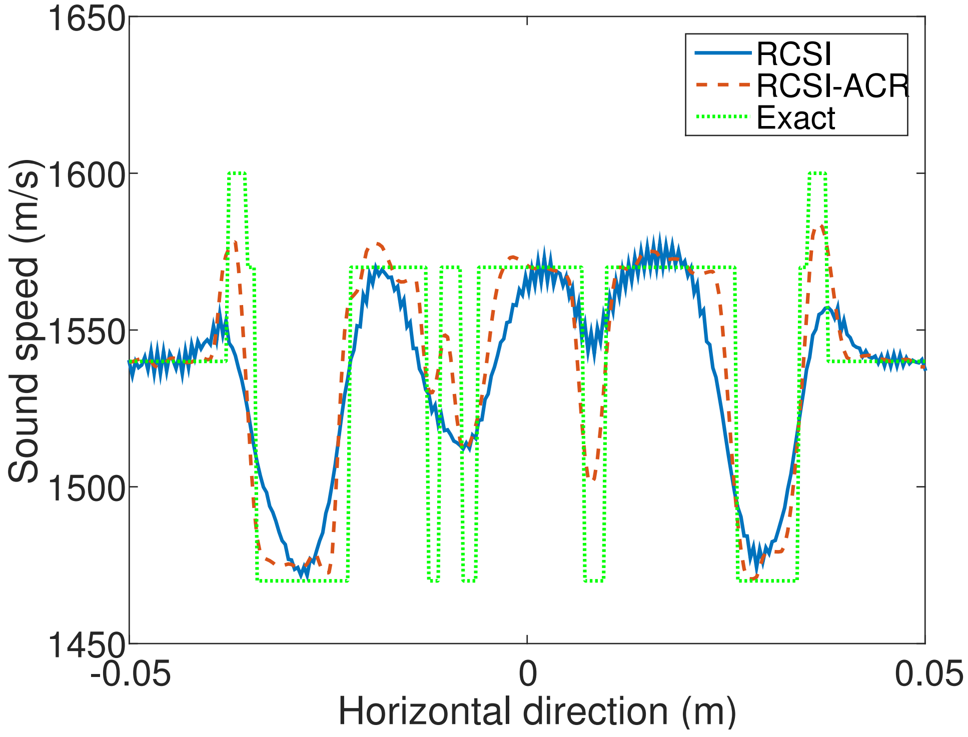

FIGURE 3.4: (Color online) Horizontal cross sections of the position at -0.025 m using the exact phantom, the RCSI, and RCSI-ACR with the different iterates: (a) 50 outer iterates, (b) 100 outer iterates, (c) 200 outer iterates, and (d) 400 outer iterates. The wavenumber is $k = 1.039 \times 10^3 \text{ rad}/m$.

(a)

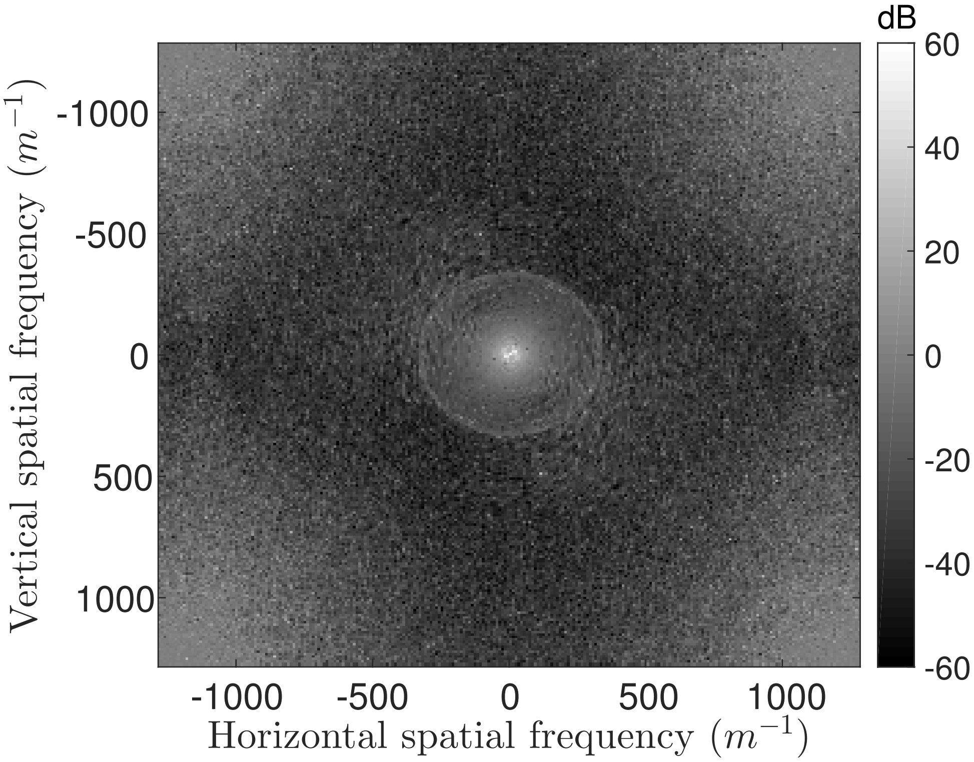

(b)

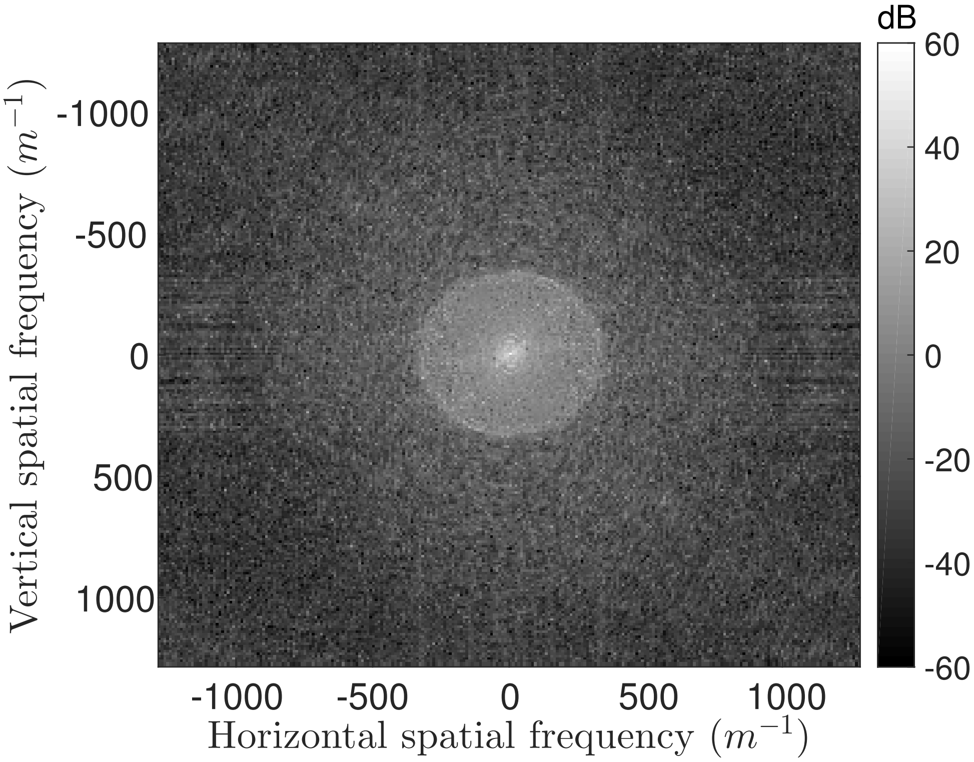

FIGURE 3.5: (Color online) Spectrum of numerical sound-speed distribution in Fig. 3.3(c) solved by (a) RCSI and in Fig. 3.3(d) solved by (b) RCSI-ACR, employing two-dimensional fast Fourier transform. The wavelength is 6.16 mm.

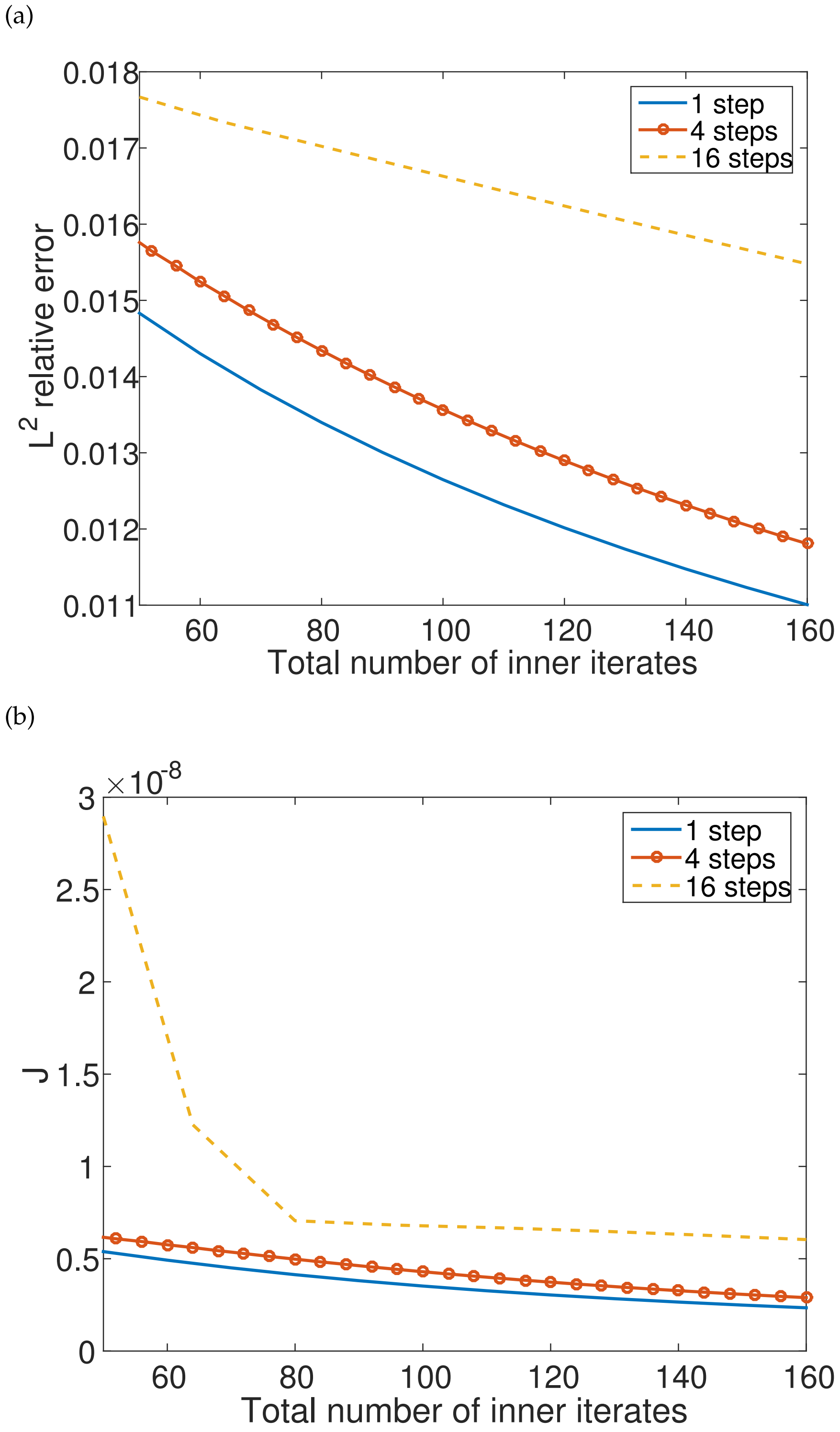

FIGURE 3.6: (Color online) L^2 relative measure of (a) the error and (b) the cost functional J at total number of inner iterates using one-step inner iteration, four-step inner iteration, and sixteen-step inner iteration. All methods start at the same regularization parameter 10^{-4}.

Chapter 4

Multi-frequency accelerating strategy

4.1 Introduction

Ultrasound computed tomography (USCT) is a prospective technology for breast cancer diagnosis providing three kinds of 3D images: speed of sound, attenuation, and reflection. In terms of the speed of sound image, the reconstruction modalities of USCT can roughly be classified into two categories: ray-based tomography and waveform tomography. For ray-based tomography, **Labyed2014** developed a two-parallel-transducer-array system and employed the ray-based method to reconstruct speed of sound. **Qu2015a**; **Qu2015b** reconstructs the speed-of-sound images on a ring transducer imaging system using Fermat's principle for ray tracing. On the other hand, waveform tomography, based on the wave equation retaining the integrated feature of acoustic wave, reconstructs high-resolution and accurate image (**Roy2010**; **Li2014**; **Wang2015**; **Sandhu2015**). **Duric2016** developed a commercial ultrasound tomography imaging system named SoftVue and demonstrated clinic significance of reconstructing the speed-of-sound images by waveform tomography. Compared with ray-based tomography, the images of the breast tissue reconstructed by waveform tomography have an advantage of higher resolution and accuracy. However, it is always time-consuming because of a large number of iterations as well as grid points. The contrast source inversion (CSI) method is a kind of inversion methods for ultrasound waveform tomography that does not require the forward solver through the reconstruction (**vandenBerg1997**). It is able to be calculated on a coarse grid because of the explicit introduction of the Green's function.(**Alles2011**; **Ying2015**) In the literature, there have existed various extensions for the CSI method, such as extended contrast source inversion(**vandenBerg1999**), robust contrast source inversion with automatic choice rule of regularization parameters (RCSI-ACR(**Lin2016**)), etc. **Ozmen-Eryilmaz** published the pioneer work on the inversion of speed of sound using the CSI method applied to low-frequency data, in terms of breast cancer detection.

The objective of this work is to implement the CSI method on the real configuration of breast cancer diagnostic device. We consider more practically that the pulse wave data collected by the time-domain simulator are applied. We attempt to make full use of the abundant frequency components from dataset while running the CSI method. Henceforth, we show a way to process the raw data for the CSI method and propose that the multi-frequency accelerating strategy significantly alleviates the computational cost as well as enhances the resolution of speed-of-sound reconstruction.

4.2 Method

The problem of ultrasound waveform tomography is formulated in a ring-array transducer on S in Fig. 4.1. The region of interest (ROI) is denoted by D. We start with the two-dimensional acoustical wave equation in the lossless media of the speed of sound $c(\mathbf{x})$, e.g. a breast phantom model in Fig. 4.2,

$$\nabla^2 P(\mathbf{x},t) - \frac{1}{c^2(\mathbf{x})}\frac{\partial^2 P(\mathbf{x},t)}{\partial t^2} = -Q(t)\delta(\mathbf{x}-\mathbf{s}), \tag{4.2.1}$$

Where $P(\mathbf{x},t)$ is the pressure field at the location x and the time t, and $Q(t)$ denotes a pulse excitation from a point-like source located at s. Doing Fourier transform for the both sides of Eq. (4.2.1) yields the Helmholtz equation in heterogeneous media

$$\nabla^2 p(\mathbf{x};\omega) + \frac{\omega^2}{c^2(\mathbf{x})} p(x;\omega) = -q(\omega)\delta(\mathbf{x}-\mathbf{s}), \tag{4.2.2}$$

where the total wave field $p(\mathbf{x};\omega)$ and the source modulation $q(\omega)$ with the angular frequency ω denote the Fourier transforms of the functions $P(\mathbf{x},t)$ and $Q(t)$, respectively. Let the incident wave field $p^{\mathrm{inc}}(\mathbf{x};\omega)$ be the solution of Eq. (4.2.2) with the uniform speed of sound c_0. We assume that the functions $p(\mathbf{x};\omega)$ and $p^{\mathrm{inc}}(\mathbf{x};\omega)$ have been normalized by the factor $q(\omega)$, or on the other way, let $q(\omega) = 1$. Then the Lippmann-Schwinger equation, which is an integral equation of Eq. (4.2.3), is derived as follows

$$p(\mathbf{x};\omega) - p^{\mathrm{inc}}(\mathbf{x};\omega) = \left(\frac{\omega}{c_0}\right)^2 \int_{\mathbb{R}^2} G(\mathbf{x},\mathbf{y};\omega)\chi(\mathbf{y})p(\mathbf{y};\omega)d\mathbf{y} := G^{\mathbf{x}\in\mathbb{R}^2}(\chi p), \tag{4.2.3}$$

where the contrast function is of the form $f(\mathbf{y}) = c_0^2/c^2(\mathbf{y}) - 1$ and the zero-order Hankel function of the first kind gives the free-space Green's function $G(\mathbf{x},\mathbf{y};\omega) = \frac{i}{4}H_0^{(1)}(\frac{\omega}{c_0}|\mathbf{x}-\mathbf{y}|)$. For simplicity, we select a prescribed angular frequency and omit the notation in the functions hereinafter if clear. The subscript m denotes the source emanated from the location $\mathrm{s} = \mathrm{s_m}$. Let g_m be the difference field between p_m and p_m^{inc} acquired at the receivers for all source numbers $m = 1, \cdots, M$. In **vandenBerg1997**; **vandenBerg1999**; **Lin2016**; **Ozmen-Eryilmaz**, the contrast source denoted by $v_m = \chi p_m$ is introduced as an auxiliary function in Eq. (4.2.3). To recover the contrast function and the contrast source numerically from the given dataset $g_m (m = 1, \cdots, M)$, the robust CSI method is employed to solve Eq. (4.2.3) by minimizing the following two-variable cost functional:

$$J[\chi, v_1, \cdots, v_M, \gamma] = \sum_{m=1}^{M} V_m[v_m, \chi] + \lambda\|\nabla\chi\|_{L^1(D)}, \tag{4.2.4}$$

with

$$V_m[v_m,\chi] = \frac{\mu_D[\chi]}{\mu_S}\|G^S v_m - g_m\|^2_{L^2(S)} + \|\chi G^D v_m - v_m + \chi p_m^{\mathrm{inc}}\|^2_{L^2(D)}, m = 1, \cdots, M, \tag{4.2.5}$$

where the weights $\mu_D[\chi] = \sum_{m=1}^{M} \|\chi p_m^{\mathrm{inc}}\|^2_{L^2(D)}$ and $\mu_S = \sum_{m=1}^{M} \|g_m\|^2_{L^2(S)}$ and γ represents the regularization parameter.

4.2.1 Data processing for pulse data

The time-domain wavefield measurements are simulated by the K-wave toolbox(**Treeby2010**). Each source emanates a Gaussian pulse wave and the pulse excitation is of the form:

$$Q(t) = Q_0 e^{-8\ln 2(t/T-1/2)^2}\sin(\omega_c t), t \in [0, T], \tag{4.2.6}$$

where T is the duration time of pulse, ω_c the center angular frequency, and Q_0 controls the amplitude on the center angular frequency. Now the frequency-domain data are computed with the Fourier transform of the time-domain measurements. The excitation shown in Eq. (4.2.6) helps us to determine the bandwidth of the corresponding frequency-domain data.

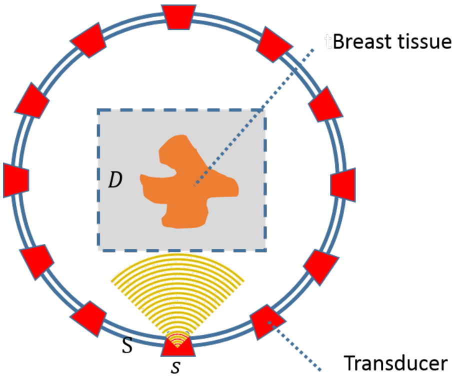

FIGURE 4.1: Schematic diagram of ultrasound waveform tomography with a ring-array transducer.

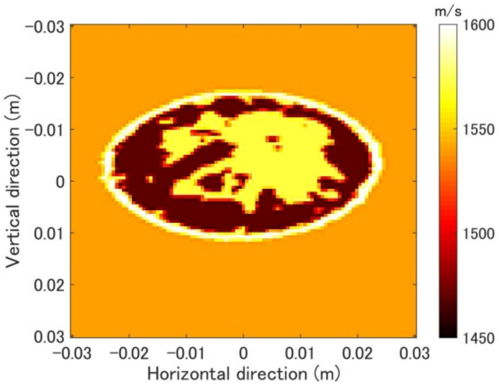

FIGURE 4.2: A breast phantom model that has a heterogeneous distribution of speed of sound.

Moreover, to make sure that these measurements coincide with the synthetic wave field computed by Eq. (4.2.3), for each frequency component, they are required to modify the amplitude and phase. Therefore, we first give the relation of the synthetic scattered wave field g_m with the help of the synthetic incident wave field g_m^{inc}, and the measurements of the total wave field p_m and the incident wave field p_m^{inc} as follows

$$g_m = \frac{|g_m^{\text{inc}}|}{|p_m^{\text{inc}}|}(p_m - p_m^{\text{inc}}). \tag{4.2.7}$$

Additionally, the inherent phase difference, caused by the dispersion error in the numerical simulator or the delay of the transducer response in the real data, should be moved out according to *a priori* information.

4.2.2 Algorithm of RCSI-ACR

The algorithm of RCSI-ACR applied to the single-frequency measured data was given in **Lin2016**. It mainly utilizes the alternating minimization method to solve the minimization problem of the cost functional (4.2.4) for the contrast function χ and the contrast source function v_m. The loop painted shadow on the background of callouts in Fig. 4.3 illustrates the process of RCSI-ACR. For the present iteration step k and the prescribed order n of the frequency-domain dataset, we first solve the minimization problem of $V_m[v_m; \chi^{(k,n)}]$ for v_m, fixing $\chi := \chi^{(k,n)}$ for all $m = 1, 2, \cdots, M$. The calculation result is denoted by $v_m^{(k+1,n)}$. Next, solve that of $J[\chi; v_1^{(k+1,n)}, \cdots, v_M^{(k+1,n)}, \gamma^{(k+1,n)}]$ for χ, fixing $v_m := v_m^{(k+1,n)}$ for all $m = 1, 2, \cdots, M$. The result is denoted by $\chi^{(k+1,n)}$. Repeat the loop until k reaches the maximal iteration step $K_{\max}$, or the cost function (4.2.4) is less than the threshold ε.

The automatic choice rule of regularization parameter is added to the alternating minimization method in order to update the regularization parameter λ while iterating. Incorporating this rule alleviates the influence to the numerical results of the CSI method, which is caused by the noisy measurements. To mathematically introduce the rule, we write $J(\gamma^{(k,n)}) := J[\chi^{(k,n)}; v_1^{(k+1,n)}, \cdots, v_M^{(k+1,n)}, \gamma^{(k,n)}]$ and $J'(\gamma^{(k,n)}) := \|\nabla\chi^{(k,n)}\|_{L^1(D)}$ as the abbreviations of the cost function and its derivative. Then the updating scheme of the regularization parameter is given by

$$\gamma^{(k+1,n)} = \frac{b^{(k,n)}}{\sigma(J(\gamma^{(k,n)}) - \gamma^{(k,n)} J'(\gamma^{(k,n)})) - a^{(k,n)}} - c^{(k,n)}, \tag{4.2.8}$$

where the coefficients $a^{(k,n)} = \sigma \sum_{m=1}^{M} \|v_m^{(k+1,n)}\|_{L^2(D)}^2$, $b^{(k,n)} = -\frac{(a^{(k,n)} - J(\gamma^{(k,n)}))^2}{J'(\gamma^{(k,n)})}$, $c^{(k,n)} = \frac{a^{(k,n)} - J(\gamma^{(k,n)})}{J'(\gamma^{(k,n)})} - \gamma^{(k,n)}$, and the constant $\sigma > 1$. For the derivation of Eq. (4.2.8), see s**Lin2016**; **Clason2010a**; **Clason2010b** and the references therein.

In terms of discretization for the cost functional (4.2.4), we use the Nyström method giving the straightforward approximation of the integrals by the quadrature rule (**Kress2014**). The composite trapezoidal rule, one of the quadrature rules, constructs the numerical integration by interpolating the integrand at each quadrature point.

4.2.3 Multi-frequency accelerating strategy

The idea of multi-frequency accelerating strategy is that it tries to achieve the rapid convergence result of the contrast function using the low-frequency data on a coarse grid, and then restart the RCSI-ACR method through utilizing the last iteration result and the high-frequency data on a fine grid, leading to the improvement of the resolution. This method is called frequency hopping which has been presented in **VandenBerg2001**. We consider that the value of points per wavelength is fixed for all frequency components, for instance, less than twenty(**Alles2011**). As the frequency increases while we do frequency hopping, the computational burden of RCSI-ACR enlarges gradually because of the increasing number of grids for each frequency component.

Moreover, compared with RCSI-ACR using single-frequency data, this strategy significantly prevents the reconstruction from being trapped into a local minima (**VandenBerg2001**).

Figure 4.3 shows the flow chart of the multi-frequency accelerating strategy. RCSI-ACR is conducted on a single-frequency component of dataset. After the substep of RCSI-ACR terminates, the output contrast function will switch to the initial guess in the next frequency component. In each loop, the initial contrast source function $v_m^{(0,n)}$ is reset by calculating the forward solver of Eq. (4.2.3), for instance the algorithm proposed in **Aguilar2004**. The regularization parameter is also restarted from the given initial guess. In numerical implementation, the interpolation should be additionally applied to the contrast function f when frequency hopping is done, since the computational grids become fine.

4.3 Numerical results

The numerical test is carried out on a breast phantom model from segmentation of the magnetic resonance images shown in Fig. 4.2 (see also **Qu2015a** and **Lin2016**). In it, speeds of sound are indicative of the different parts of the tissue; see Tab. 4.1. The K-wave toolbox generates the Gaussian pulse data with a center frequency of 0.25 MHz on a ring-array transducer with a radius of 0.045 m and 256 source/receiver pairs equally spaced. Here is a remark that frequency is expressed as $\omega/2\pi$. The breast model is immersed in a water tank. The background speed of sound is 1540 m/s. ROI is a square region centered at the origin with an area of $0.06 \times 0.06\mathrm{m}^2$. Here is a remark that although the numerical configuration is different from that of the diagnostic system, this shrinking scale is used for the sake of calculating convenience.

TABLE 4.1: Speed of sound for different parts of the breast tissue.

Tissue	Speed of sound (m/s)
Water	1540
Adipose	1470
Glandula	1570
Skin	1600

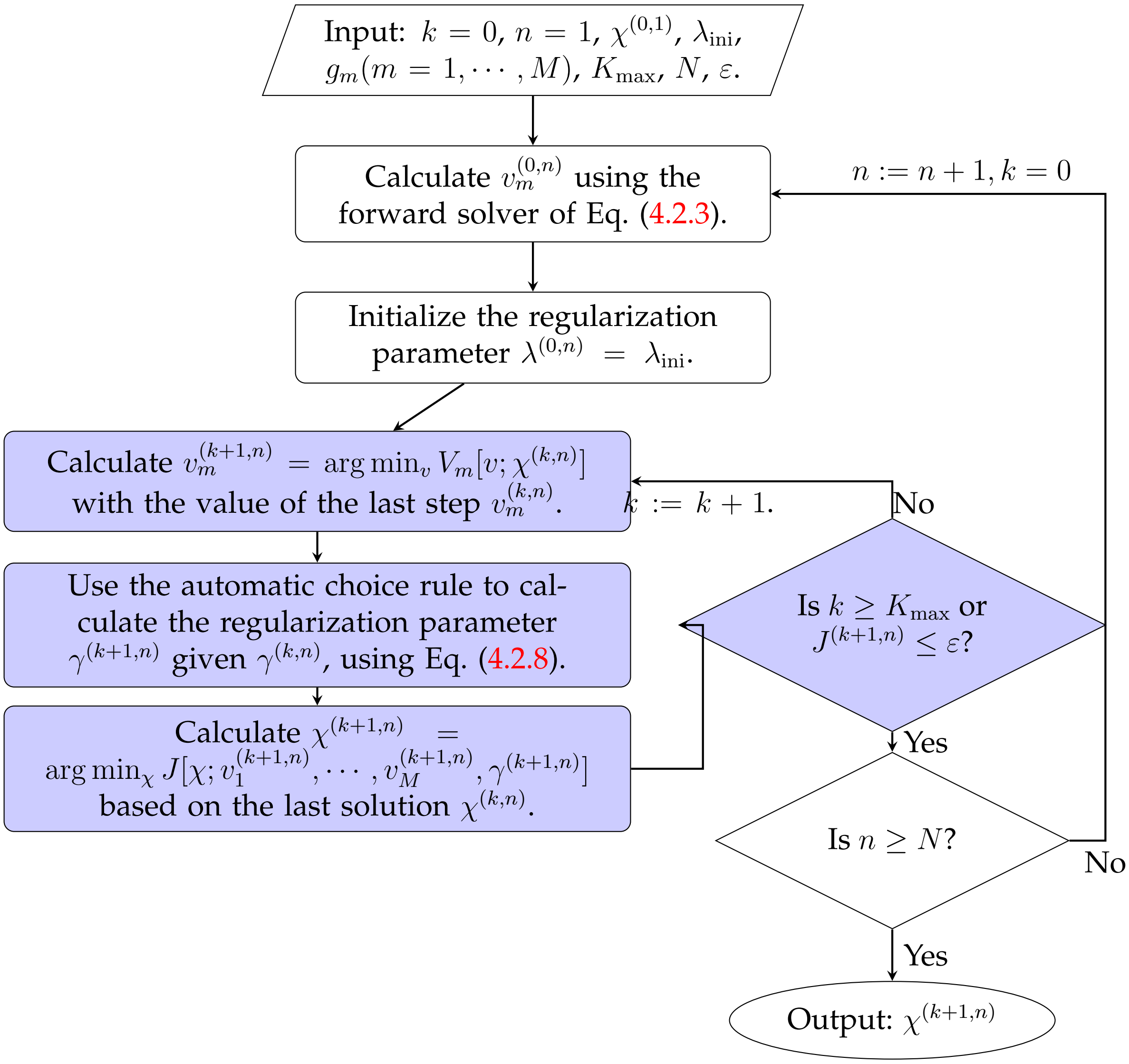

FIGURE 4.3: The flow chart for RCSI-ACR with multi-frequency accelerating strategy. $J^{(k+1,n)}$ denotes the value of $J[\chi^{(k+1,n)};v_1^{(k+1,n)},\cdots,v_M^{(k+1,n)},\lambda^{(k+1,n)}]$.

By now, we have obtained the raw dataset from the K-wave simulator received at the transducer. Then, we do Fourier transform to the dataset so as to get its frequency-domain components. In this numerical test, we extract ten samples of the equi-spaced frequencies from the dataset with respect to each receiver. These ten equi-spaced frequencies ($N=10$) sequentially range from 0.1 MHz to 0.3 MHz, covering the center frequency of 0.25 MHz. Meanwhile, a test on a single frequency dataset of 0.3 MHz is employed as a reference experiment for the conventional RCSI-ACR method. We configure twelve points per wavelength for all the tests, which leads to different grids for each frequency.

We numerically investigate the accuracy and performance of RCSI-ACR using multi-frequency accelerating strategy. We test on various cases of $K_{\max}$, the maximum iteration steps of each frequency, for the multi-frequency dataset as well as the single-frequency dataset. In this test, choosing the sufficiently small threshold as $\varepsilon = 10^{-3}$ ensure that the stop criterion of iteration is only dependent on $K_{\max}$. The reconstructions of speed of sound are shown in Fig. 4.4. We observe that compared with the numerical results for the single-frequency (SF) dataset, the proposed method applied with the multi-frequency (MF) dataset obtains the higher quality of image when they are calculated in the same number of total iteration steps. The proposed method is able to fast reach a blurred but convergent image when the low-frequency components are merely applied. Next, Figure 4.5 shows the convergence of the proposed method for MF and SF datasets assessed by the root mean square error (RMSE)

$$\mathrm{RMSE} = \|c_{\mathrm{model}} - c_{\mathrm{cmp}}\|_{L^2(D)}, \tag{4.3.1}$$

where c_{model} and c_{cmp} are speed of sound for the phantom model and the numerical result, respectively. The unit of RMSE is m/s. The relation between speed of sound and the contrast function χ is $c = c_0/\sqrt{1+\chi}$. We can see that after the iteration is full developed for many steps, the smaller $K_{\max}$ we use, the more accurate the reconstructed image will be. Here is a remark that the plot for the case of the MF dataset of $K_{\max} = 10$ is incomplete since it terminates at the 100 steps.

We conduct the proposed method implemented on graphic-processing-unit (GPU) to see its computational cost. The GPU computing platform is built on a workstation of Dell precision tower 7910 with a graphic card of NVIDIA GeForce GTX TITAN X and calculated with Parallel Computing Toolbox of Matlab. The comparison of the computation cost on the different datasets is illustrated in Fig. 4.5. We see that for the MF dataset with $K_{\max} = 20$, the proposed method using multi-frequency accelerating strategy costs approximate 2.68 s per iteration, whereas for the case of the SF data with the frequency of 0.3 MHz the computational time per iteration rises to approximate 4.04 s. Moreover, after calculating several iteration steps, calculating on the MF dataset with larger $K_{\max}$ may have shorter computational time.

4.4 Discussion

In this work, we focus on implementing the CSI method using pulse wave data that consist of many frequency components. There are two reasons triggering this idea. The first one is that the high-center-frequency data measured by the diagnostic device does not match the low-frequency configuration of many numerical methods of ultrasound waveform tomography. This is because of the rapid increasing of computational cost and the slow convergence in high frequency calculation. Following the same idea in **Sandhu2015**, the iteration is started with the lower frequency in order to ensure the priority of the computing efficiency. The second one is that we try to take full advantage of the abundant frequency components from data instead of the single-frequency reconstruction. As shown in Sec. 3, the merit of multi-frequency accelerating strategy is that the computational burden at the first few iterations is alleviated because of the coarse grids, with an assumption of a fixed number of points per wavelength. The numerical results also show that it does not lose more accuracy compared with the single-frequency reconstruction.

We specify some implementing details of the numerical test. First, in terms of choosing the value of the maximum iteration steps $K_{\max}$, there is a tradeoff between the computational cost and the accuracy of the outcomes. The aforementioned analyses indicate that choosing a large $K_{\max}$ accelerates the calculation of iteration while a small one enhances the convergence rate of the algorithm. Additionally, in Fig. 4.5(a), as long as hopping happens, RMSE of the outcome for the first few steps gets unstable. It requires $5 - 10$ steps so that the algorithm returns to convergence again. Under the configuration of the numerical test, we recommend setting $K_{\max} = 20$. Another discussion is that our proposed method is able to be applied to the corrupted measurements, though the measurements in the numerical test is noise-free. In fact, the use of the total-variation penalty term $\|\nabla f\|_{L^1(D)}$ in the cost functional (4.2.4) endows with robustness against ill-posedness. Finally, we exclude the computational time of the forward solver for calculating the initial contrast source function $v_m^{(0,n)}$. This is for the purpose of precisely verifying that the multi-frequency accelerating strategy has better performance of both accuracy and the computational cost.

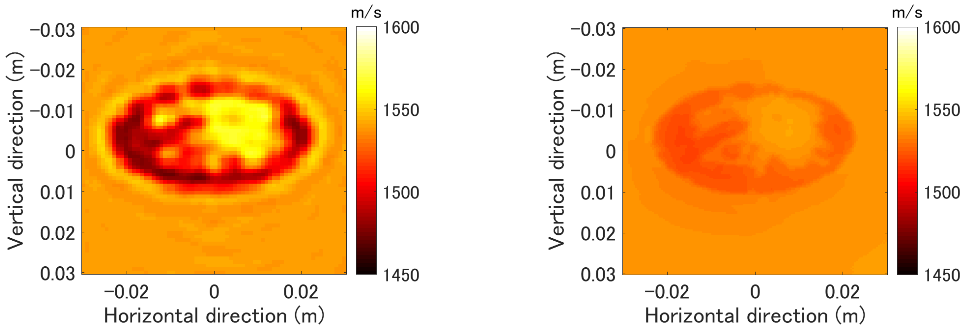

(a) MF ($K_{\max} = 20$ at 0.145 MHz), 50 iters (e) SF, 50 iters

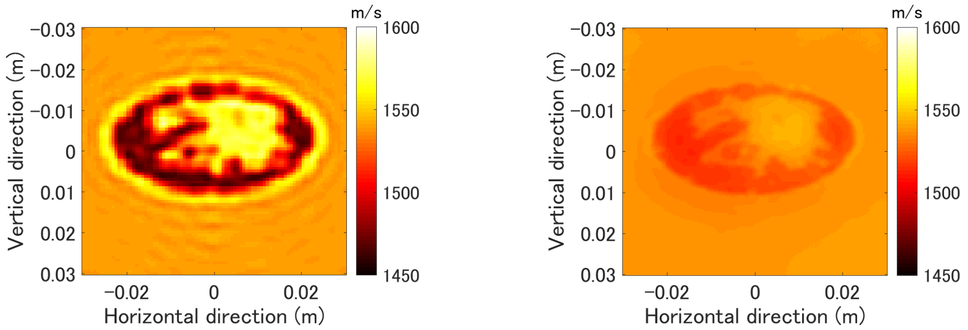

(b) MF ($K_{\max} = 20$ at 0.19 MHz), 100 iters (f) SF, 100 iters

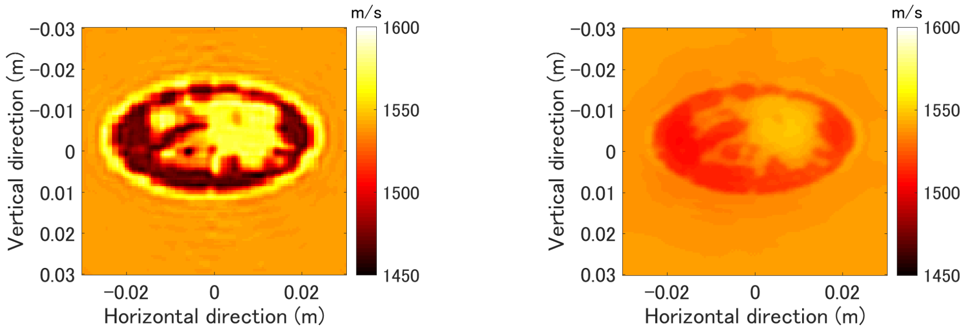

(c) MF ($K_{\max} = 20$ at 0.255 MHz), 150 iters (g) SF, 150 iters

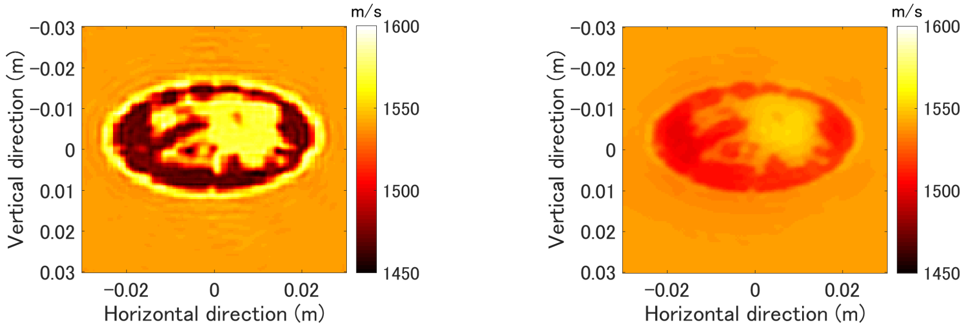

(d) MF ($K_{\max} = 20$ at 0.3 MHz), 200 iters (h) SF, 200 iters

FIGURE 4.4: Reconstructed images of sound-speed map for multi-frequency (MF) dataset with $K_{\max} = 20$ and single-frequency (SF) dataset with the frequency of 0.3 MHz using RCSI-ACR with multi-frequency accelerating strategy, respectively. Figures (a)-(d) are the results of the MF dataset at $50, 100, 150,$ and 200 total iteration steps (iters), whereas Figs. (e)-(h) are those of the SF dataset.

(a) Line plot

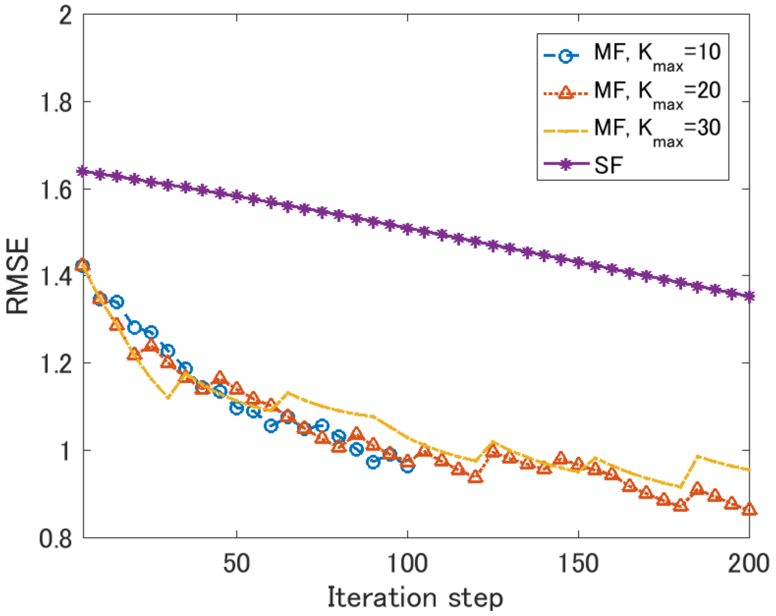

(b) Bar plot

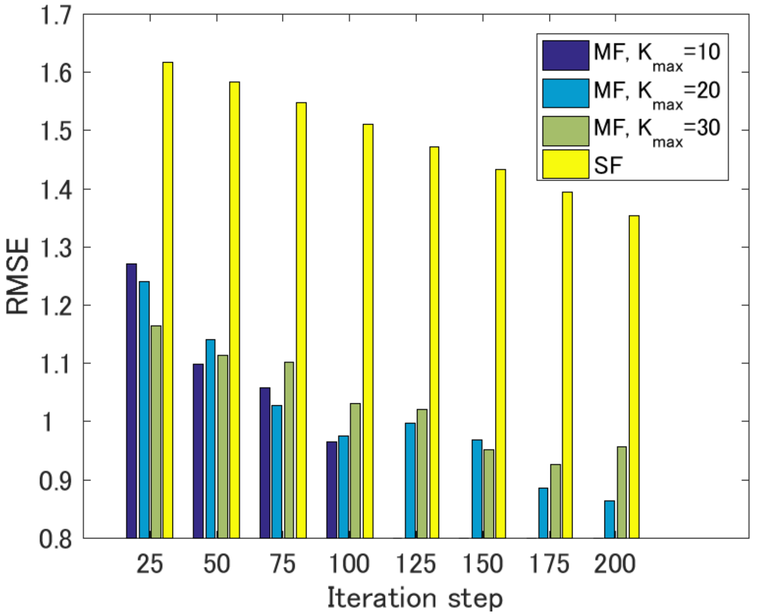

FIGURE 4.5: RMSE for the numerical solution of each iteration step using RCSI-ACR with multi-frequency accelerating strategy. The MF dataset with $K_{\max} = 10, 20, 30$ as well as the SF dataset with the frequency of 0.3 MHz are applied to the algorithm.

(a) Line plot

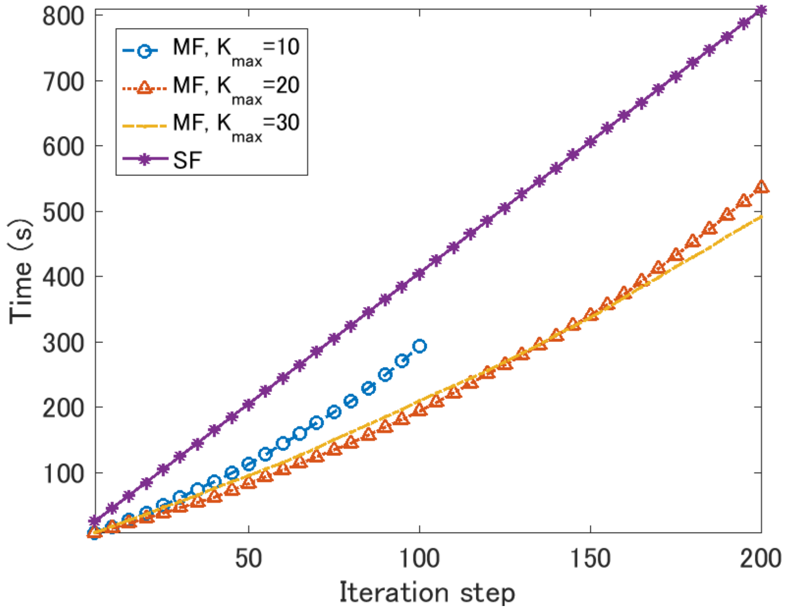

(b) Bar plot

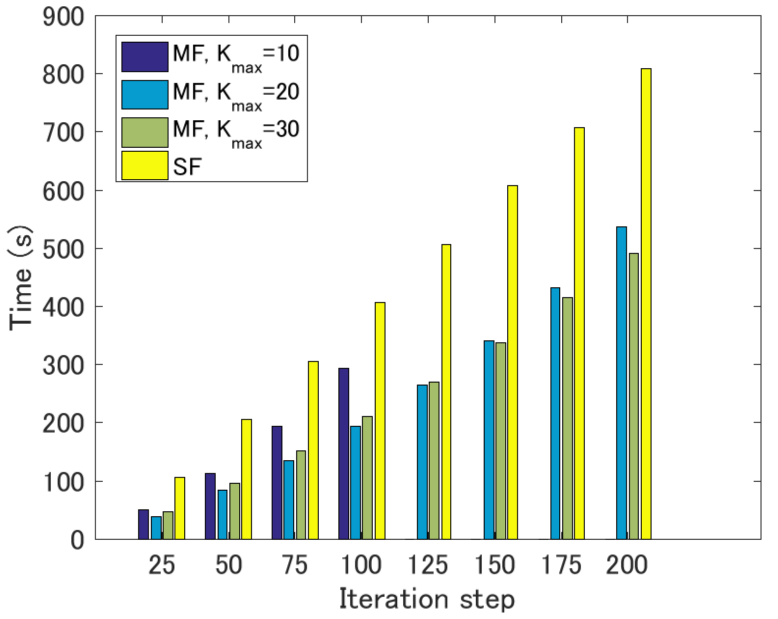

FIGURE 4.6: Computational time for the numerical solution of each iteration step using RCSI-ACR with multi-frequency accelerating strategy. The MF dataset with $K_{\max} = 10, 20, 30$ as well as the SF dataset with the frequency of 0.3 MHz are applied to the algorithm.

Chapter 5

Practical reconstruction from experimental data

5.1 Experimental setup

5.1.1 Ultrasound tomography system

The schematic diagram of the experimental device is shown in Figure 5.1. It is composed by the two parts: a ring-array ultrasound transducer and its driving hardware – "Verasonics". The experimental data of the ultrasound propagating through the experimental object will be measured, processed, and save in the Verasonics. The technical specifications of our ultrasound tomography system will be stated in the following text. More details are referred to **tamano2015compensation**.

Ring-array ultrasound transducer

Figure 5.2 shows the appearance of the ring-array ultrasound transducer. It consists of four pieces of concave rings whose central angle and radius are 90 degree and 104 mm, respectively. Each piece contains 256 piezoelectric elements, and totally 1024 elements are available on the ring. The technical specification for one piece is illustrated in Figure 5.3. The grating arrangement of the transducer has the 0.03 mm distance between the two adjacent elements. Each element is designed as an elongated bar of the 0.27-mm width and the 10-mm height. The center frequency of the pulse excitation from the element is 1.75 MHz. Moreover, an acoustic lens covering the transducer focuses the three-dimensional ultrasound waveform on the finite-height ring. This will help to acquire the two-dimensional waveform signal from the ultrasound propagating through the three-dimensional structure.

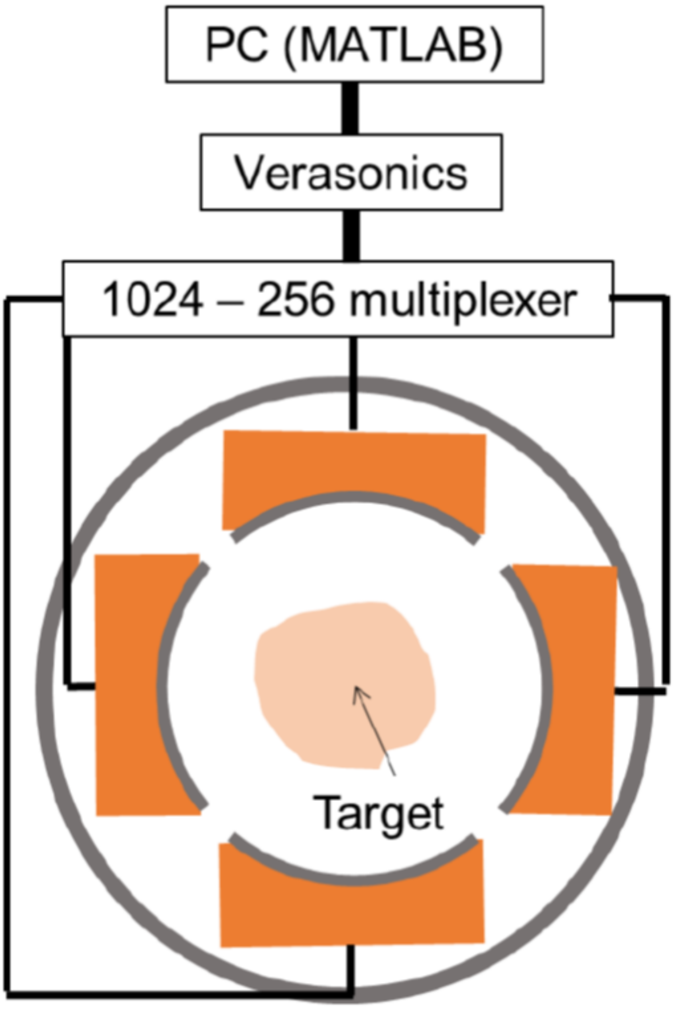

FIGURE 5.1: Schematic diagram of the ultrasound tomography system. (**Nakamura2014**)

Driving hardware

Our ultrasound tomography system is driven by the type V1-4board of Verasonics. Via the switching circuit with 1024 to 256 multiplexer, the ring-array ultrasound transducer is connected to Verasonics. Matlab programming environment is used to manipulate data acquisition and data analysis of the signal. Since Verasonics has ability to simultaneously control 256 emitter elements at most, the acquired dataset contains 1024-receiver-times-256-emitter time sequences for one scanning.

Time delay may occur during the data acquisition. First, switching the element from transmitting mode to receiving mode will cost the order of several microsecond for each element. The duration time of the analog-to-digital (A/D) converting carried out on the receiver is approximate 4.0 nanosecond. Therefore, the delay is assumed to be neglected for a full acquisition time of

FIGURE 5.2: Appearance of the ring transducer.

the order of several millisecond.

5.1.2 Experimental object

In this study, the urethane phantom is chosen as the experimental object and the reconstruction is based on the ultrasound phantom data. Urethane has a slower speed of sound than water in the room temperature (1483 m/s in the $20°C$ water). Usually, the transparency of urethane is related to the value of the speed of sound while the stiffness has impact on the attenuation coefficient. The products of the urethane gel made by Exseal Corporation enable us to mould the prescribed shape of phantom and control its transparency as well as stiffness.

In order to assess the accuracy and resolution of the aforementioned reconstruction algorithms with regard to applying experimental data, this study attempts to reconstruct two phantom models: the transparent soft urethane phantom having a slow speed of sound but a weak attenuation coefficient, and the opaque hard one having a similar speed of sound as water but a strong attenuation coefficient.

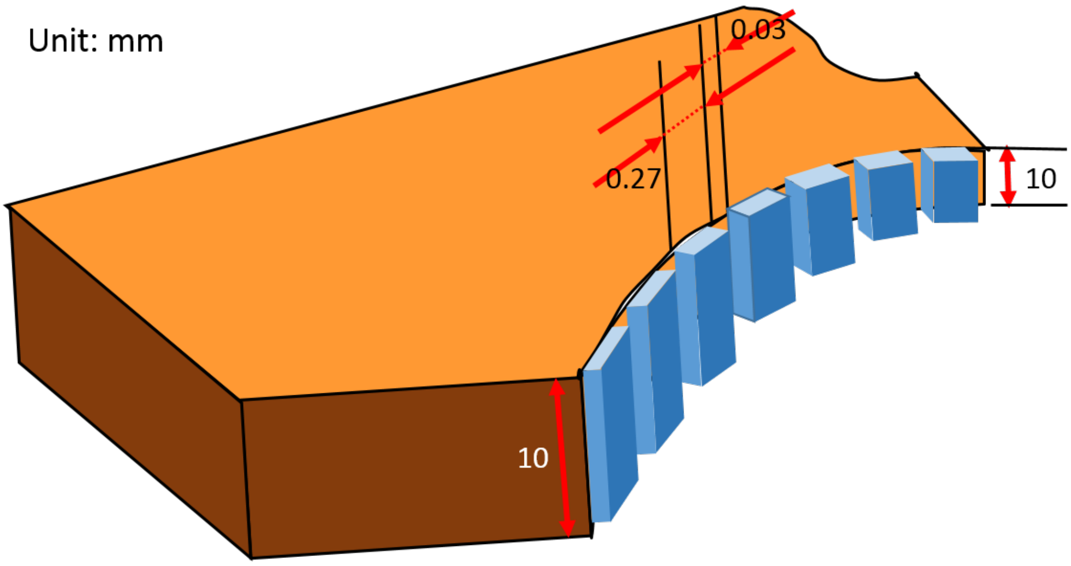

FIGURE 5.3: A piece of the quarter ring transducer.

5.2 Data processing

5.2.1 Acquired data analysis

In this subsection, the phenomenon emerging from the observation of the ultrasound waveform data is analyzed. The transducer elements for emitters and receivers are numbered from the same starting point along the direction of counter clockwise. The raw data are acquired by the aforementioned ultrasound tomography system. We present a common shot gather emanated from the element number one on the transducer through a homogeneous media of water with the absence of the phantom model. Here the common shot gather means a collection of the ultrasound signals recorded as the time series from one shot to many receivers. To clearly illustrate the intensity of the waveform, we take the logarithm of the absolute value of the wave signals for the common shot gather shown in Figure 5.4.

The band in the region 1 represents the control signals which instruct the transducer elements switching from transmitting mode to receiving mode. These exceptional signals are sufficiently strong to significantly impact the main signal because of the large amplitude and bandwidth. The transmitted wave is located in the region 2 where the waveform of the transmitted pulse arrives at the receivers with a distribution as an arch on the figure of the common shot gather. In specific, the first-arrival picking and the time duration of pulse determine the extraction of the transmitted wave. Moreover, the

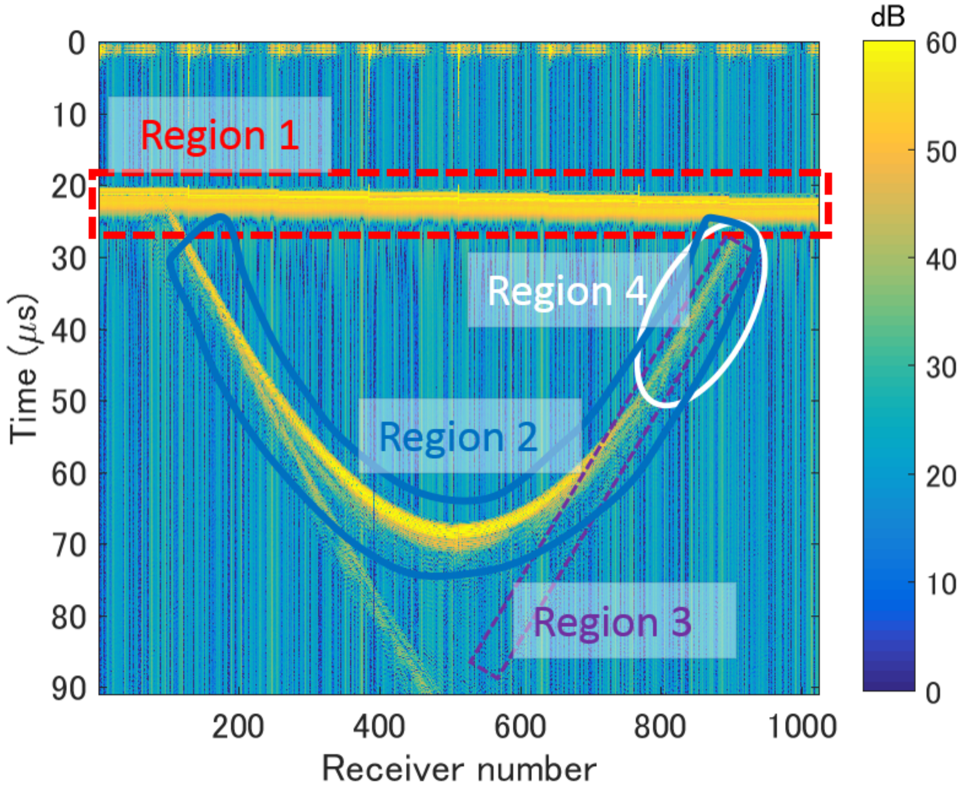

FIGURE 5.4: The common shot gather emanated from the source number one.

transmitted wave has strong directivity since the intensity of the received signal whose direction is perpendicular to the emitter element dominates, compared with the other directions. The region 3 contains the two rays caused by the reflected wave signals from the ring transducer. Note that the overlap of the transmitted pulse wave and the reflected boundary wave happening in the region 4 increases difficulty of the transmitted signal extraction.

5.2.2 Scattered wavefield data processing

To prepare the scattered wavefield data processing, we carry out two data acquisition process on the ultrasound tomography system with the presence and absence of the experimental object, resulting in the water dataset and the phantom dataset, respectively. Subtracting the phantom dataset with the water dataset yields the scattered wavefield dataset which include the information of contrast between water and phantom. The aim is to extract the particular group of the frequency components from the time-domain scattered wavefield dataset for all emitters and receivers. However, the discrepancy between the simulated forward problem and the real ultrasound propagation in the device is indeed existed on the aspects of the directivity of source, the boundary reflection, the uncertainty of the element's coordinates, etc. Hence, before the Fourier transform, the following steps of data processing are necessary to remedy the difference of the simulated wavefield data and the experimental wavefield data as much as possible.

Exceptional signal removing

The so-called exceptional signal is defined as the ultrasound phenomenon which is not explained in the simulated forward problem. Typically, the exception signals in the common shot gather of Figure 5.4 are the control signal lied in the region 1 as well as the boundary reflected signal in the region 3. To cope with the issue in the region 1, one can first find the common ending of the control signals and then reset the time series before the common ending as zero for all emitters and receivers. Since the control signals as well as the transmitted wave signals in the near offset are removed, together with the consideration of the overlapped signals, the components of the wavefield dataset whose receivers are lied in the near offset should be truncated. For instance, the receiver channels with the central angle of 144° are moved out including the overlapped region 4 shown in Figure 5.5.

Moving average filtering

Moving average filter is introduced to compensate the discrepancy of the signals for the adjacent receivers, which is caused by the independent sensitivity for each receiver element. We also take the common shot gather in Figure 5.4 as an example. Each received signal are rectified by means of taking the average of signal in its adjacent five receivers with respect to all the time series; see Figure 5.6 . As a result, the processed wavefield dataset on the dimension of receiver number become smooth.

First-arrival picking and exponential damping

This step is to extract the transmitted pulse signal and remove the boundary reflected signal. With the known duration time of the pulse signal, the time-of-flight (TOF) map determines the separation of the transmitted and reflected wave for each emitter-receiver pair. To calculate the TOF map, the

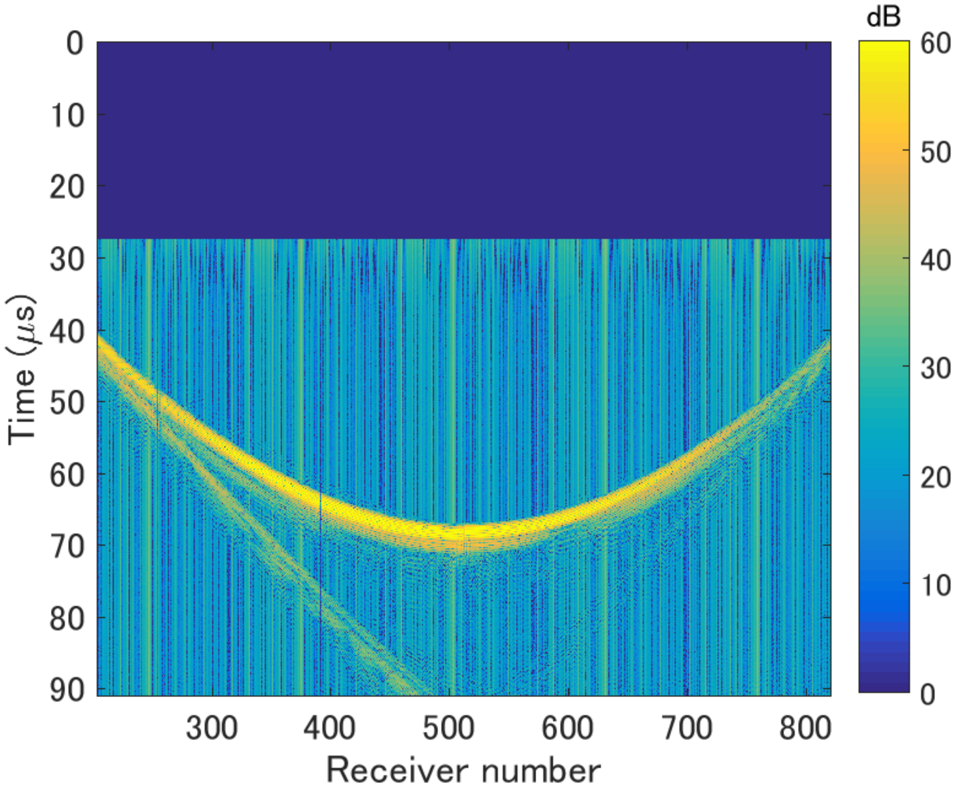

FIGURE 5.5: Exceptional signal removing which applies to the common shot gather.

automatic first-arrival picking method with the Akaike information criterion (AIC) is used (**qu2015novel**). The TOF map for the water dataset using the automatic first-arrival picking method with AIC is shown in Figure 5.7(a).

Instead of resetting the reflected signal, one dampens the tail of the transmitted signal with the use of the exponential filter in order to rapidly attenuate the non-transmitted signal. In specific, the exponential filter of the expression $\max\{1, \exp[-(t - t_0 - t_d)/\tau]\}$ is applied to the time series of the waveform dataset, as proposed in **sandhu2015frequency**. Here, t_0 denotes the time of flight, t_d is the duration time of the transmitted pulse for some emitter-receiver pair, and the factor τ determines the damping speed starting at the tail of the transmitted pulse. In our example, t_d is chosen as 6 μs and τ is approximate to 1 μs. The result is shown in Figure 5.7(b).

Transducer calibration

Calibrating the coordinates of the transducer elements has been carried out through the experimental test (**NakamuraPersonal**). This is one of the unpublished researches authored by H. Nakamura who is the staff from Lily

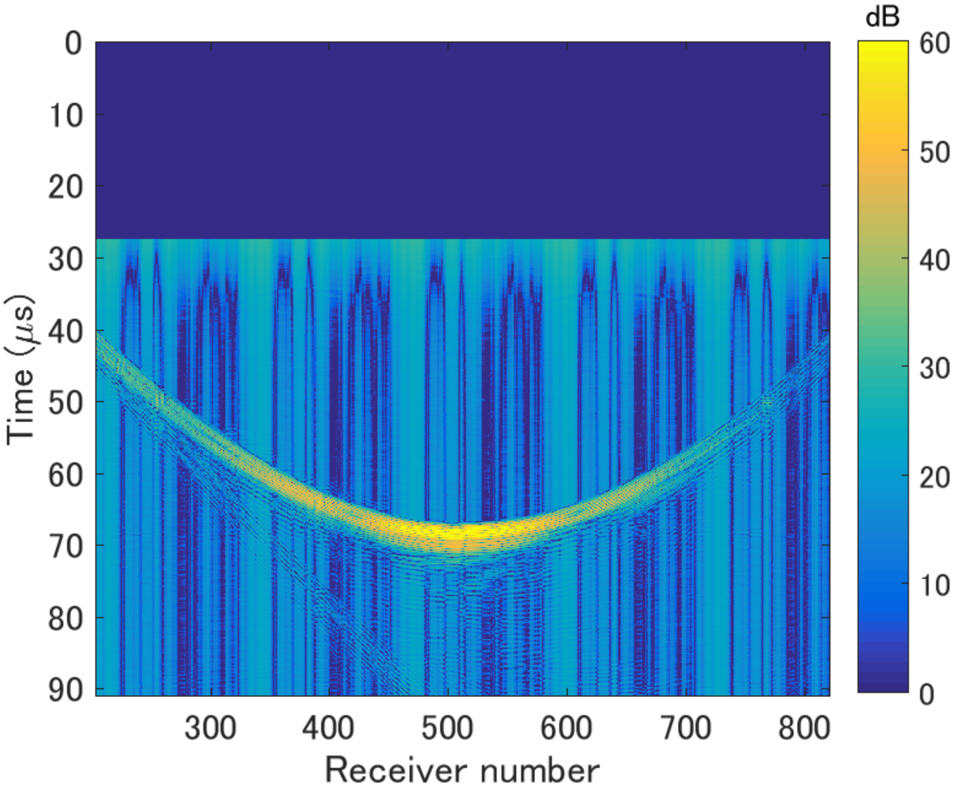

FIGURE 5.6: Moving average filtering which applies to the common shot gather.

MedTech Co. Ltd. The calibrated transducer elements will help to compensate the phase difference caused by the deviation of the element position.

Fourier transform

We apply the time-domain Fourier transform to the waveform dataset and extract some of the particular frequency components for all emitter-receiver pairs. Figure 5.8 shows the power spectrum of the received ultrasound signal in the water dataset. With the consideration of the effectiveness and computational cost, the frequency components lied in from $3/4$ to 1 of the center frequency will be extracted.

Beamforming

Beamforming is only conducted in the water dataset. It is used to synthesize the incident wavefield in the region of interest from many point sources on the ring transducer. Minimum variance beamforming (MVB) is one of the simple beamforming algorithm which solves the least square estimate of the

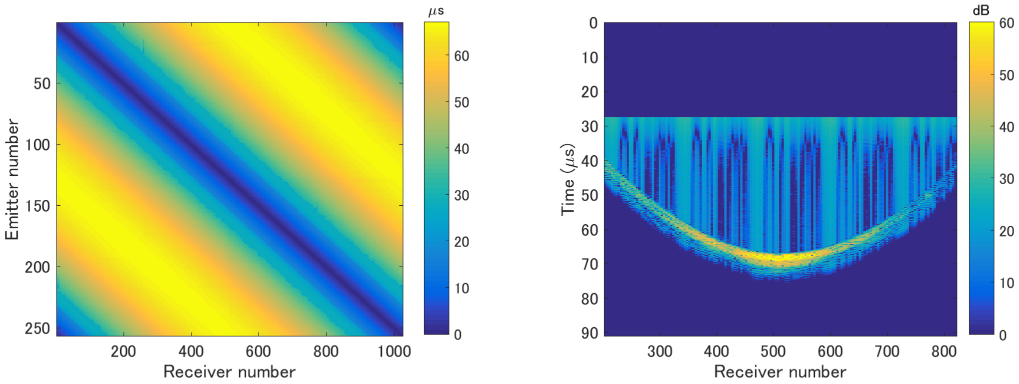

(a) The TOF map (b) Exponential damping

FIGURE 5.7: (a) The TOF map for the water dataset using the automatic first-arrival picking method with AIC. (b) Exponential damping which applies to the common shot gather.

weight $\mathbf{w}$ for the following formula (**VanVeen1988**):

$$\mathbf{P}^{\mathrm{inc}}\mathbf{w} = \mathbf{g}, \tag{5.2.1}$$

where $\mathbf{P}^{\mathrm{inc}}_{ij} = p^{\mathrm{inc}}(r_i, s_j, \omega)$ emanated from the source s_j is the entry of the spherical-incident-wavefield matrix which is done on the given angular frequency ω, $g_i = g(r_i, \omega)$ the wavefield data acquired at the receiver r_i, and the receiver and source numbers are $i = 1, 2, \cdots, N_r$ and $j = 1, 2, \cdots, N_s$, respectively. One numerical example in Figure 5.9 shows that the synthetic wavefield using MVB allows us to simulate the ultrasound wavefield propagating in our ultrasound tomography system.

5.3 Reconstruction from the processed experimental data

The reconstruction is carried out on the cutaway hemisphere urethane phantom; see Figure 5.10. The experimental data is processed in accordance with Section 5.2. Table 5.1 shows the speed-of-sound and attenuation coefficient reconstruction with the use of the processed experimental dataset.

Fq (MHz)	Speed-of-sound	Attenuation

1.2	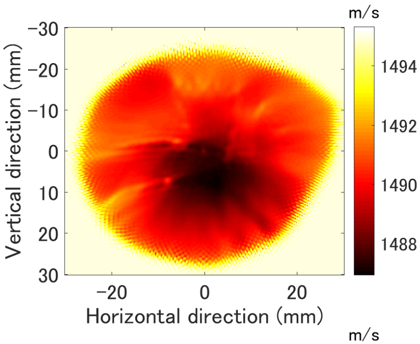	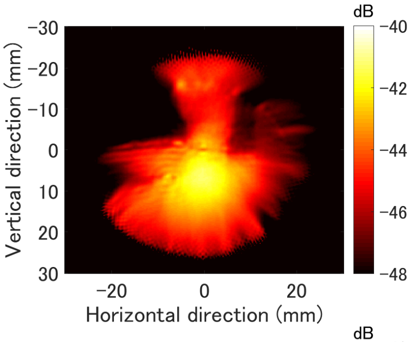
1.6	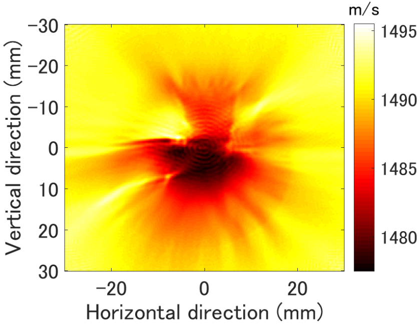	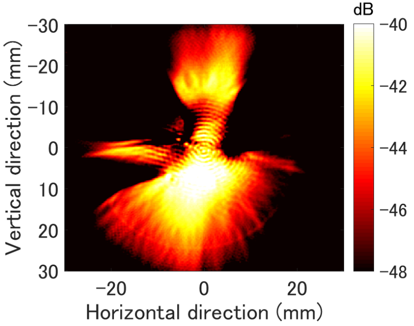

TABLE 5.1: Speed-of-sound and attenuation coefficient reconstruction with the use of the experimental dataset. The reconstruction results at the two targeted frequency components are conducted.

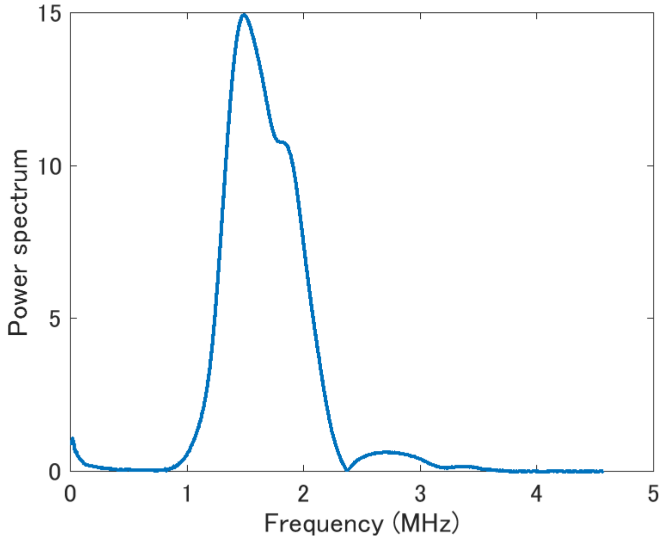

FIGURE 5.8: Power spectrum of the water dataset for the source number 1 and the receiver number 512 applying the Fourier transform.

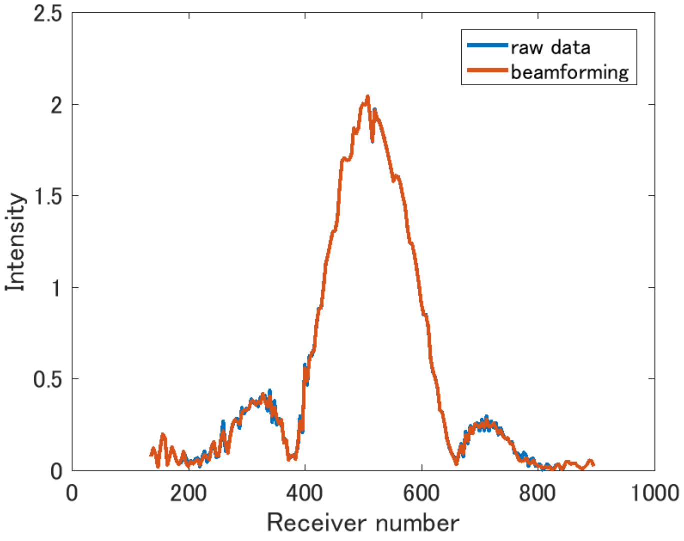

FIGURE 5.9: Minimum variance beamforming.

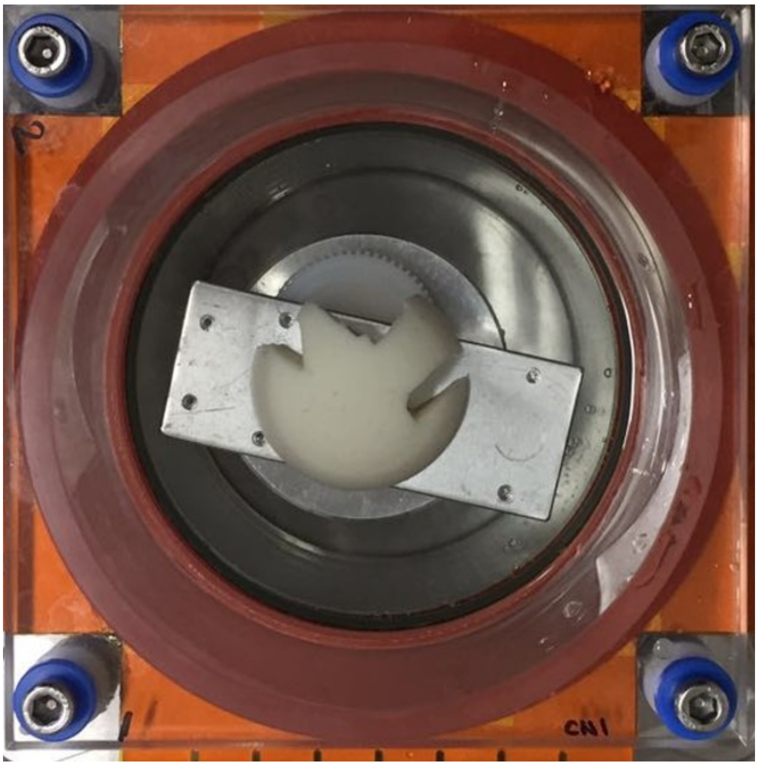

FIGURE 5.10: Cutaway hemisphere urethane phantom.

Chapter 6

Conclusions

In this work, an alternating minimization method with the automatic choice rule of regularization parameters is developed for numerical computation of the robust CSI method. In order to stipulate that this algorithm is universally valid, the convergence results of the method is specifically discussed in this paper. In particular, the automatic choice rule avoids the artificial and empirical determination of the trials of regularization parameters prior to executing the algorithm. This not only saves the number of implementation times but also improves the spatial resolution of the reconstructed image. Moreover, the numerical results show that the use of the automatic choice rule sharpens the edge in the reconstructed image as well as filters out high-frequency noise, in comparison with the fixed regularization parameter.

Chapter 4 demonstrates a multi-frequency accelerating strategy for the CSI method using pulse data in the time domain. The CSI method of ultrasound waveform tomography in the frequency domain is introduced. The idea of frequency hopping helps restart CSI in the current frequency using the result obtained from the former frequency reconstruction. In the numerical test, the data were generated by the K-wave simulator and have been processed to meet the computation of the CSI method. One conducts a numerical study to demonstrate the performance of the multi-frequency and single-frequency reconstruction. It turns out that the multi-frequency accelerating strategy significantly reduces the computational cost as well as improves the convergence rate.

In Chapter 5 (to be appeared) , the urethane phantom images are calculated by applying the experimental measurements acquired from the prototype of the ring transducer. The result shows that the structure of this defective hemisphere is successfully reconstructed by the attenuation image rather than the speed of sound image. This is because the calibration of the source/receiver locations is required to correct the phase information in the measurement. Moreover, the gap between the governing equation and the real phenomenon probably depends on the boundary condition related to the reflectivity of the ring transducer and the bad channels because of the intrinsic defects in the structure of transducer.

In Appendix B, TR is first developed to recover the initial-pressure distribution rather than the inversion of the wave propagation. In the TR equations, the measurements are reversed and considered as a time-varying Dirichlet boundary condition in IBVP of the wave equation. As a modification, IA is derived from IVP of the wave equation with the pressure source provided by the time-reversal measurements, which is free of the computation of the Dirichlet Green's function. Compared with the TR method, it turns out that the IA method works out a higher-resolution image, with merely few numbers of receivers deployed.

Theoretically, the higher-order weights of the angular frequency ω in the IA formula indicate that high frequency components in the measurements take more effect on the aspect of the contrast at the high-resolution points, although the TR and IA methods have the identical basis for each spatial point in the imaging domain D. In the numerical tests, we even see that the high-resolution image calculated by IA is preserved at the sub-Nyquist sampling rate by the sensors along the ring, whereas the TR method is vulnerable to the sampling criterion. Numerically, the low-pass filter stipulates the robustness of the IA method when the received measurements are corrupted by the noise.

Appendix A

Exact wavefield of the circular scatterer

In this section, one reviews the derivation of the exact wavefield on a circular scatterer B of radius r_B composed by the constant wave number k different from that k_0 of the background. First, one can write the expansion of fundamental solution:

$$\frac{i}{4}H_0^{(1)}(k|x-y|) = \frac{i}{4}\sum_{n=-\infty}^{\infty} H_n^{(1)}(k|x|)J_n(k|y|)e^{in(\theta-\varphi)} \tag{A.0.1}$$

which is valid for $|x| \geq |y|$. Here θ and φ denote the phases (angles) of x and y respectively.

For $x \notin \bar{B}$, the total wave u is solved by the homogeneous Helmholtz equations, and split into the incident wave u^i and the scattered wave u^s. By (A.0.1) and (**??**), we have the form of u^i and u^s

$$u^i(x) = \sum_{n=-\infty}^{\infty} \gamma_n J_n(k_0|x|)e^{in(\theta-\psi)}, x \notin \bar{B} \tag{A.0.2}$$

and

$$u^s(x) = \sum_{n=-\infty}^{\infty} \alpha_n H_n^{(1)}(k_0|x|)e^{in(\theta-\psi)}, x \notin \bar{B}, \tag{A.0.3}$$

where α_n and γ_n are the coefficients with respect to inner boundary conditions, and ψ is the propagated angle of the incident wave. If we assume the plain incident wave $u^i(x) = e^{ik_0 x\cdot d}$, then the coefficient is definite

$$\gamma_n = i^n, d = (\cos(\psi), \sin(\psi)). \tag{A.0.4}$$

Similarly, for the spherical incident wave $u^i(x) = \Phi_z(x)$, then

$$\gamma_n = \frac{i}{4} H_n^{(1)}(k_0|z|), z = |z|e^{i\psi}. \tag{A.0.5}$$

For $x \in B$, we use the idea of Green's Representation Theorem to express the solution u^r of interior Helmholtz equation (see p.p. 68 Colton Kress 82)

$$u^r(x) = \sum_{n=-\infty}^{\infty} \beta_n J_n(k|x|) e^{in(\theta-\psi)}. \tag{A.0.6}$$

The connecting condition of u on ∂B can be determined from the same pressure and pressure gradient (velocity) inside and outside the boundary; see Thompson 76. That is,

$$\begin{cases} u^i(x) + u^s(x) = u^r(x) & x \in \partial B, \\ \frac{\partial u^i}{\partial \nu}(x) + \frac{\partial u^s}{\partial \nu}(x) = \frac{\partial u^r}{\partial \nu}(x) & x \in \partial B. \end{cases} \tag{A.0.7}$$

Since the orthogonality of the basis $\{e^{in\theta}\}$, it follows from (A.0.7) that

$$\begin{cases} \gamma_n J_n(k_0 r_B) + \alpha_n H_n^{(1)}(k_0 r_B) = \beta_n J_n(k r_B) \\ \gamma_n k_0 \frac{\partial J_n}{\partial \nu}(k_0 r_B) + \alpha_n k_0 \frac{\partial H_n^{(1)}}{\partial \nu}(k_0 r_B) = \beta_n k \frac{\partial J_n}{\partial \nu}(k r_B). \end{cases} \tag{A.0.8}$$

Here the calculation of the derivative of any Bessel functions can refer to the following expression

$$j_n'(r) = \frac{n}{r} j_n(r) - j_{n+1}(r), r > 0. \tag{A.0.9}$$

Then using Cramer's Rule and (A.0.9), we find the solutions of α_n

$$\alpha_n = \gamma_n \frac{k J_{n+1}(k r_B) J_n(k_0 r_B) - k_0 J_{n+1}(k_0 r_B) J_n(k r_B)}{k_0 H_{n+1}^{(1)}(k_0 r_B) J_n(k r_B) - k J_{n+1}(k r_B) H_n^{(1)}(k_0 r_B)}. \tag{A.0.10}$$

Appendix B

Photacoustic imaging: resolution and sensor-element sampling

B.1 Introduction

Photoacoustic imaging (PAI) is a three-dimensional imaging modality that uses the photoacoustic effect. When light is absorbed by the tissue and converted to heat, an acoustic wave is generated due to the thermoelastic expansion of the heated volume. Therefore, PAI is an elegant combination of optical imaging and ultrasound imaging. It combines the rich optical contrast with high spatial resolution of ultrasound imaging. Moreover, PAI is a multiscale imaging system in the sense that it provides, molecular, functional and anatomical information in a single modality. More details of the photoacoustic imaging are referred to the reviews (**Wang2008**; **Li2009**; **Beard2011**).

In PAI the main goal is to recover the initial pressure distribution. There exists one of the PAI methods which quantitatively illustrates the optical properties of the soft tissue. For instance, based on the mathematical modeling and the numerical study, the inverse spherical Radon transform is used to the study of the quantitive PAI; see the references **Xu2006**; **Kunyansky2007**. Moreover, PAI has succeeded in dealing with the more realistic situation on attenuation (**Ammari2012**; **Cox2010**; **Huang2013**), the variable speed of sound (**Modgil2010**; **Zhang2008a**; **Zhang2008b**), and the dynamic photoacoustic tomography (**Wang2014**). The regularization methods are applied to alleviate the ill-posedness appealing in the inverse problem of PAI, especially when the measurements are corrupted by the noise; see for example **Arridge2016b**.

Compared with the quantitative PAI, a category of the approximate reconstructions, such as the time-reversal methods (**Kowar2014**), interferometric imaging (**Vasconcelos2010**; **Halliday2010**), back-projection (**Xu2005**), synthetic aperture (**Berer2012**), etc., considers the physical and medical essence of PAI instead of the inversion for the forward process. These methods employ the imaging function to depict the structure, function, and interface of the tissue in the morphology via assessing the spatial resolution and the contrast of images instead of the quantitative physical properties. The characteristics of cancer and other pathology may be revealed if the high-quality image achieves. The approximate reconstructions have the low computational burden as well as the matched thinking way to the engineers.

In this manuscript, we focus on the study of the time-reversal methods and the interferometric imaging with the assessment of the resolution. In the literature, the theoretical research on the time-reversal methods was first proposed in **Fink1992**, and got abundant applications (**Xu2004**; **Yanik2004**; **Moura2007**). On the other hand, interferometry is developed to extract the Green's function in heterogeneous media in seismology (**Snieder2004**; **Wapenaar2006**). Specifically, two impulsive sources are enclosed within the receiver arrays. Cross-correlating wavefields emanated from these two sources yields the Green's function between them as if one of them can be regarded as a virtual receiver (**Curtis2009**). Wavefield imaging based on interferometry has been studied in **Halliday2010** and **Vasconcelos2010**. **Ammari2011** discusses the connection between the time-reversal methods and the interferometric imaging in PAI. In this study, we further propose qualitative and quantitative analyses on the resolution study of both methods in the lossless homogeneous media. The analyses and the numerical results both show that the interferometric imaging produces a higher resolution and contrast image, even with sub-sampling numbers of receivers located on the ring-shaped transducers. Moreover, considering that the measurements are corrupted by the Gaussian noise, the numerical scheme for the interferometric imaging is utilized with the use of interferometry derived in the frequency domain and low-pass filter as well. And the use of the low-pass filter enhances the robustness of it.

The manuscript is organized as follows: In Section B.2, the forward problem of PAI and its solution represented by the integral form are reviewed. The time-reversal photoacoustic imaging method and the interferometry alternative one consisting of image reconstruction for PAI are formulated both in the continuous and semi-discrete expressions with the measurement recorded on a ring array. The main contribution of this paper is proposed in Section B.3. The analyses on the resolution and the sampling by the sensor elements show an intrinsic distinction between the two imaging methods when the finite number of sensor elements on the ring array is considered. In section B.4, the numerical tests are presented to show the image quality of the two photoacoustic imaging methods quantitatively assessed by the resolution and contrast. This manuscript is discussed and concluded in Section B.5 and Section **??**.

B.2 Methods

Consider that the photoacoustic wave excites and propagates in a two-dimensional lossless homogeneous medium; see Figure B.1. It is governed by the acoustic wave equation

$$\left(\nabla^2 - \frac{1}{c_0^2}\frac{\partial^2}{\partial t^2}\right) p(\mathbf{x},t) = -\frac{\beta}{C_P}\frac{\partial H}{\partial t}(\mathbf{x},t), \quad (\mathbf{x},t) \in \mathbb{R}^2 \times (0,T), \tag{B.2.1}$$

where $p(\mathbf{x},t)$ is the acoustic pressure at point $\mathbf{x}$ (unit: m) and time t (unit: Pa) and $H(\mathbf{x},t)$ the heat generation from optical absorption per unit volume and time [unit: $J/(m^3 \cdot s)$]. The parameter c_0 denotes the speed of sound (unit: m/s), β denotes the thermal coefficient of volume expansion (unit: K^{-1}), and C_P denotes the specific heat capacities at constant pressure [unit: $J/(Kg \cdot K)$]. The time T is a large terminal time such that

$$p(\mathbf{x},t) = 0 = \frac{\partial p}{\partial t}(\mathbf{x},t), \quad \mathbf{x} \in \mathbb{R}^2, t \in (-\infty,0] \cup [T,+\infty). \tag{B.2.2}$$

With the assumption of a short optical illumination, the heat generation $H(\mathbf{x},t)$ is separated as $H(\mathbf{x},t) = A(\mathbf{x})\delta(t)$ where $A(\mathbf{x})$ is the specific optical absorption and $\delta(t)$ is the Dirac delta function indicating there is an impulse response emerging at $t = 0$. With the definition of the initial pressure $p_0(\mathbf{x}) = \frac{\beta c_0^2}{C_P}A(\mathbf{x})$, the source term of equation (B.2.1) can be written as

$$\frac{\beta}{C_P}\frac{\partial H}{\partial t}(\mathbf{x},t) = \frac{p_0(\mathbf{x})}{c_0^2}\frac{d\delta(t)}{dt}. \tag{B.2.3}$$

The area of irradiation is a disk S that is centered at the origin and contains the initial pressure. In the way of the mathematical description, the function of the initial pressure has a compact support in a rectangle D. The sensor array surrounding D is deployed on the ring-shape boundary of S denoted by ∂S. The received waveform signals acquired by the sensors are denoted by $g(\mathbf{y},t) := p(\mathbf{y},t)$ where $\mathbf{y} \in \partial S$ and $t \in [0,T]$. Its expression is

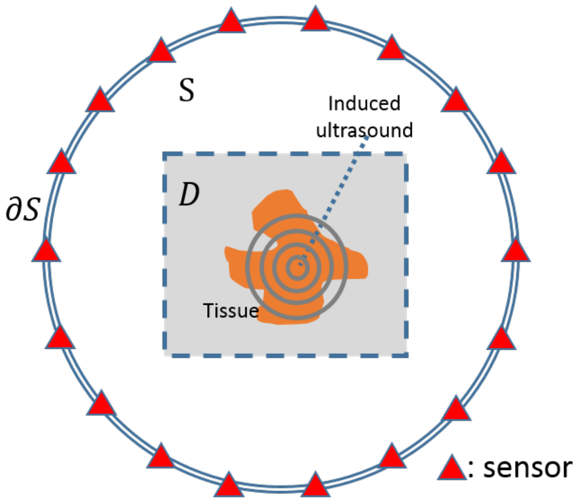

FIGURE B.1: Configuration of photoacoustic forward process.

followed with the Green's representation theorem:

$$g(\mathbf{y},t)=\frac{1}{c_0^2}\int_D \frac{\partial G_0}{\partial t}(\mathbf{y},\mathbf{x},t,0)p_0(\mathbf{x})d\mathbf{x},\ \mathbf{y}\in\partial S, \tag{B.2.4}$$

where G_0 is the free-space Green's function of equation B.2.1. The main task of photoacoustic imaging is to determine the initial pressure $p_0(\mathbf{x})$ of Eqs. (B.2.1)-(B.2.3) in D, given the received signal $g(\mathbf{y},t)$ on $\partial S\times[0,T]$.

B.2.1 Formulation of time-reversal photoacoustic imaging

The classical photoacoustic imaging is to solve the following acoustic wave propagation:

$$\begin{cases} \left(\nabla^2-\frac{1}{c_0^2}\frac{\partial^2}{\partial t^2}\right)v(\mathbf{x},t)=0, & (\mathbf{x},t)\in S\times(0,T);\\ v(\mathbf{x},0)=0=\frac{\partial v}{\partial t}(\mathbf{x},0), & \mathbf{x}\in S;\\ v(\mathbf{y},t)=\Phi(\mathbf{y})g(\mathbf{y},T-t), & (\mathbf{y},t)\in\partial S\times[0,T]. \end{cases} \tag{B.2.5}$$

The wavefield $v(\mathbf{x},t)$ gives the process of the waveform propagation from the ring array ∂S, provided the reversed time of the received signal $g(\mathbf{y},t)$ in $t\in[0,T]$ on $\mathbf{y}\in\partial S$. $\Phi(\mathbf{y})$ is a window function which maps the wave signal to the received measurement on the sensor elements. Correspondingly, the Dirichlet Green's function G_d of equation (B.2.5) at the imaging point $\mathbf{x}\in S$

is determined by

$$\begin{cases} \left(\nabla_{\mathbf{y}}^2 - \frac{1}{c_0^2}\frac{\partial^2}{\partial \tau^2}\right) G_d(\mathbf{x},\mathbf{x}',t,\tau) = -\delta(\mathbf{x}-\mathbf{x}')\delta(t-\tau), & (\mathbf{x}',\tau) \in S \times (0,T); \\ G_d(\mathbf{x},\mathbf{x}',t,\tau) = 0 = \frac{\partial G_d}{\partial t}(\mathbf{x},\mathbf{x}',t,\tau), & \mathbf{x}' \in S \text{ and } t = \tau; \\ G_d(\mathbf{x},\mathbf{y},t,\tau) = 0, & (\mathbf{y},\tau) \in \partial S \times [0,T]. \end{cases} \tag{B.2.6}$$

Then the imaging function $I_1(\mathbf{x})$ of the continuous formulation is defined as the image of the wavefield $v(\mathbf{x},T)$ at the terminal time T in the region of interest D when we set $\Phi(\mathbf{y})$ is an indicator function gives a unit value on ∂S and vanishes otherwise, i.e.

$$I_1(\mathbf{x}) = v(\mathbf{x},T) = \int_0^T \int_{\partial S} \frac{\partial G_d}{\partial \nu_{\mathbf{y}}}(\mathbf{x},\mathbf{y},T,t) g(\mathbf{y},T-t) d\sigma(\mathbf{y}) dt, \tag{B.2.7}$$

where $\nu_{\mathbf{y}}$ is the unit normal vector on $\mathbf{y} \in \partial S$. equation (B.2.7) is derived from the Green's function representation of wave equation. This can be referred to equation (13) in **Xu2004** and equation (A3) in **Burgholzer2007** as well. As image is reconstructed from reversing time of the signal $g(\mathbf{y},t)$, this method is the so-call time-reversal (TR) photoacoustic imaging.

In this work, we also focus on the semi-discrete form of the TR imaging function (B.2.7). Consider a circular boundary ∂S_N of the radius of R is a pointwise subset of ∂S containing N sampling sensor points $\mathbf{y_n}$ $(n = 1,2,\cdots,N)$ with equally spaced arguments. By means of defining $\Phi(\mathbf{y}) = \frac{2\pi R}{N}\sum_{n=1}^{N} \delta(\mathbf{y}-\mathbf{y_n})$, the semi-discrete TR imaging function is obtained as

$$I_1'(\mathbf{x}) = \frac{2\pi R}{N} \sum_{n=1}^{N} \int_0^T \frac{\partial G_d}{\partial \nu_{\mathbf{y}}}(\mathbf{x},\mathbf{y},T,t)\bigg|_{\mathbf{y}=\mathbf{y_n}} g(\mathbf{y_n},T-t) dt, \tag{B.2.8}$$

B.2.2 Interferometry alternative

In **Xu2004**, it is implied that instead of imposing a time-reversal boundary condition, the image is able to be reconstructed from the interferometry of the received wavefield by means of regarding each time-reversal received signal as a source. With this methodology, Eq. (B.2.5) is rewritten as

$$\begin{cases} \left(\nabla^2 - \frac{1}{c_0^2}\frac{\partial^2}{\partial t^2}\right) v_\tau(\mathbf{x},t) = -\frac{1}{c_0}\frac{d\delta(t-\tau)}{dt} g(\mathbf{x},T-\tau)\Phi_{\partial S_N}(\mathbf{x}), & (\mathbf{x},t) \in \mathbb{R}^2 \times (0,T); \\ v_\tau(\mathbf{x},0) = 0 = \frac{\partial v_\tau}{\partial t}(\mathbf{x},0), & \mathbf{x} \in \mathbb{R}^2 \text{ and } t = \tau; \end{cases} \tag{B.2.9}$$

where $\Phi_{\partial S_N}(\mathbf{x})$ is the indicator function defined as above. Accordingly, if we assume $\partial S_N = \partial S$, the interferometry alternative (IA) imaging function can be obtained from Duhamel's principle as:

$$I_2(\mathbf{x}) := \int_0^T v_\tau(\mathbf{x}, T) d\tau = \frac{1}{c_0} \int_0^T \int_{\partial S} \frac{\partial G_0}{\partial t}(\mathbf{x}, \mathbf{y}, \tau, t = T) g(\mathbf{y}, T - \tau) d\sigma(\mathbf{y}) d\tau, \tag{B.2.10}$$

where G_0 is the free-space Green's function and $v_\tau(\mathbf{x}, t)$ is the interferometric wavefield at the time $t \in [0, T]$. The mathematical derivation also refers to **Ammari2011** and **Arridge2016a**; **Arridge2016b**. In their paper, this method is named as modified time reversal (MTR) or backpropagation (BP). Similar to the derivation of equation (B.2.8), the semi-discrete IA imaging function is written as

$$I_2'(\mathbf{x}) = \frac{2\pi R}{N c_0} \sum_{n=1}^{N} \int_0^T \frac{\partial G_0}{\partial t}(\mathbf{x}, \mathbf{y}, \tau, t = T)\bigg|_{\mathbf{y}=\mathbf{y_n}} g(\mathbf{y_n}, T - \tau) d\tau. \tag{B.2.11}$$

In **Ammari2011**, it turns out that the continuous TR imaging function I_1 approximates the continuous IA one I_2 in the situation where the boundary ∂S is continuous and in the far-field. Further discussion is presented in Section B.5.2. However, the outcome can not extend to the semi-discrete form of the imaging functions. The analyses in next section are proposed to show the technical details of the reason why there exists a gap between the continuous and semi-discrete imaging functions.

B.3 Analyses

In this section, we demonstrate that interferometry alternative has better imaging resolution over the time-reversal method. To see this, the following assumptions are required. First, the analyses are carried out in the case where there is only an impulse response emanating from a point in the region D. Mathematically, the initial pressure is given by the Dirac delta function $\delta(\mathbf{y} - \mathbf{a})$ emerging at the point a in D. With equation (B.2.4) and the temporal Fourier transform, we can write the received signal as $\hat{g}(\mathbf{y}, \omega) = -\frac{i\omega}{c_0^2} \hat{G}_0(\mathbf{y}, \mathbf{a}, \omega)$. The second assumption is that the ring-array boundary ∂S lies in the far field relative to the bounded region D, mathematically expressed by $\mathrm{dist}(\partial S) > 2\mathrm{dist}(\mathrm{supp}\{p_0\})$. The "dist" denotes the maximum distance of the set and the "supp" the support of the function (or the nonzero-value domain of the function).

B.3.1 Analyses on the resolution

Since the continuous and semi-discrete imaging functions for each method share the common integrands, we only look deeply into the explicit expression of the continuous forms of I_1 and I_2. Using Parseval's Theorem, $\widehat{g}(\mathbf{y}, -\omega) = \overline{\widehat{g}(\mathbf{y}, \omega)}$, $\widehat{G_d}(\mathbf{x}, \mathbf{y}, -\omega) = \overline{\widehat{G_d}(\mathbf{x}, \mathbf{y}, \omega)}$, $\widehat{G_0}(\mathbf{x}, \mathbf{y}, -\omega) = \overline{\widehat{G_0}(\mathbf{x}, \mathbf{y}, \omega)}$, and the low-pass filter, we obtain the alternative forms of the imaging functions (B.2.7) and (B.2.11):

$$I_1(\mathbf{x}) = \Re\left\{\int_{-\infty}^{+\infty}\int_{\partial S}\frac{1}{\pi}\frac{\partial\widehat{G_d}}{\partial\nu_{\mathbf{y}}}(\mathbf{x},\mathbf{y},\omega)\overline{\widehat{g}(\mathbf{y},\omega)}d\sigma(\mathbf{y})d\omega\right\}, \tag{B.3.1}$$

$$I_2(\mathbf{x}) = \Re\left\{\int_{-\infty}^{+\infty}\int_{\partial S}\frac{i\omega}{\pi c_0}\widehat{G_0}(\mathbf{x},\mathbf{y},\omega)\overline{\widehat{g}(\mathbf{y},\omega)}d\sigma(\mathbf{y})d\omega\right\}. \tag{B.3.2}$$

where the symbol hat represents the Fourier transform in time domain, and the points $\mathbf{x}$ and $\mathbf{y}$ are located in D and ∂S, respectively. Note that with the assumption that $\text{dist}(\partial S) > 2\text{dist}(\text{supp}\{p_0\})$ as well as $\text{dist}(\partial S)$ is sufficiently larger than the wavelength of impulse with respect to the angular frequency ω, the normal derivative of Dirichlet Green's function $\partial\widehat{G_d}/\partial\nu_{\mathbf{y}}$ is approximated by $2\partial\widehat{G_0}/\partial\nu_{\mathbf{y}}$ using geometrical optics approximation; see **Xu2004**. Hence the comparison of the resolution between $I_1(\mathbf{x})$ and $I_2(\mathbf{x})$ is conducted on the spatial and frequency characteristics of the integrands of Eqs. (B.3.1) and (B.3.2) which are given by

$$K_1(\mathbf{x},\mathbf{y},\omega) = \frac{\partial\widehat{G_0}}{\partial\nu_{\mathbf{y}}}(\mathbf{x},\mathbf{y},\omega)\overline{\widehat{g}(\mathbf{y},\omega)}, \tag{B.3.3}$$

$$K_2(\mathbf{x},\mathbf{y},\omega) = \frac{i\omega}{c_0}\widehat{G_0}(\mathbf{x},\mathbf{y},\omega)\overline{\widehat{g}(\mathbf{y},\omega)}. \tag{B.3.4}$$

To split the spatial points $\mathbf{x}$ and $\mathbf{y}$ in $\widehat{G_0}(\mathbf{x},\mathbf{y},\omega)$, the additional theorem for the Hankel function of the first kind is recalled (**Colton2013**):

$$\frac{i}{4}H_0^{(1)}\left(\frac{\omega}{c_0}|\mathbf{x}-\mathbf{y}|\right) = \frac{i}{4}\sum_{l=-\infty}^{+\infty}J_l\left(\frac{\omega}{c_0}|\mathbf{x}|\right)H_l^{(1)}\left(\frac{\omega}{c_0}|\mathbf{y}|\right)e^{il(\theta_{\mathbf{x}}-\theta_{\mathbf{y}})}, \tag{B.3.5}$$

since $|\mathbf{x}| < |\mathbf{y}|$. Here, J_l and $H_l^{(1)}$ denotes the Bessel and first-kind Hankel functions of order l, and $\theta_{\mathbf{x}}$ and $\theta_{\mathbf{y}}$ the polar angles of $\mathbf{x}$ and $\mathbf{y}$, respectively. With the additive theorem (B.3.5), the recurrence relation $dH_l^{(1)}(\rho)/d\rho = l\rho^{-1}H_l^{(1)}(\rho) - H_{l+1}^{(1)}(\rho)$, and the asymptotic behavior $H_l^{(1)}(\rho) \sim \sqrt{\frac{2}{\pi\rho}}e^{i(\rho-(2l+1)\pi/4)}$ as $\rho \to +\infty$ with $\rho > 0$ (**Abramowitz1966**), we write out the expansion of the kernel

(B.3.3):

$$K_1(\mathbf{x},\mathbf{y},\omega) = \sum_{l=-\infty}^{+\infty} \frac{\left(\frac{l}{|\mathbf{y}|} + \frac{i\omega}{c_0}\right) J_l\left(\frac{\omega}{c_0}|\mathbf{x}|\right)}{16\pi^2 c_0 |\mathbf{y}|^{1/2}|\mathbf{y}-\mathbf{a}|^{1/2}} e^{i\left[\frac{\omega}{c_0}(|\mathbf{y}|-|\mathbf{y}-\mathbf{a}|)-\frac{l+1}{2}\pi + l(\theta_{\mathbf{x}}-\theta_{\mathbf{y}})\right]}. \quad \text{(B.3.6)}$$

Following the analogous deduction as equation (B.3.6), we have the expansion of the kernel (B.3.4):

$$K_2(\mathbf{x},\mathbf{y},\omega) = \sum_{l=-\infty}^{+\infty} \frac{\frac{i\omega}{c_0} J_l\left(\frac{\omega}{c_0}|\mathbf{x}|\right)}{16\pi^2 c_0 |\mathbf{y}|^{1/2}|\mathbf{y}-\mathbf{a}|^{1/2}} e^{i\left[\frac{\omega}{c_0}(|\mathbf{y}|-|\mathbf{y}-\mathbf{a}|)-\frac{l+1}{2}\pi + l(\theta_{\mathbf{x}}-\theta_{\mathbf{y}})\right]}. \quad \text{(B.3.7)}$$

Since the two integrands have the common part of a Bessel function $J_l\left(\omega|\mathbf{x}|/c_0\right)$ with respect to the index l, the imaging point $\mathbf{x}$ and the angular frequency ω, regarding the component of the summation. Hence, the weights left by the Bessel function determine the resolution of the imaging functions. Since they are composed by the function of the angles $\theta_{\mathbf{x}}$ and $\theta_{\mathbf{y}}$, l, and ω, without loss of generality, we analyze how l and ω make an influence on the weights with assuming the fixed angles $\theta_{\mathbf{x}}$ and $\theta_{\mathbf{y}}$.

We first discuss that each Bessel function $J_l\left(\omega|\mathbf{x}|/c_0\right)$ is band-limited by either the chosen $\omega|\mathbf{x}|/c_0$ or the index l. In figure B.2, it shows that the line $l = \omega|\mathbf{x}|/c_0$ is a borderline between the oscillating region and the fast decayed region. Thurs, for each fixed imaging point $\mathbf{x}$, one of the parameters, l or ω, determines the maximum value of the other one chosen at the borderline. The analogous analysis is referred to **Xu2002**. Theqrefore, only the angular frequency ω in the kernels (B.3.6) and (B.3.7) plays the principal role on the resolution of the imaging functions.

Henceforth in this subsection, we see that the variable ω of the weights dominates given fixed $\mathbf{x}$ in D and $\mathbf{y}$ on ∂S. Considering equation (B.3.6), the weight is denoted by $b_1(l,\omega) := \frac{l}{|\mathbf{y}|} + \frac{i\omega}{c_0}$. The maximum l that is chosen by $l = \omega|\mathbf{x}|/c_0$ is utilized to approximate b_1 as $b_1 \approx \frac{\omega}{c_0}\left(\frac{|\mathbf{x}|}{|\mathbf{y}|} + i\right)$. It implies that the weight whose l is evaluated at the maximum has the factor of the order-one ω. On the other hand, the weight in equation (B.3.7) is denoted by $b_2(\omega) := \frac{i\omega}{c_0}$ which is merely a function of the angular frequency ω. The modulus of the weight is proportional to ω of order 1 for all l such that the high-frequency component of the Bessel function $J_l(\omega|\mathbf{x}|/c_0)$ are assigned to the large weight. This amplifies the intensity near point $\mathbf{a}$ for the high-frequency components of data since those contains the signal of the impulse response in the situation of the photoacoustic effect. Moreover, in terms of the discussions of both TR

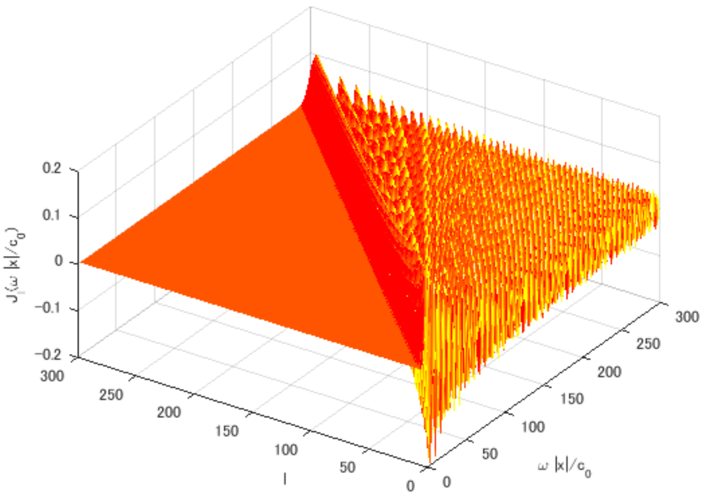

FIGURE B.2: Bessel function $J_l\left(\omega|x|/c_0\right)$ versus l and $\omega|x|/c_0$. The region is set in $(0,300)\times(0,300)$.

and IA, some terms in equations (B.3.6) and (B.3.7) may be eliminated due to the arguments of the particular y found on the ring array. Note that the main difference between TR and IA is that towards each $l \leq \omega|x|/c_0$, the corresponding weight in equation (B.3.6) has a distinct phase whereas that in equation (B.3.7) keeps consistency of phase. Consequently, the TR imaging function (B.2.7) may cause the problem where the sampling sensor element y is chosen to maximize b_1 for the particular l but eliminate it at another l. As a result, we summarize the similarities and differences of the weights b_1 and b_2 as follows:

- Similarities: they are both proportional to the order-one ω at the maximum possible value of l.
- Differences: for any fixed ω and x, the phase of $b_1(l,\omega)$ varies with all the feasible $l \leq \omega|x|/c_0$ while $b_2(\omega)$ keeps consistency of phase.

B.3.2 Analyses of sampling by the sensor elements

In the photoacoustic experiment, only a few of ultrasound sensors are deployed on a ring array. Usually, the received signals have abundant time samples but limited sensor elements. In Section B.4.2, the numerical results indicate that the number of sensors on the ring array ∂S significantly is associated with the resolution of the reconstructed images. Theqrefore, in this subsection, we analyze the principle of sampling by the sensor elements in photoacoustic imaging. We employ the phase analysis to qualitatively show the relation of sampling and resolution. Additionally in this subsection, the sampling analysis is conducted on the discrete ring array ∂S_N. Hence, the argument of the sensor point $\mathbf{y_n}$ is the unique variable in the discussion.

In terms of the TR imaging function (B.2.7), followed by the statement in Section B.3.1, the analysis of sampling is considered in the case where ω and l both has large values. Define the phase factor $a_1(\theta_{\mathbf{x}}, \theta_{\mathbf{y_n}}, l, \omega)$ of the integrand in equation (B.3.1) regardless of the factor $b_1(l, \omega)$. With the relation

$$|\mathbf{y_n} - \mathbf{a}| = |\mathbf{y_n}| - |\mathbf{a}| \cos(\theta_{\mathbf{y_n}} - \theta_{\mathbf{a}}) + O(1/|\mathbf{y_n}|),$$

it follows that

$$a_1(\theta_{\mathbf{x}}, \theta_{\mathbf{y_n}}, l, \omega) \simeq e^{i\left[\frac{\omega}{c_0}|\mathbf{a}| \cos(\theta_{\mathbf{y_n}} - \theta_{\mathbf{a}}) - \frac{l+1}{2}\pi + l(\theta_{\mathbf{x}} - \theta_{\mathbf{y_n}})\right]}. \tag{B.3.8}$$

Then the phase change for the term is expressed as

$$a_1 b_1 = (\Re a_1 \Re b_1 - \Im a_1 \Im b_1) + i(\Re a_1 \Im b_1 + \Im a_1 \Re b_1). \tag{B.3.9}$$

Note that the real part of equation (B.3.9) takes principal effect in the reconstructed image because of the real value of equation (B.2.7). Following the aforementioned deduction, to enlarge the weight of $\Im b_1(l, \omega) = \omega / c_0$ and exclude $\Re b_1(l, \omega)$, we attempt to let the phase of $a_1(\theta_{\mathbf{x}}, \theta_{\mathbf{y_n}}, l, \omega)$ approximate to $k\pi + \pi/2$ where k is an integer, by the way to find the argument $\theta_{\mathbf{y_n}}$ from $n = 1, 2, \cdots, N$. This is attained through enhancing the rate of sampling, namely, an oscillation of the polar angle $\theta_{\mathbf{y_n}}$ since it may cause a significant phase change of a_1 when ω is large and l follows the inequality $l \leq \omega |\mathbf{x}| / c_0$ from the band-limited property of Bessel function in Figure B.2. As a result, increasing the rate of spatial sampling succeeds in retaining the dominating factor ω for equation (B.3.9) as well as restraining the influence of $\Re b_1(l, \omega)$ otherwise.

The analogous analysis applies to the IA imaging function (B.2.11). The phase factor $a_2(\theta_{\mathbf{x}}, \theta_{\mathbf{y_n}}, l, \omega)$ is identical to $a_1(\theta_{\mathbf{x}}, \theta_{\mathbf{y_n}}, l, \omega)$ with equation (B.3.7). Since $\Re b_2 = 0$, the spatial sampling associated with $\theta_{\mathbf{y_n}}$ has no impact on ω of order 1. Hence, in this situation, the relatively low sampling is acceptable for resolution nevertheless it leads to a low accuracy in terms of the numerical scheme of the imaging function.

B.4 Numerical results

In these numerical examples, the measurement g is considered to be corrupted by the wide-band noise. Naturally, the low-pass filter applying to the temporal components will move out the high-frequency artifacts generated in the reconstructed images. Incorporated with a low-pass filter at the prescribed frequency $\Omega > 0$, equation (B.3.2) is written as the following interferometry alternative imaging function with low-pass filter (LPF-IA):

$$I_3(\mathbf{x}) = \Re\left\{\int_{|\omega|\leq\Omega}\int_{\partial S}\frac{i\omega}{c_0}\hat{G}_0(\mathbf{x},\mathbf{y},\omega)\overline{\hat{g}(\mathbf{y},\omega)}d\sigma(\mathbf{y})d\omega\right\}, \tag{B.4.1}$$

and its semi-discrete form:

$$I_3'(\mathbf{x}) = \Re\left\{\sum_{n=1}^{N}\int_{|\omega|\leq\Omega}\frac{2\pi R\omega i}{Nc_0}\hat{G}_0(\mathbf{x},\mathbf{y_n},\omega)\overline{\hat{g}(\mathbf{y_n},\omega)}d\omega\right\}, \tag{B.4.2}$$

where the symbol bar represents complex conjugate while the hat represents the Fourier transform in t. In practice, noting that the imaginary part of $I_3(\mathbf{x})$ is sufficiently small to be neglected compared with its real part, only the real part of the imaging function $I_3(\mathbf{x})$ will be plotted.

Regarding discretization of the TR imaging function (B.2.7), the IA one (B.2.11), and the LPF-IA one (B.4.2), we use the Nyström method giving the straightforward approximation of the integrals by the quadrature rule (**Kress2014**). The composite trapezoidal rule, one of the quadrature rules, constructs the numerical integration by interpolating the integrand at each quadrature point; see Appendix A for details. To compare the resolution and sampling effect calculated by three imaging functions, each the reconstructed image is normalized by its corresponding maximum absolute value.

B.4.1 Configuration

The numerical test is carried out on a vasculature model originated from one of the testing examples in K-wave simulator, also as shown in figure B.3. This image provides the illuminated location of the initial pressure. The K-wave toolbox then simulates the propagation of pressure wavefield and detects the signal on the ring-shape sensor. The ring has a radius of 0.045 m and consists of some equi-spaced sensor elements. The background speed of sound is 1500 m/s. The imaging domain is a square region centered at the origin with an area of 0.05×0.05 m^2.

B.4.2 Resolution test for noise data

The reconstructed vasculature images with utilizing the various photoacoustic imaging functions, i.e. I_1, I_2, and I_3, are shown in figure B.4, with respect to the noisy measurements g of distinct signal-to-noise ratio (SNR). Since the reconstructed images are normalized, what we concern in photoacoustic imaging is restricted to resolution and artifact. We observe that applied to the noise-free data, the IA imaging functions I_2 and the LPF-IA one I_3 both reconstruct higher-resolution images than the TR one I_1. Additionally, the reconstructed image using I_2 is vulnerable to the artifact compared with that using I_3, especially with low-SNR data.

Figure B.5 shows the profiles of the reconstructed images along the horizontal line through -0.005 m, which are extracted from figure B.4. Regarding these profiles, there exist two principal peaks illustrating the brightness defined as the relative intensity of pressure. The full width at half maximum (FWHM) is introduced to assess the resolution of the profile quantitatively. FWHM is measured by the length of the interval between two half-maximum points on a peak. Moreover, the image contrast, assessing the maximum pixel intensity for the proposed imaging method, is measured by the maximum of a peak. The results of FWHM and the contrast are shown in table B.1. We observe that TR always reconstructs images with relatively low resolution but fine contrast. However, the images reconstructed by IA have high resolution but are vulnerable to the low-SNR data. LPF-IA has both advantages of the resolution and contrast, even if the applied data have low SNR. Here is a remark that FWHM of IA with 20-SNR makes no sense because of its corresponding negligible value of contrast.

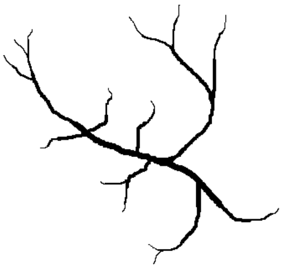

FIGURE B.3: Initial pressure emitted from a vasculature which is an example extracted from K-wave toolbox (**kwave**).

TABLE B.1: Resolution and contrast results of the profile along the horizontal line through -0.005 m with respect to the numerical methods and the noise levels. Figure B.5 illustrates the two peaks numbered from left to right. FWHM and maximum of normalized pressure (abbreviated as maximum) assess resolution and contrast, respectively. We use the measurements $\hat{g}(y, \omega)$ corrupted with noise-free, 40-SNR, and 20-SNR Gaussian noise.

Methods \ Data		Noise free		40 SNR		20 SNR	
		Peak 1	Peak 2	Peak 1	Peak 2	Peak 1	Peak 2
IP	FWHM (mm)	0.1429	0.1266	0.1429	0.1266	0.1429	0.1266
	Maximum	0.3865	0.6395	0.3865	0.6395	0.3865	0.6395
TR	FWHM (mm)	0.3662	0.3660	0.3237	0.3252	0.3727	0.3647
	Maximum	0.3992	0.5338	0.3994	0.5322	0.3892	0.4812
IA	FWHM (mm)	0.1596	0.1262	0.2083	0.2082	–	–
	Maximum	0.3143	0.4965	0.3047	0.4990	0.0570	0.1525
LPF-IA	FWHM (mm)	0.1850	0.1297	0.1676	0.1303	0.1793	0.1287
	Maximum	0.3683	0.6029	0.3825	0.6094	0.3521	0.6831

B.4.3 Sensor-element sampling test

The reconstructed vasculature images related to the number of sensors are shown in figure B.6. The configuration is set as Section B.4.1 except for applying the noise-free data. Figure B.5 shows the profiles of the reconstructed images along the horizontal line through -0.005 m, which are extracted from figure B.6. And in table B.2, the relation between the sampling by the sensor elements and the imaging functions is assessed by FWHM as well as the maximum. We observe that a large number of the sensor-element sampling significantly improves the resolution of the reconstructed images using the TR imaging function, whereas it upgrades the contrast of the images using the IA imaging function. Regardless of the artifacts, the LPF-IA imaging function produces the sharp image even when a few sensors are provided for the reconstruction.

B.5 Discussion

B.5.1 Model assumptions

Some assumptions are made for the particular purposes. In practice, the first is that the ring array of sensors is designed to deploy limited sensor elements, owing to the fact of expense and technical complexity factors. The abundant temporal samples can record the principal frequency components

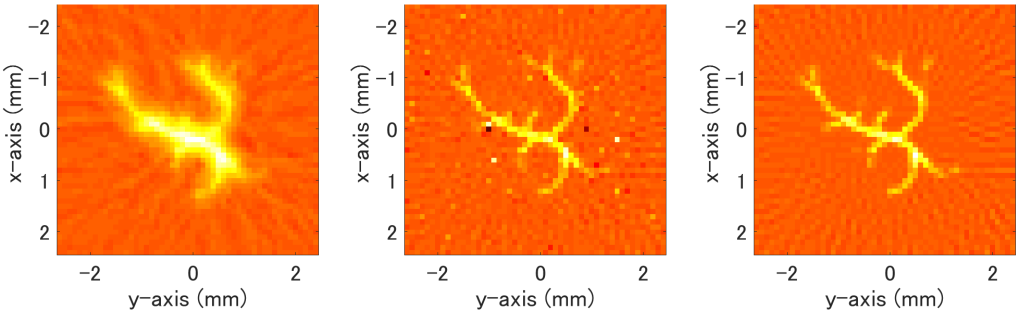

(a) TR, noise-free data. (b) IA, noise-free data. (c) LPF-IA, noise-free data.

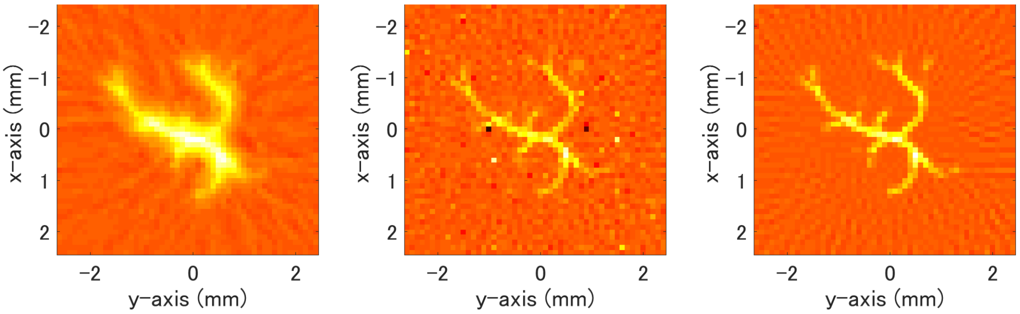

(d) TR, 40-SNR data. (e) IA, 40-SNR data. (f) LPF-IA, 40-SNR data.

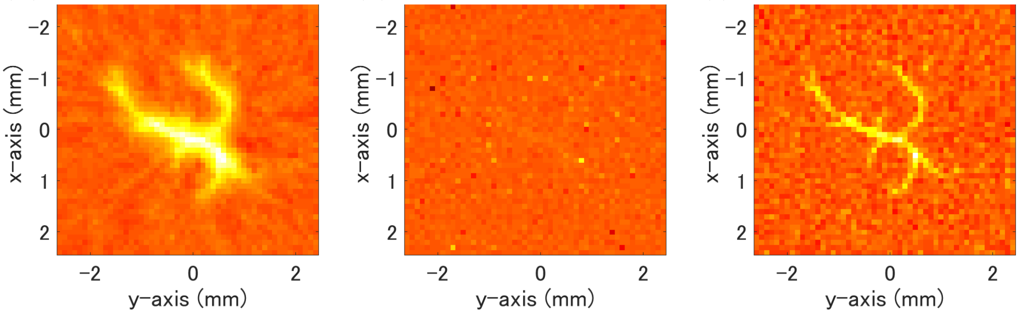

(g) TR, 20-SNR data. (h) IA, 20-SNR data. (i) LPF-IA, 20-SNR data.

FIGURE B.4: Numerical results with the use of the imaging functions $I_1(x)$, $I_2(x)$, and $I_3(x)$. The measurements are noise-free, 20 SNR, and 40 SNR for every row of images.

arising from the induced ultrasound impulse, since the temporal sampling frequency is considerably high, and only the mollified impulse has been measured by the sensor in the real experiment. Thus, samples of sensors are much less temporal samples in the measurements. From the theoretical assumption on the far-field requirement of the ring array ∂S, the received data set will dramatically increase at the dimension of the sensor element due to the Nyquist criterion. However, from the aforementioned analysis, the IA method reconstructs a high-quality image using only sub-Nyquist rate of the sensor element in the data set. The progress of the IA method is of interest as it compresses the data set, saves the cost of sensor elements, and potentially accelerates the frame rate for the dynamic photoaoustic tomography images.

TABLE B.2: Resolution and contrast results of the profile along the horizontal line through -0.005 m with respect to the numerical methods and the spatial sampling points. Figure B.7 illustrates the two peaks numbered from left to right. FWHM and maximum of normalized pressure (abbreviated as maximum) assess resolution and contrast, respectively. The spatial sampling points along the ring transducers are 35, 70, and 140. We use the noise-free measurements $\hat{g}(y, \omega)$ in this case.

	N_s	35		70		140	
Methods		Peak 1	Peak 2	Peak 1	Peak 2	Peak 1	Peak 2
IP	FWHM (mm)	0.1429	0.1266	0.1429	0.1266	0.1429	0.1266
	Maximum	0.3865	0.6395	0.3865	0.6395	0.3865	0.6395
TR	FWHM (mm)	–	0.4690	0.3662	0.3660	0.2162	0.2309
	Maximum	0.4140	0.4796	0.3992	0.5338	0.3896	0.5246
IA	FWHM (mm)	0.1526	0.1329	0.1596	0.1262	0.1675	0.1366
	Maximum	0.1517	0.2182	0.3143	0.4965	0.3398	0.5896
LPF-IA	FWHM (mm)	0.1674	0.1377	0.1676	0.1303	0.1849	0.1333
	Maximum	0.3886	0.5414	0.3825	0.6094	0.3284	0.6013

The second is that the lossless medium is assumed to be set in the entail space. In Section B.3, all the analyses are based on the additional theorem that expands the free-space Green's function. However, the tissue in the medium often has the properties of attenuation and heterogeneous speed of sound in practice. The analyses in Section B.3 can not be extended to the attenuated and heterogeneous medium since the explicit expression of the Green's function is not available. Nevertheless, the results may be valid inspired by **Ammari2011** for the attenuated medium and **Modgil2010** for the heterogeneity.

B.5.2 Physical perspectives on photoacoustic imaging

Regarding the physical perspectives of TR and IA, the discussions are separated into the continuous and discrete configuration. The continuous configuration of TR and IA has fully been discussed in **Arridge2016a**; **Arridge2016b** using both mathematical and physical tools. They cope with the time-reversal measurements in different ways. TR treats the measurements as the in-let boundary (or mathematically, Dirichlet boundary condition) in an initial boundary value problem (IBVP) of the wave equation, while IA considers them as the time-varying pressure source for an initial value problem (IVP) of the wave equation in the free space. **Ammari2011** has shown that TR and IA are equivalent under the assumption of the continuous configuration with setting the ring array in the far field. Simultaneously, the reconstructed results of TR and IA can both approximate to the initial pressure with the same assumption.

However, regarding the discrete configuration, the ambiguity of equation (B.2.5) is apparently shown in the TR method. As the aforementioned assumption in Section B.5.1, the sensor elements are sampled at the sub-Nyquist rate. Due to the discrete sensor elements distributed on the ring array, using the linear or nearest interpolation on the domain, the multiple of continuous Dirichlet boundary condition can be made in the decision of the Dirichlet Green's function in equation (B.2.6). This problem as well happens in equation (B.2.7) where the normal vector n_y depends on the boundary shape. On the other hand, the IA method is still well-defined in the discrete configuration. The process of IA has the same mode of propagation as the forward process. This may alleviate the lost accuracy from the discretization of the mathematical model.

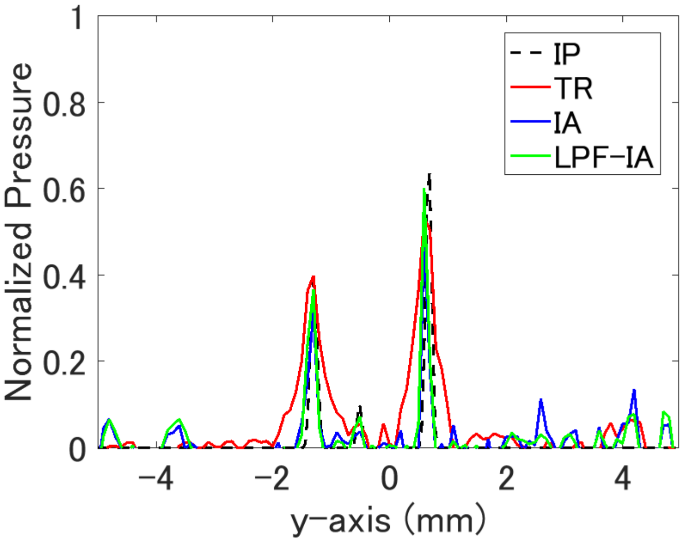

(a) Profile, noise-free data.

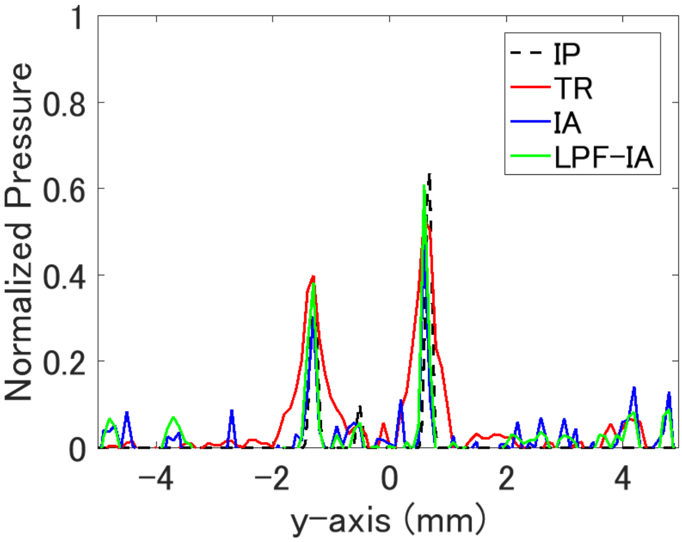

(b) Profile, 40-SNR data.

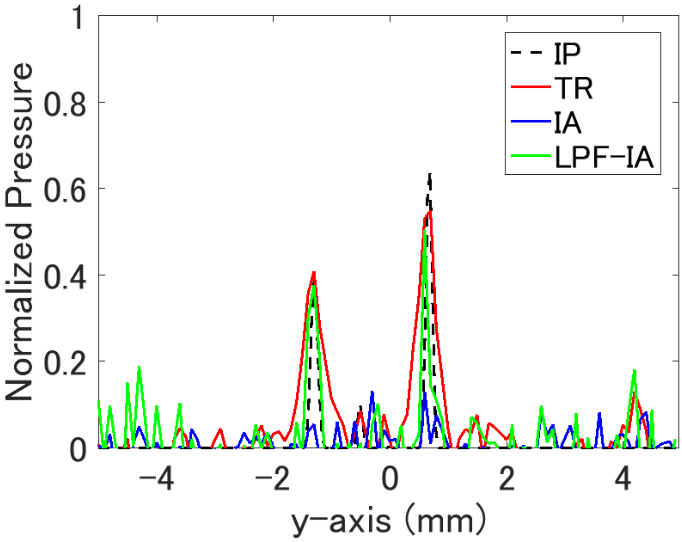

(c) Profile, 20-SNR data.

FIGURE B.5: Profile along the horizontal line through -0.005 m with the use of the imaging functions $I_1(x)$, $I_2(x)$, and $I_3(x)$. The measurements are (a) noise-free, (b) 40 SNR, and (c) 20 SNR.

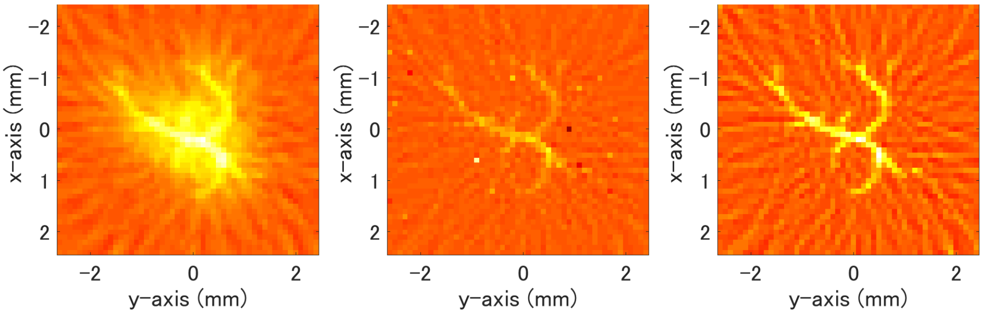

(a) TR, $N_s = 35$. (b) IA, $N_s = 35$. (c) LPF-IA, $N_s = 35$.

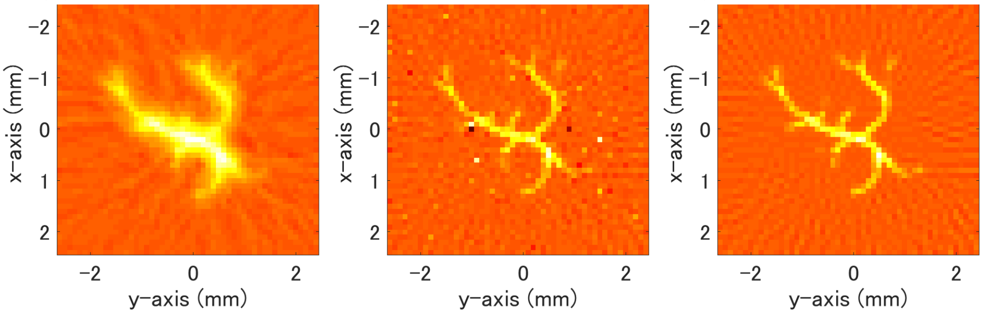

(d) TR, $N_s = 70$. (e) IA, $N_s = 70$. (f) LPF-IA, $N_s = 70$.

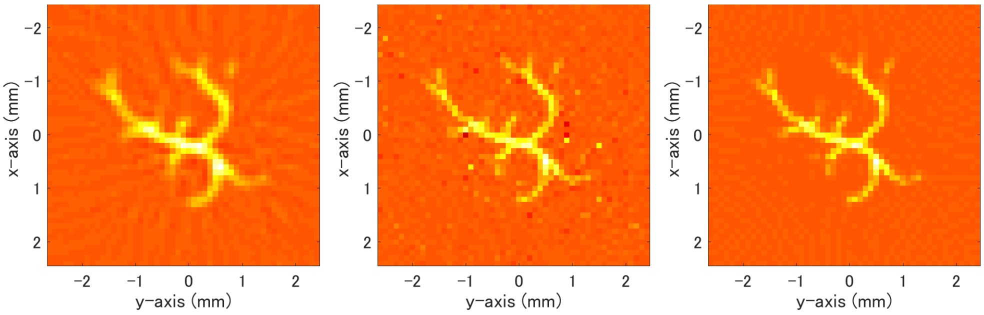

(g) TR, $N_s = 140$. (h) IA, $N_s = 140$. (i) LPF-IA, $N_s = 140$.

FIGURE B.6: Numerical results with the use of the imaging functions $I_1(x)$, $I_2(x)$, and $I_3(x)$. The numbers of sensors are chosen as (a) 35, (b) 70, and (c) 140.

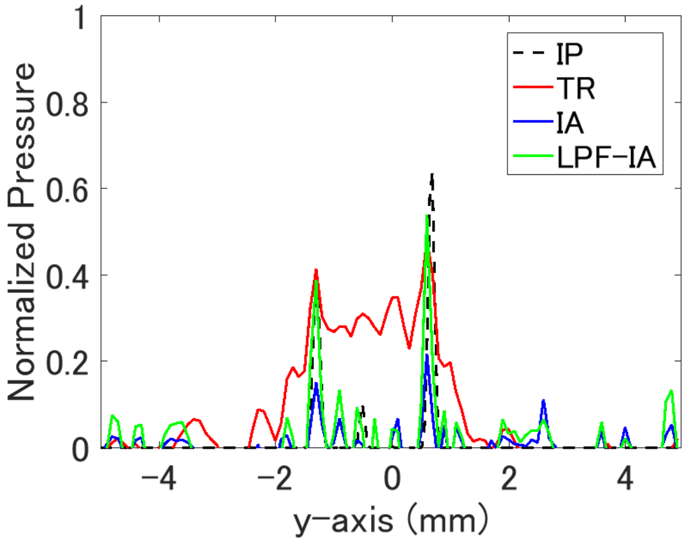

(a) Profile, $N_s = 35$.

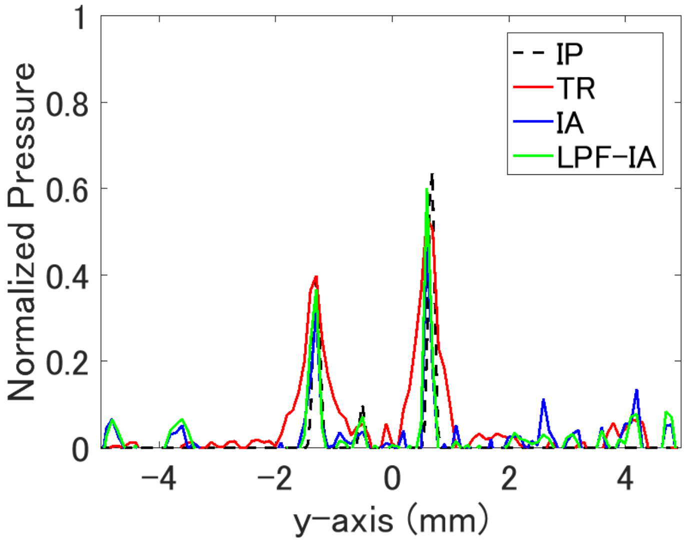

(b) Profile, $N_s = 70$.

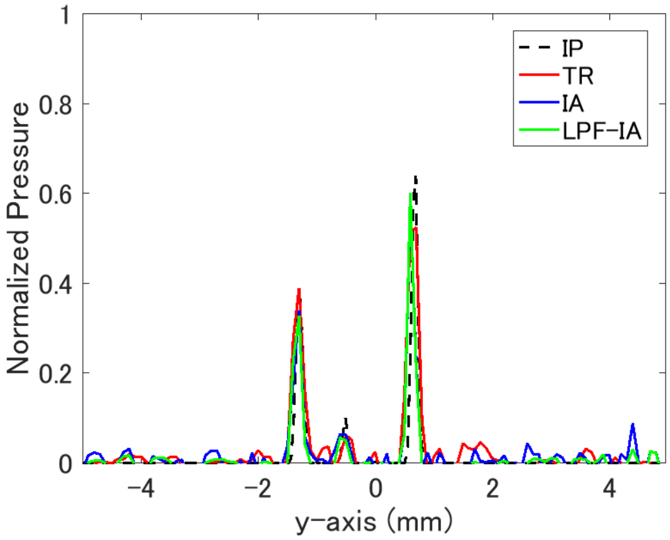

(c) Profile, $N_s = 140$.

FIGURE B.7: Profile along the horizontal line through -0.005 [m] with the use of the imaging functions $I_1(x)$, $I_2(x)$, and $I_3(x)$. The numbers of sensors are chosen as 35, 70, and 140 for each imaging function.